Analysis of particle and cluster characterization methods used in aerosol science

A DISSERTATION

SUBMITTED TO THE FACULTY OF

UNIVERSITY OF MINNESOTA

BY

Jikku Moolamkunnam Thomas

IN PARTIAL FULFILLMENT OF THE REQUIREMENTS

FOR THE DEGREE OF

DOCTOR OF PHILOSOPHY

Professor Christopher J Hogan Jr.

December 2018

Acknowledgements

This thesis is the result of several years of graduate study and could not have been completed without the gracious contributions of several individuals and organizations. First of all, I would like to express my heartfelt gratitude to Prof. Chris Hogan, my graduate advisor and mentor. Without his patient technical advising, financial support and emotional backing, this dissertation would surely not have seen the light of day.

I would also like to thank the members of my final examination committee, Prof. Alon McCormick, Prof. Satish Kumar and Prof. Sungyon Lee for taking the time to review my thesis and evaluate me.

The studies leading up to this thesis could be completed in a timely manner due to the excellent work environment that Prof. Chris Hogan has cultivated in his group. Former and current members of the Particle Technology Laboratory contributed in differing, but significant ways to ensure the completion of these studies. Some of them were teachers and mentors, others engaged me in several challenging and thoughtful discussions which improved the final outcomes. Everyone was gracious and accommodating in sharing resources that were essential to the progress of my dissertation. In particular, I would like to thank Dr. Thaseem Thajudeen, Prof. Carlos Larriba-Andaluz, Dr. Anne Maisser, Dr. Derek Oberreit, Dr. Siqin He and Jihyeon Lee. The staff of the CSE Machine Shop and the ECE Depot were instrumental in providing technical and fabrication expertise required for the building of experimental systems that were part of the studies in this thesis.

I would like to take this opportunity to recognize the technical assistance and financial support provided by Kanomax-FMT in completing the studies on the development of the drift tube in a timely manner. Also, CT Associates, Inc participated in making me a better engineer by granting me the opportunity of an internship with them. Further, they helped me navigate engineering solutions when I was stuck on my projects.

Lastly, but definitely not the least, I would like to acknowledge the people who offered me unconditional support and love during this challenging period, namely, my family and friends. Their contributions ranged from sage wisdom in difficult situations to financial support in times of hardship. Their names are too many to list here, however, they know who they are and how much they have influenced my life.

To

My family and friends

Table of Contents

List of Tables

List of Figures

Chapter 1: Introduction

Aerosols are dispersions of liquid or solid particles suspended in a gaseous medium. They are encountered in a variety of important contexts, including atmospheric/ambient aerosol (Bianchi et al. 2016, Smith et al. 2010), which has an effect on human health and global climate, engine emissions (Yli-Ojanperä et al. 2012, Collings, Rongchai and Symonds 2014), and intentionally in manufacturing settings(Rahman et al. 2015, Pratsinis 2010). The particle size distribution function (the number concentration of particle of a defined size, per unit change in size) of aerosols is one of the primary properties of an aerosol which determines its behavior. A common method to measurement the size distribution function for aerosol particles below 1 micrometer in diameter (or equivalent mobility diameter) is electrical mobility spectrometry (also called ion mobility spectrometry) (Knutson and Whitby 1975b, Wang and Flagan 1990, Fang et al. 2014, Jiang et al. 2011a). In electrical mobility spectrometry, charged particles migrate through a gas driven by an electric field. The speed particles move is dependent upon the ratio of the electrostatic force (field strength and charge product) and the force on the particle (in the low Reynolds number, low Mach number limit); the electrical mobility is the ratio of the charge on the particle to its friction coefficient, which is in turn the proportionality coefficient between the drag force on the particle and its speed difference with the surrounding gas.

In aerosol measurement, the most common method of making electrical mobility measurements is via a differential mobility analyzer in combination with a condensation

particle counter (Jiang et al. 2011a, Wang and Flagan 1990). Though use of these instruments is widespread for size distribution function determination in the 2 nm - 300 nm size range, there are a number of features of the measurement process which are need of further characterization and clarification. The purpose of the studies performed here all pertain to refined analysis approaches for nanometer scale aerosol particles. To demonstrate why such studies are needed, Figure 1.1 depicts a typically differential mobility analyzer-condensation particle counter system, used in aerosol size distribution function measurements. In the figure, an aerosol, containing polydisperse particles of unknown size and charge state is sampled into the system at a prescribed flowrate. Electrical mobility analysis is only amenable to charged particles and hence first the particles must be brought to a known charge distribution, which is ideally independent of their chemical composition (which is unknown) and only dependent on particle size. The "perfect" ionization scheme would be one in which all particles, independent of their initial charge, passed through an ionizer which yielded all singly charged (i.e. either an excess electron or excess proton) particles, independent of size and chemical composition. However, no ionization scheme has been developed which can yield such a charge distribution and efforts to design such schemes (Adachi, Kousaka and Okuyama 1985 Fruin and McMurry 1988), UV-ionization sources (Burtscher et al. 1982)) typically yield singly and multiply charged particles and additionally can suffer from repeatability issues (i.e. the charge distribution is not always the same at the outlet, likely influenced by the incoming particle charge state). For this reason, in aerosol science, the most common adopted ionizer source is one which produces roughly equal concentrations of

positive and negative ions from trace gas species (parts-per-billion to parts-per-trillion concentration organic contaminants) present in the flow (Steiner and Reischl 2012). It appears that irrespective of chemical composition, when small ions collide with particles, they transfer their charge to the particles (Premnath, Oberreit and Hogan 2011). Therefore, in a bipolar ion environment (i.e. an environment wherein there is roughly equal concentration of positive and negative ions) the time rate of change of the number concentration (n_z) particles of diameter d_p, net charge z (z = -2, -1, 0, +1, +2, etc) is given by the equation (Adachi et al. 1985):

$$\frac{dn_z}{dt} = k_{z-1,+}n_{z-1}n_+ + k_{z+1,-}n_{z+1}n_- - k_{z,+}n_z n_+ - k_{z,-}n_z n_- \qquad (1.1)$$

where $k_{z,\pm}$ is the collision rate coefficient between ions (either positive "+" or negative "-") and particles, and $n_\pm$ is the number concentration of positive/negative ions. Provided particles spend a sufficiently long time in a bipolar environment, they will reach a steady-state charge distribution, where the fraction of particles with a specific charge state $f_z(d_p)$ can be predicted by setting equation (1.1) equal to 0, and assuming that $n_+ = n_-$:

$$f_0(d_p) = \frac{1}{1+\sum_{p=1}^{\infty}\prod_{i=1}^{p}\left(\frac{k_{i-1,+}}{k_{i,-}}\right)+\sum_{p=-1}^{-\infty}\prod_{i=-1}^{p}\left(\frac{k_{i+1,-}}{k_{i,+}}\right)} \qquad (1.2a)$$

$$f_z(d_p) = \frac{\prod_{i=1}^{z}\left(\frac{k_{i-1,+}}{k_{i,-}}\right)}{1+\sum_{p=1}^{\infty}\prod_{i=1}^{p}\left(\frac{k_{i-1,+}}{k_{i,-}}\right)+\sum_{p=-1}^{-\infty}\prod_{i=-1}^{p}\left(\frac{k_{i+1,-}}{k_{i,+}}\right)} \qquad z \geq +1 \qquad (1.2b)$$

$$f_z(d_p) = \frac{\prod_{i=-1}^{z}\left(\frac{k_{i+1,-}}{k_{i,+}}\right)}{1+\sum_{p=1}^{\infty}\prod_{i=1}^{p}\left(\frac{k_{i-1,+}}{k_{i,-}}\right)+\sum_{p=-1}^{-\infty}\prod_{i=-1}^{p}\left(\frac{k_{i+1,-}}{k_{i,+}}\right)} \qquad z \leq -1 \qquad (1.2c)$$

Clear from (1.2) is that if the collision rate coefficients are known, the steady-state charge distribution is known. The collision rate coefficients depend upon the particle size (diameter for spheres), the mobility/diffusion coefficient of the ion, and the ion mass (through its mean thermal speed). Using approximate ion properties estimated in air, and Fuchs limiting sphere theory (Fuchs 1963b) (with the correction introduced by Hoppel & Frick (Hoppel and Frick 1986)) Wiedensohler developed regression equations(Wiedensohler 1988) to predict $f_z(d_p)$ for electrical mobility based measurements. Though these are used almost universally in aerosol science, there are a number of reasons to investigate their validity. First, as discussed by Gopalakrishnan et al(Gopalakrishnan and Hogan 2012a, Gopalakrishnan, McMurry and Hogan Jr 2015b, Gopalakrishnan et al. 2013a), Fuchs limiting sphere theory breaks down when determining $k_{z,-}$ and $k_{z,+}$ for positively and negatively charged particles in the sub 20 nm size range, respectively (i.e. when strong attractive Coulomb interactions influence collisions). Second, and perhaps more importantly, the ion properties (diffusivity and mass) input regression equations are entirely assumed; meanwhile, different environments may have vastly different types of ions generated. Related to this, third, the existing regression equations are based on the assumption of one type of positive and one type of negative ion (i.e. one ion mass and one ion mobility). This too, would not be expected in an actual environment. The first study presented in this dissertation hence focuses on direct measurement of the ion properties (masses and mobilities) in atmospheric pressure air produced by a bipolar ion source (specifically a Po-210 alpha particle source). These ion properties are compared to predictions based on structural

models and used to predict the charge distribution on particles accounting for the heterogeneity in the ion population through the approach of Gopalakrishnan et al (Gopalakrishnan et al. 2015b).

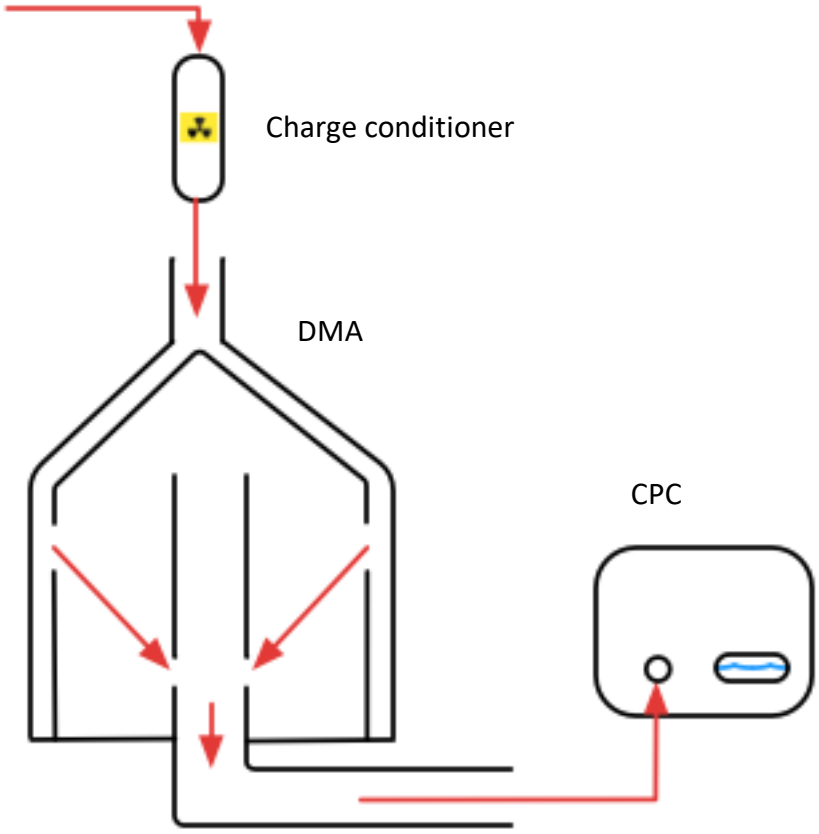

Figure 1.1. Schematic of differential mobility analysis for size distribution function measurement

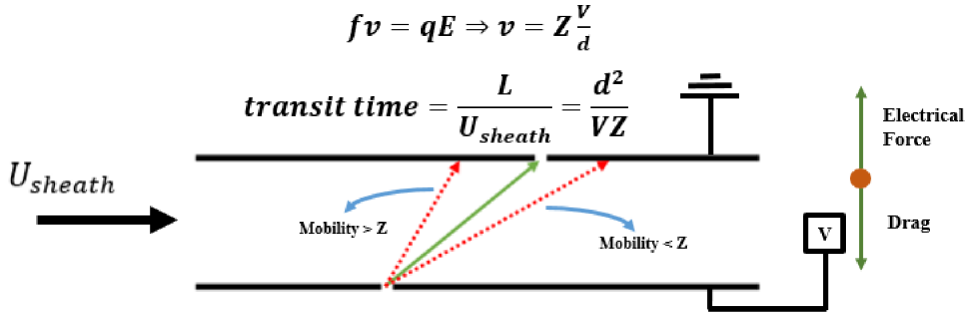

Figure 1.2. Schematic of a parallel plate DMA. L is the distance between in the slits in the horizontal dimension, d the vertical separation between the plates, U_{sheath} the sheath gas speed, and V the voltage difference applied between the plates. The free body diagram of a positive ion of charge q and friction factor f is shown. Mobility is the drift speed (v) per unit electrical field (E). Only ions of mobility Z have the required trajectory (Greenspan) to traverse the slit on the other side and the other ions follow the red trajectories.

The second step in size distribution function measurement by electrical mobility based techniques is the actual mobility classification by an instrument known as a differential mobility analyzer (DMA). Mobility (Z) is related to particles charge (q) and the mobility equivalent size (d_p) by the following equation:

$$Z = \frac{qC_c}{3\pi\mu d_p} \tag{1.3}$$

where C_c is known as the slip correction factor, and function of particle diameter, and gas mean free path. This factor corrects for non-continuum effects as d_p approaches the mean free path of the background gas (drag becomes dominated by ballistic collisions by gas molecules, rather than by the more familiar continuum mechanisms of momentum transfer). The mathematical formulation of C_c is such that the mobility becomes inversely proportional to d_p^2 as d_p becomes much smaller than the gas mean free path

(the high Knudsen number limit or the free molecular regime). In the opposite case, i.e. as d_p becomes much larger than the mean free path (the low Knudsen number limit), the familiar Stokes drag coefficient is recovered (mobility becomes inversely proportional to d_p) in the denominator of equation 1.3; this is termed the continuum limit.

DMAs are available in different geometries such as concentric cylindrical(Knutson and Whitby 1975a, Chen et al. 1998), parallel plate(Rus et al. 2010a), and radial(Zhang et al. 1995); all operate on the same general principle, which schematized in Figure 1.2 for a parallel plate type DMA. Briefly, depending on the operating parameters of the DMA, namely sheath flow rate and voltage applied across plates, only particles within a mobility window (dependent on geometric and operating parameters) are transmitted from a slit on the front electrode to another on the back electrode. For the most commonly used cylindrical DMA, the relation between characteristic selected mobility Z^* and the operating and geometric parameters is given by(Knutson and Whitby 1975a)

$$Z^* = \frac{Q_{sheath} ln\left(\frac{R_2}{R_1}\right)}{2\pi VL} \tag{1.4}$$

where Q_{sheath} is the sheath flow rate maintained between the cylindrical electrodes, R_2 and $R_1$are the outer and inner cylinder radii, respectively. Irrespective of the DMA geometry, the selected mobility is inversely proportional to the voltage applied and proportional to the sheath flow rate (Rus et al. 2010a, Zhang et al. 1995). Also, irrespective of geometry, DMAs are imperfect instruments. The DMA transfer function

$\Omega(Z, Z^*)$ is the probability(Knutson and Whitby 1975a) that particles with mobility Z that enter the classification region of the DMA will be included in the classified (outlet) aerosol flow when the flow rate and applied voltage are for a characteristic mobility of Z^*. A perfect instrument would have a delta-function like transfer function. However, for DMAs, in the non-diffusive limit, that is, for large enough particles and large enough applied voltages, the transfer function spans in Z space the range of mobilities $Z^* - \Delta Z \leq Z \leq Z^* + \Delta Z$, where

$$\Delta Z = Z^* \beta \tag{1.5}$$

$$\beta = \frac{Q_{aerosol}}{Q_{sheath}} \tag{1.6}$$

In this non-diffusive limit, the shape of the transfer function is triangular(Knutson and Whitby 1975a) in the range of Z with its apex at Z^*. Diffusion of particles broadens this transfer function beyond its ideal limit. Stolzenburg developed an expression for this diffusionally broadened transfer function as(Stolzenburg and McMurry 2008):

$$\Omega(\tilde{Z}) = \frac{\tilde{\sigma}}{\sqrt{2}\beta}\left[\varepsilon\left(\frac{\tilde{Z}-(1+\beta)}{\sqrt{2}\,\tilde{\sigma}}\right) + \varepsilon\left(\frac{\tilde{Z}-(1-\beta)}{\sqrt{2}\,\tilde{\sigma}}\right)\right] \tag{1.7}$$

where

$$\varepsilon(y) = y\, erf(y) + \frac{1}{\sqrt{\pi}} e^{y^2} \tag{1.8}$$

$erf(y)$ is the error function, and

$$\tilde{\sigma}^2 = \frac{G}{Pe_{mig}}\frac{Z}{Z^*} \tag{1.9a}$$

$$\tilde{Z} = \frac{Z}{Z^*} \tag{1.9b}$$

where the Peclet number is particle migration across the gap between the electrodes and G is a parameter that depends weakly on the DMA geometry and on the flow rate ratio β. The broadening of the transfer function is captured by the variable $\tilde{\sigma}$ via Pe_{mig} (which is a measure of the directed motion of the particle due to the electric field to random thermal motion, i.e. diffusive motion).

Because (1) DMA transfer functions are particularly broad for sub-2 nm particles (with reduced transmission) and (2) the response of condensation particle detectors used conventionally in electrical mobility based sizing is poor for these particles, mass spectrometers are used in nanometer particle/cluster characterization.(Smith et al. 2010a, Zhao et al. 2010, Zhao et al. 2011) Mass spectrometry measures the mass-to-charge ratio of ions or charged clusters and with high resolution, aids in their chemical identification. However, this technique is not capable of direct size measurement. Often, their size is inferred from assumptions of a spherical particle and bulk density.(Almeida et al. 2013) To link DMA measurements and mass spectrometer measurements, characterization of the relationship between mass and mobility of particles in this size range is of interest.(Hogan and de la Mora 2011, Hogan Jr and De La Mora 2009) The coupling differential mobility analysis with mass spectrometry in series enables such characterization.(Rus et al. 2010a) Of particular interest, is combined differential

mobility analysis-mass spectrometry of particles/clusters with structures and chemical compositions resembling those detected in atmospheric nucleation events. Nucleation is the formation of stable clusters from molecular species that grow spontaneously by further uptake of vapor phase species. This process leads to new particle formation (NPF), that is, the formation of particles in the atmosphere from vapor phase species. The study of NPF events in field or laboratory settings involves characterization of clusters, which are molecular or ionic condensates, by various techniques such as Chemical Ionization Mass Spectroscopy (CIMS)(Zhao et al. 2010), and differential mobility analysis.(Smith et al. 2010a) In addition to the aforementioned issue of linking mass spectrometry measurements to size (to compare to DMA measurements), it is not clear that clusters measured in a mass spectrometer will not be structural modified by the measurement technique itself. Mass spectrometry involves the transmission of clusters across a large pressure drop (1 atm to a few torr) and includes manipulation by electric fields (acceleration by tens of volts) to focus analytes into beams. Clusters thus undergo high energy collisions with gas molecules in these non-equilibrium conditions and can fragment during measurements.(Kulkarni, Baron and Willeke 2011, Hogan Jr and De La Mora 2009) Such fragmentation can lead to misidentification of the original species involved and consequently results may be misinterpreted. The second part of this thesis hence employs a combination of an atmospheric pressure DMA coupled with a high-resolution mass spectrometer to study sub-2nm ions relevant to atmospheric NPF and to understand how such clusters can be affected by commonly used measurement techniques. The use of the atmospheric pressure measurement technique, namely, the

DMA is expected to prevent loss of information associated with cluster fragmentation events. This study also enables the investigation of mass-mobility relationship in the sub-2 nm regime.

The final step in size distribution measurement using electrical mobility based methods is the detection of particles (again, depicted in Figure 1.1). The particles examined are too small for direct optical detection. Therefore, their size is amplified by condensing vapor onto them in devices called condensation particle counters (CPCs).(McMurry 2000, Wilson 1912, Wilson 1897, Wilson 1911) Laminar flow condensation particle counters (CPCs) are devices in which nanoparticles are "grown" via condensation by exposure to supersaturated vapor in a "growth tube" and subsequently detected via light scattering.(Bricard et al. 1976, Agarwal and Sem 1980, Stolzenburg and McMurry 1991) All CPCs have activation efficiency curves, i.e. only a particular percentage of particles of a given size are activated to grow to larger sizes (and hence detected).(Hering and Stolzenburg 2005, Hering et al. 2005, Iida, Stolzenburg and McMurry 2009, Stolzenburg and McMurry 1991) These curves, which almost universally reveal decreasing activation with decreasing size, are strongly dependent on the saturation profile of condensable vapor in the CPC's growth tube. Accounting for the CPC activation efficiency curve, the overall response from the experimental scheme summarized in Figure 1.1 is the following(Kulkarni et al. 2011):

$$N = \sum_{z=1}^{\infty} \int_0^{\infty} f_z(d_p) \Omega_V(d_p, z) \eta_{CPC}(d_p) \frac{dn}{dd_p} dd_p \tag{1.10}$$

where N is the number concentration measured at the CPC, $f_z(d_p)$ is the fraction of particles of charge state z and size d_p, $\Omega_V(d_p, z)$ is the DMA transfer function for voltage setting V on the DMA, $\eta_{CPC}(d_p)$ is the size-dependent activation efficiency function of the CPC and $\frac{dn}{dd_p}$ is the size distribution function of the aerosol (which is the objective of the measurement). The summation runs over only positive charge states because the DMA is typically operated to isolate particles of a given polarity. From the measurement of N at different DMA settings (typically, different voltage settings as this is the easiest operating parameter to change), the size distribution function can be inferred from equation 1.10.

Just as ionization performance and DMA performance (in comparison to other isntruments) can be examined, CPC activation curves merit further study. The most widely used CPCs create supersaturation by cooling a saturated gas stream in a growth tube.(Bricard et al. 1976, Agarwal and Sem 1980) The saturation profiles are established by simultaneous heat and mass transport of vapor, and thus determined by vapor and gas properties and operational parameters like temperatures and flow rates. While a number of studies have been performed to examine the influence of changing the condensable vapor properties(Iida et al. 2009) and CPC operational parameters (namely, internal flow rates and temperatures)(Kuang et al. 2012, Barmpounis et al. 2018), what has not been examined is to what extent supersaturation for a given vapor, and hence activation efficiency curves, can be controlled via changing gas properties. Changing gas properties ultimately influences the Lewis number (the ratio of the gas thermal diffusivity to the

vapor mass diffusivity), the dimensionless ratio controlling differences in mass and heat transfer processes.(Stolzenburg and McMurry 1991, Metayer, Perrin and Madelaine 1982) Therefore, the Lewis number directly governs the supersaturation profile in a growth tube. The third portion of this thesis will focus on the heat and mass transfer influences in condensation; in this study, by varying ratios of He and N_2, which have high and low thermal diffusivities respectively, it will be demonstrated that activation efficiency curves in a CPC can be varied for 3-10 nm particles.

Finally, it is important to note that the DMA is not the only instrument enabling separation of charged particles/ions based upon electrical mobility. DMAs separate particles of different mobilities into different trajectories, with only particles of a specific narrow mobility window (closely spaced trajectories) being classified into the classified aerosol flow. A consequence of this separation is that the mean transit time of all mobilities is the same. Because the mean displacement of a Brownian walker is proportional to the product of diffusivity and time, this mode of separation leads to resolution degradation for smaller particles (i.e those with higher diffusivity).(Stolzenburg and McMurry 2008) Further, size distribution function measurement using DMAs require several minutes to complete voltage scans which can lead to signal smearing when aerosol being sampled varies at a faster rate (e.g. aircraft based atmospheric aerosol measurements, nebulized aerosol produced at the outlet of liquid chromatography systems etc). Electrical mobility analysis of sub-2 nm ions is often conducted by Drift Tube-Ion Mobility Spectroscopy (DT-IMS).(Dugourd et al. 1997, St. Louis and Hill 1990, Revercomb and Mason 1975) In DT-IMS, ions sampled at specific

times traverse along an electric field towards a detector; the transit time is inversely proportional to the ion mobility. All ions travel along similar trajectories, but arrive at the detector at different times in a mobility dependent manner and unlike DMAs do not require scanning in operational parameters like voltage. “The transit time for a particle being inversely proportional to its mobility or diffusivity(Mason and McDaniel 1988), the resolution of an ideal drift tube is independent of particle size.” (Revercomb and Mason 1975) DT-IMS for particles larger than 2 nm remains relatively poorly studied. Existing DT-IMS system mostly operate at reduced pressure and have high voltage inlet systems to charge particles for study.(Dugourd et al. 1997) Transmitting atmospheric pressure aerosols through these severe operating inlet condition could lead to alteration of the aerosol under study. The detector used in DT-IMS is often a Faraday plate detector that has low analyte sensitivity. Further, drift times in typical DT-IMS instruments are of the order of milliseconds, which is much faster than the response time of detectors (i.e. CPCs) used in the characterization of particles > 2 nm. Recently, Oberreit and co-workers overcame these limitations and developed a DT-IMS capable of atmospheric pressure sampling and detection of particles in the 2.2 to 11.1 nm size range with measurement times under 15 seconds.(Oberreit, McMurry and Hogan 2014) They did this by employing fluid mechanical gating instead of the conventionally used electrostatic gating in DT-IMS, using a fast-response time CPC (a far more sensitive detector) instead of the usually used Faraday plates.(Oberreit et al. 2014) The fourth part of this thesis delves into the extension of this technology up to 40 nm by increasing the electric field strength in the Oberreit drift tube and using a CPC with a faster response time than originally used.

In total, my dissertation provides new insights into the physics governing aerosol measurement systems and suggests that alternative or improved modes of measurement (better ion characterization for chargers, correction for dissociation in mass spectrometer measurements, modulation of CPC activation efficiency curves through gas composition modulation, and use of a DT-IMS in lieu of a DMA) may be useful in future aerosol measurements. The subsequent Chapters (2-5) describe the individual studies performed in this work. Each acts as a stand-alone document, and Chapters 2-4 (Maißer et al. 2015, Thomas et al. 2016, Thomas et al. 2018) are based upon published/submitted manuscripts (with the supplemental information from these manuscripts integrated into each Chapter). Because of this, each chapter contains is own abstract, introduction, methods, results & discussion, and conclusions section. Following Chapters 2-5, Chapter 6 provides an overview of the conclusions and future research prospects resulting from all performed studies.

Chapter 2: The Mass-Mobility Distributions of Ions Produced by a Po-210 Source in Air

Abstract: A differential mobility analyzer-mass spectrometer (DMA-MS) with a high resolving power (~45) parallel plate DMA was utilized to measure the masses and mobilities of positive and negative ions generated in dry, particle free air with a 10 mCi Po-210 α-irradiation source. I was able to chemically identify 6 positive ions and 25 negative ions in the spectra. The positive ions detected were generated by protonation, and included protonated acetone (59 Da), protonated bis-(2-ethylhexyl)phthalate (391 Da), and protonated cyclic polydimethylsiloxanes. The negative ions detected were all deprotonated, and included Teflon-derived perfluoralkanoate ions, long chain alcohol derived alkoxide ions, and the nitrate ion, which, despite its low mass and high mobility was the most abundant ion in negative spectra. Most detected ions can be traced back to system components or to compounds used in the manufacture of system components. Though clearly the detected ions are system specific, the conditions employed were similar to those used in many laboratory scale aerosol measurement systems. The mobility-mass relationship for measured ions was compared to prior mass-mobility measurements of ions produced via α-irradiation, as well as to the predictions of gas molecule scattering calculations, which took as inputs semi-emipirical AM1 based structural models. Through this comparison it is shown that (1) a universal mobility-mass relationship cannot be applied to all ions and (2) for most ions, gas molecule

scattering with diffuse scattering rules can be used to accurately predict ion mobilities.

2.1 Introduction

A number of aerosol measurement techniques are based on determination of the electrical mobilities of particles (Knutson and Whitby 1975a, Wang and Flagan 1990), with subsequent inference of particle sizes and concentrations from the detected signal as a function of mobility. Mobility measurements themselves, as well as accurate determination of particle concentrations in mobility measurements, are thus dependent upon imparting a known charge distribution to an aerosol. Overwhelmingly, this distribution is the steady-state charge distribution (i.e. the bipolar charge distribution) arising due to diffusion charging when particles are exposed to nearly equal concentrations of positive and negative ions (Gopalakrishnan, McMurry and Hogan 2015a Scheibel and Porstendörfer 1983, Reischl et al. 1996, Wiedensohler et al. 1986). Gas phase bipolar ion production is hence an important aspect of aerosol measurements. A commonly used approach to bipolar ion production is with radioactive materials, which emit either alpha (Po-210, Am-241) or beta radiation (Ni-63, Kr-85) (Liu and Pui 1974), or with the use of low frequency x-ray sources (Lee et al. 2005). These materials/sources produce roughly equal concentrations of positive and negative ions *via* direct ionization of gas molecules (which lose an electron through direct interaction with the radiation) and subsequent attachment of the produced electrons to neutral gas molecules. In spite of the consistency of ion production, typically, the chemical composition of the ions generated is left uncontrolled in bipolar ion sources, and as recent work demonstrates

(Steiner et al. 2014, Steiner and Reischl 2012) the ion composition undoubtedly varies from system to system (i.e. in different laboratory or field environments). Unfortunately, ambiguities in the chemical composition and properties (mass and mobility) of ions lead to direct ambiguities in the resulting bipolar charge distribution, as the charge distribution is a function of ion properties (Wiedensohler and Fissan 1988, Wiedensohler and Fissan 1990, Wiedensohler and Fissan 1991, Gopalakrishnan et al. 2015, Gopalakrishnan et al. 2013b, Tigges, Jain and Schmid 2015).

Measurement of the properties of ions produced by radioactive sources is of considerable interest not only because of their application in diffusion charging, but also to better understand how ion structure links to mobility. Charging ions, which are <1000 Da in mass and below ~2.0 nm in characteristic size (with rare exceptions) are typically smaller than the particles which are examined by mobility analysis. However, recent interest in new particle formation in both ambient aerosol (Jiang et al. 2011b) and in laboratory settings (Almeida et al. 2013, Jen, Hanson and McMurry 2014) has led to the application of mobility measurement to the analysis of sub 2.0 nm clusters, formed from vapor phase precursors and composed of <100 molecules. With mobility measurements alone (i.e. without direct mass measurement coupled with mobility measurements), it is necessary to have a model linking mobility to an effective cluster/particle size to infer structural information for such entities. Although typically the Stokes-Millikan equation (Larriba et al. 2011), modifications to it (Tammet 1995, Larriba and Hogan 2013, Fernández-García and Fernández de la Mora 2013, Mäkelä et al. 1996b), or regression equations (Mäkelä et al. 1996) based upon the measurements of Kilpatrick (1971) are

applied for this purpose, it is not clear to what extent these relationships are valid in the sub 2.0 nm size range for a variety of species, and in fact, there is evidence that such simple relationships cannot be applied in all circumstances (Ouyang et al. 2013, Larriba-Andaluz et al. 2015). Simultaneous mass-mobility measurements for < 2.0 nm ions, with clear identification of ion structure, would make clearer to what extent simple relationship linking ion mobility and size can be invoked, and under what circumstances more detailed calculation procedures (considering ion structure (Shvartsburg et al. 2007, Larriba and Hogan 2013, Larriba-Andaluz and Hogan 2014)) are needed.

Ion mobility spectrometry-mass spectrometry (IMS-MS) facilitates simultaneous measurement of ion mobility and mass and is well suited for characterization of bipolar ions. IMS-MS has been applied to ions generated by radioactive sources to detect explosives and specific vapor phase ions (Steiner et al. 2006, Kanu et al. 2008); thus, the composition of the ions in these studies was well-controlled and dissimilar from the conditions typically found in aerosol measurement systems. More recently, attempts have been made to use IMS-MS (with differential mobility analyzer/DMA for IMS (Rus et al. 2010b)) for measurement of the mass and mobilities of negative ions produced by Am-241 source in N_2 and air (Steiner et al. 2014). Though this work enabled identification of some ions and their corresponding mass and mobilities, complete, three-dimensional spectra (signal intensity as a function of mass and mobility) were not reported, and further aspects of IMS-MS measurement such as (1) ion fragmentation subsequent to IMS measurement and (2) charge exchange (charge stealing) between ions and neutral

molecules both within the DMA and subsequent to DMA measurement were not considered in data analysis, though likely occurred during measurement.

Therefore, in this work, differential mobility analysis-mass spectrometry (DMA-MS, with a SEADM P5 DMA and a time-of-flight mass spectrometer) is applied to tandem mobility-mass measurements of both positive and negative ions generated in air using a 10 mCi Po-210 source. Though the ions detected in such experiments are clearly system specific, we remark that the components and gases used in the reported experiments are similar to those frequently applied in laboratory scale aerosol measurements. In addition, we have reported preliminary measurements along these lines previously (Gopalakrishnan et al. 2015, Gopalakrishnan et al. 2013b); however, unique in this work, for many of the ions detected, specific chemical compositions are identified and structure calculations are performed at the semi-empirical AM1 level (Dewar et al. 1985, Stewart 1989) to infer local energy minimum structures for these ions. Subsequently, the inferred structures are used with recently developed mobility calculation procedures (Larriba and Hogan 2013a, Larriba and Hogan 2013c) to predict mobilities and directly compare to measurements. This approach is contrasted with simpler regression-based approaches to link ion mass and mobility.

2.2 Experimental Methods

As is described in detail previously (Gopalakrishnan et al. 2015), mobility and mass measurements were carried out using a parallel-plate DMA (P5, SEADM, Boecillo, Spain) operated in tandem with a QSTAR XL quadrupole-time-of-flight mass

spectrometer (qTOF-MS, MDS Sciex). A detailed description of the parallel-plate DMA and its operation in series with a mass spectrometer is provided in Rus et al. (2010). Figure 2.1 shows a schematic of the DMA-MS as applied in this study. Similar to the measurements performed by Gopalakrishnan et al (2015), the Po-210 alpha particle source (a 10 mCi Nucleospot source, TSI, St. Paul, MN) used for bipolar ion production was placed in a Teflon chamber that was attached directly to front plate of the DMA. A flow of 0.8 lpm (liters per minute) of ultra-high purity "zero" air (Airgas Inc.) was passed through the Teflon housing and into the DMA inlet. To facilitate ion transport, a potential difference of ~1 kV was applied between the metallic Po-210 holder and the front plate of the DMA. The DMA was operated in recirculating mode. The voltage applied to the front plate of the DMA was stepped in 10 V increments, and ions were transmitted through the DMA outlet at flow rate of 0.5 lpm. The remaining 0.3 lpm left the DMA sheath flow loop through an overflow outlet. While the operation of DMA model P5 with counterflow at the inlet enables DMA resolving powers close to 70, in the co-flow mode applied here the resolution was reduced to ~45; this value is still significantly greater than the resolving powers achievable with commercial DMAs in the mobility range of interest (Jiang et al. 2011c). The DMA was calibrated as performed in prior studies, by electrospraying a methanol solution of tetraheptylammonium bromide and determining the voltage of maximum transmission for the tetraheptylammonium cation, whose mobility near the measurement temperature is provided by Ude & Fernandez de la Mora (2005). The mass of the most abundant tetraheptylammonium cation was also used in mass spectrometer calibration.

For each potential difference applied across the DMA electrodes, a mass spectrum in the 10-2000 Da range was measured using the time of flight section (resolving power of ~8000) of the QSTAR XL mass spectrometer, with the quadrupole filters operated in transmission (RF only) modes. To directly assess the influence of ion dissociation in the mass spectrometer inlet on results (i.e. neutral or charge loss between the DMA and time of flight tube (Hogan and Fernandez de la Mora 2010, Larriba, Fernandez de la Mora and Clemmer 2014, Ouyang et al. 2013), we varied the declustering potential (DP) between the DMA outlet and the skimmer in the inlet of the mass spectrometer from 0 to +/- 100 V (for positive and negative ions, respectively). Between measurements, the DMA was cleaned periodically by opening up the front plate and washing both electrodes with both HPLC grade acetone and methanol.

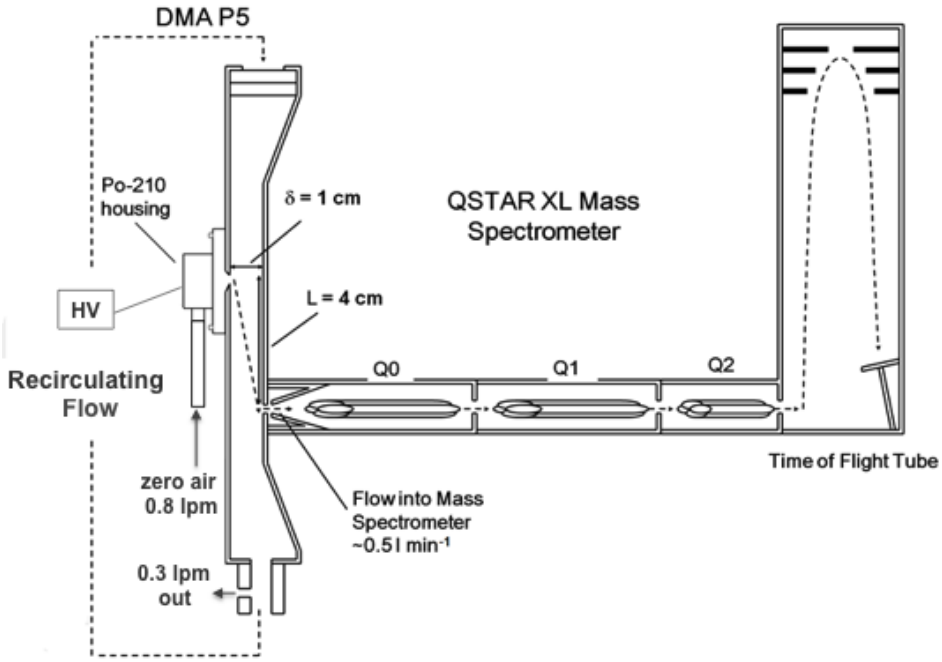

Figure 2.1. A schematic of the parallel plate DMA-MS system used in measuring the mass and mobility of Po-210 generated ions in dry air.

2.3 Results and Discussion

2.3.1 Mobility-Mass Spectra & Ion Identification

First and foremost, I report the multidimensional mass-mobility spectra for detected ions. Figures 2.2 a & 2.2 b display contour plots of the mass spectrometer-based signal intensity as a function of both mass to charge ratio as well as inverse mobility (in V s cm^{-2}, inferred from DMA calibration) for positive and negative ions, respectively. The presented results were obtained without a declustering potential applied in the mass spectrometer inlet. Relative signal intensity is denoted *via* a color scale from blue to red on a logarithmic basis. Specific ions are identified *via* line segments whose lengths are defined by the resolving power of the DMA. All detected ions are found to be singly charged. In interpreting contour plots, it is important to consider the possibility of ion dissociation after DMA classification but before mass measurement, as well as charge exchange collisions between a neutral molecule and an ion in the DMA. The former will lead to the appearance of ions at the mass to charge ratio of the product(s), but the inverse mobility of the parent ion (Hogan and Fernandez de la Mora 2010). Meanwhile, the latter will lead to longer line segments at the mass of the ion accepting charge, and line segment lengths defined by the inverse mobility difference between the charge donating and charge accepting ion. Without obtaining complete mobility-mass spectra, it is difficult to clearly identify dissociation and charge exchange reactions, and both may have been present in related ion measurements reported elsewhere (e.g. in the measurements of Steiner et al (2014), the ions $C_9H_{10}O_2(HCl)(HNO_3)NO_3^-$, $C_9H_{10}O_2(HNO_3)NO_3^-$, and $C_9H_{10}O_2NO_3^-$ all appear at the same mobility, suggesting

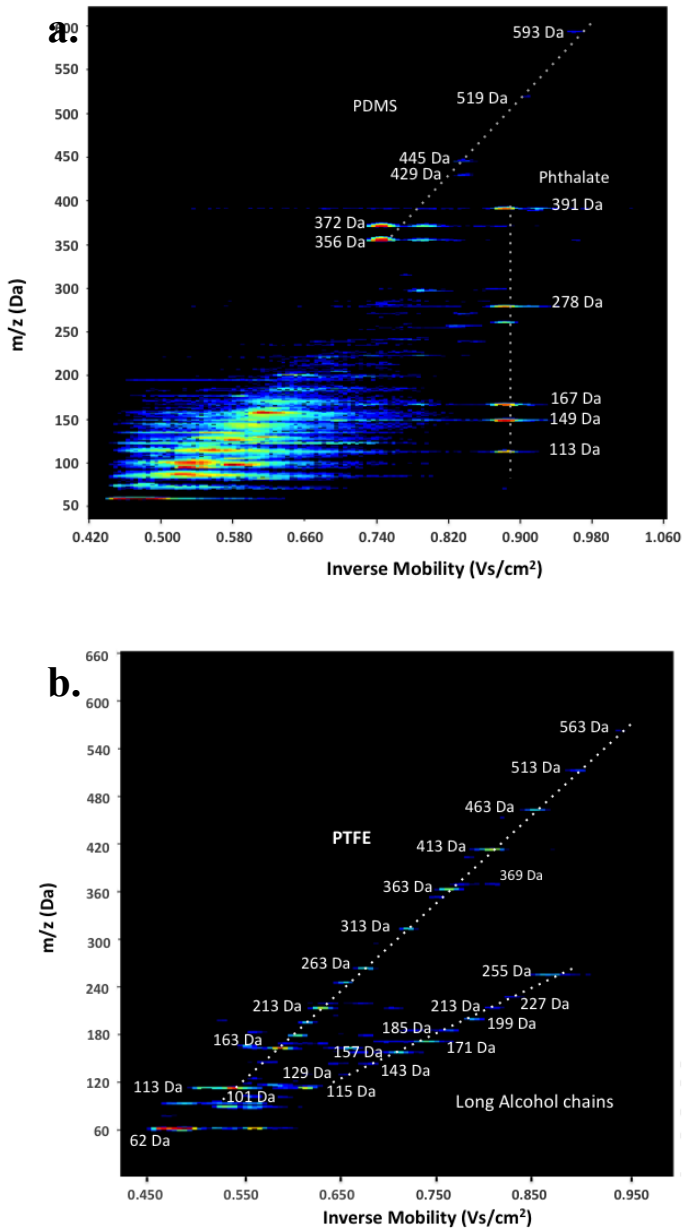

Figure 2.2. Contour plots displaying signal intensity as a function of mass to charge ratio and inverse mobility for **(a)** positive ions and **(b)** negative ions generated in ultrahigh purity zero air. Selected classes of ions are labelled by their presumed origin. In the positive ions spectrum, PDMS denotes protonated cyclic-polydimethylsiloxane ions, and phthalate denotes parent (protonated) and product ions deriving from Bis-(2-ethylhexyl)phthalate. In the negative ion spectrum, PTFE denotes perfluoroalkanoate ions, which derive from polytetrafluoroethane. The "long alcohol chains" label applies to alkoxide ions, and the the peak for nitrate (NO_3^-, 62 Da) is also labelled in the negative spectrum.

that the latter two ions form *via* dissociation in the mass spectrometer inlet).

Ion chemical composition in several instances can be identified from the ion's exact mass (which is inferable because of the resolution of the time-of-flight mass spectrometer applied). Ion identification is further facilitated through comparison to ions detected in prior studies (Keller et al. 2008), as well as knowledge of the chemical compositions of system components. Focusing first on the positive ion contour plot, a high signal intensity line segment appears at a nominal mass of 391 Da, and is identified as protonated bis-(2-ethylhexyl)phthalate, $C_{24}H_{38}O_4H^+$ (denoted as phthalate). Phthalates are used as plasticizers in a wide range of applications, and in our experiments possible sources include any and all polymeric materials (e.g. Teflon and Nylon ferrules). It is highly likely this ion would be found in other laboratory environments where such materials are utilized. At an identical mobility to the phthalate 391 Da ion, a number of smaller mass species are also detected; as noted above, these ions arise due to fragmentation of the parent phthalate ion. The fragmentation products observed for the 391 Da phthalate ion have been noted previously (Jecklin, Gamez and Zenobi 2009), and include protonated 1,2-benzendicarboxylic acid ($C_{16}H_{22}O_4H^+$, 279 Da) as well as phthalate esters with saturated alkyl side chains (at 149 Da). Fragmentation between the DMA and mass spectrometer is confirmed by applying a declustering potential of 100 V; in Figure 2.3a the mass spectrum at an inverse mobility of 0.88 V s cm^{-2} is plotted for both DP = 0 and DP = 100V conditions. Clearly evident is the increase in signal intensity for the 149 Da ion at the expense of both the parent ion and the other fragmentation products with the application of declustering potential.

Also of high signal intensities at higher masses in the positive ion spectrum are a number of ions corresponding to protonated polydimethylsiloxanes (PDMS, $(C_2H_6OSi)_nH^+$, with n =*5-8* discernable. PDMS ions are also labeled in figure 2.2a, and differ in mass from one another by 74 Da. Such ions are frequently encountered contaminants in mass spectrometry (Keller et al. 2008), as PDMS is the main component of silicone rubber, is used in surfactants and defoamers, and is incorporated into most O-rings (used in sealing the DMA). Like phthalates, PDMS ions are hence difficult to avoid in measurement systems (Timko et al. 2009, Yu et al. 2009). While the noted chemical formula accurately describes the detected ions, the precise structure of the PDMS ions is not clear; a likely possibility (as noted) is that the PDMS ions are cyclic with an excess proton bound (Schneider, Sablier and Desmazières 2008). For several PDMS ions, also observed is dissociation between the DMA and mass spectrometer; specifically, the $n = 5$ and $n = 6$ ions are observed to lose a neutral CH_4 (16 Da), which may occur *via* a rearrangement reaction (Ballistreri, Garozzo and Montaudo 1984).

Finally, positive ion spectra reveal considerable number of ions with masses less than 100 Da and with inverse mobilities less than 0.7 V s cm^{-2}. These ions are difficult to identify clearly in mobility because of the prevalence of charge exchange reactions within the DMA (such as by the 149 Da phthalate fragment), though they appear to be organic ions. Identifiable among these organic ions is the protonated acetone peak, $C_3H_7O^+$, with a mass of 59 Da.

The negative ion spectrum is considerably clearer than the positive ion spectrum at low mass; the most prominent line segment appears at 62 Da and corresponds to the

nitrate ion (NO_3^-). The nitrate ion was similarly detected by Steiner *et al* (2014), and was only observed to diminish in concentration upon cleaning of their ion source chamber. The nitrate ion's abundance over all other negative ions is attributable to the high gas phase acidity of nitric acid (Exner and Böhm 2005); this leads to the contrasting appearance of negative ion spectra to positive ion spectra, in which it appears that without intentionally doping the gas, no low mass species (< 100 Da) of high gas phase basicity dominates in abundance over other ions.

In the contour plot for negatively charged ions at higher mass, two dominant families of ions are also evident, and are denoted *via* white dashed lines in figure 2b. The higher mass line corresponds to perfluoroalkanoate ions, which derive from polytetrafluoroethylene (PTFE, i.e. Teflon, which has a 50 Da repeating group). These ions all have the structure CF_3-$(CF_2)_n$-COO^-, with $n = 0$-10 identified. Presumably, perfluoroalkanoate ions derive directly from the Teflon housing of the Po-210 source applied, and were likely released into the gas phase because of incident α-irradiation on the housing itself (leading to depolymerization of longer chain PTFE). It is not clear to what extent this depolymerization would occur for other bipolar ion production systems; in the present study the use of a non-conducting housing material was essential to direct ions electrostatically into the DMA. The lower mass series, appearing in the same mobility range, is found to correspond to alkoxide ions of the form CH_3-$(CH_2)_n$-O^- (14 Da repeating group). Such ions likely derive from long alcohol chains present in the system, and we are able to identify ions ranging from deprotonated hexanol ($n = 5$, hexoxide) up to deprotonated nonadecanol ($n = 18$, nonadecoxide). In our system, these

long alcohol chains have been traced back to a polishing cream used periodically on the DMA electrodes, and they are commonly used as emulsifiers. For this reason, they too would be commonly encountered in laboratory settings and alcohol derived ions may be present in other experiments. The ions deriving from PTFE and alcohols exhibit near linear increases in inverse mobility with mass, suggesting that all such ions adopt non-spherical, chain-like structures in the gas phase (Larriba and Fernandez de la Mora 2012).

Dissociation was also observed to occur for negative ions with increasing declustering potential applied. Figure 3b displays a negative ion mass-mobility contour plot with DP = 100 V. For PTFE derived perfluoroalkanoate ions, declustering leads to a mass loss of 44 Da, which corresponds to decarboxylation (Maestri et al. 2006). In case of the alcohol derived alkoxide ions, the line segments are increased in length, indicating that declustering leads to loss of $(CH_2)_n$ units. This observation underlines the importance of careful interface between the ion mobility measurement and the mass measurement when intending to study mass – mobility relationship, as the relationship can be significantly biased *via* dissociation reactions. For example, in this instance dissociation lead to a shift of ~5% in the apparent inverse mobilities of perfluoroalkanoate ions, which is a systematic error well above the resolving power of the instrument. At the same time, controlled ion dissociation can be a useful tool for the chemical identification of ions; here the phthalate ion was identified through its characteristic fragment products (Stein 2015).

2.3.2 The Mobility-Mass Relationship

In total, after considering dissociation reactions, the masses, mobilities, and structures of 6 positive ions and 25 negative ions were identified, all of which appear to be ionized *via* either protonation or deprotonation. The names, chemical formulae, masses, mobilities (at 300 K and atmospheric pressure), and mode of ionization for of all identified ions are provided in Table 2.1. In large part, ions appear to derive from tubing components and materials used in system component manufacturer. These chemicals may be present in the gas phase in sub-ppt levels (part per trillion; at standard conditions 1 part per trillion is ~2.4 x 10^{13} m^{-3}, which is near the total ion concentration produced by commonly applied radioactive sources) and still be the most abundant ions produced. It is reiterated that many of the ions deriving from these compounds are likely to be detected in other laboratory environments as well. Atomic ions or molecular ions of oxygen or nitrogen are not detected (though the experimental system has the capability to do so); presumably such ions would lose charge upon collision with the organic vapor phase precursors for the ions detected here. It is also noted that the mass of the polymeric species detected are higher than the average mass and mobilities used in charge distribution calculations (Wiedensohler 1988). Beyond identification, of interest is comparison of the mobility versus mass relationship for the different species detected, and comparison of the results obtained here to previous studies. In approximating ions as spheres, as noted in the introduction section, one approach has been to assume bulk density for ions and apply the Stokes-Millikan equation (Ku and de la Mora 2009, Larriba et al. 2011), with a correction

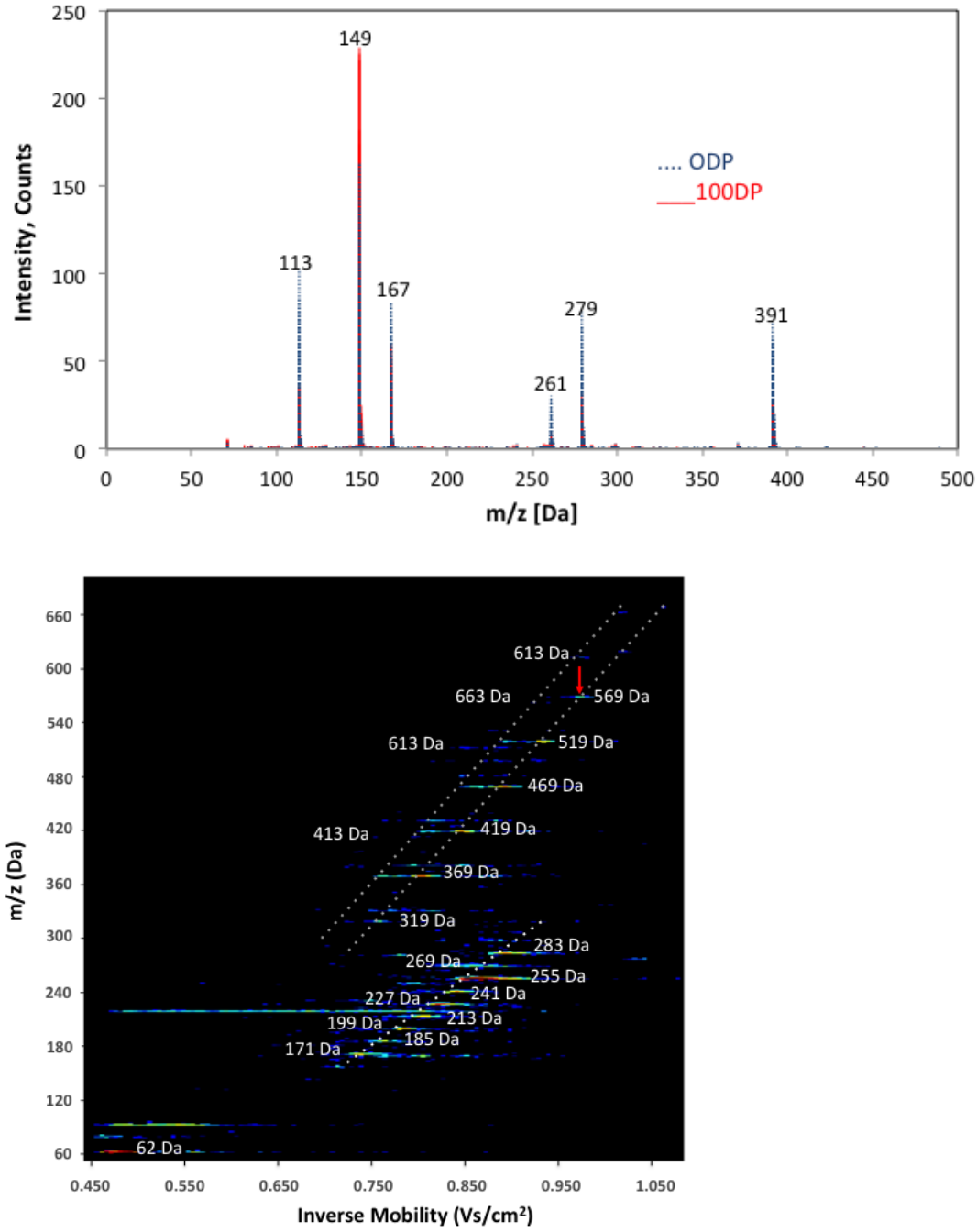

Figure 2.3. **(a.)**The mass spectrum for positive ions at an inverse mobility of 0.88 V s cm^{-2} with DP = 0 and DP = 100. **(b.)** A contour plot for negative ions with DP = 100 V.

factor introduced to account the influence of the ion induced dipole potential between gas molecule and the ion (Ouyang et al. 2013b, Tammet 1995, Larriba and Hogan 2013c, Fernández-García and Fernández de la Mora

2014, Fernández-García and Fernández de la Mora 2013). However, as noted in the previous section, a near linear-relationship is observed between mass and inverse mobility for several ions types; prior studies show clearly (Larriba and Fernandez de la Mora 2012) that a linear mass-inverse mobility relationship is expected for chain-like ions, as opposed to spheres. For this reason, the Stokes-Millikan equation is not applied in comparison to results (i.e. its requisite assumptions are not met). A second approach is to compare to the measurements of Kilpatrick (1971), who reported the masses and mobilites of both positive and negative ions in the 35 to 2211 Da range (in air and N_2). A fit curve (extrapolating to 300 K) to these results was provided by Mäkelä et al (1996a):

$$Z = exp\,[-0.0347(ln\ (m_i)\ )^2 - 0.0376\ ln\ (m_i)\ + 1.4662] \qquad (2.1)$$

where m_i is the ion mass (in Da) and Z is the ion mobility (in $cm^2\ V^{-1}\ s^{-1}$). In figure 2.4, we plot the mobility for all 31 identified ions as a function of mass, and also plot the predictions of equation (1). Further plotted are the results of Steiner et al (2014). It is found that the sub 100 Da ions (protonated acetone and nitrate) as well as alkoxide ions agree well with the Kilpatrick regression curve. However, for all other polymeric ions, a substantial deviation from the Kilpatrick curve is evident, with both PDMS and perfluoroalkanoate ions exhibiting higher mobilities than anticipated by the regression equation. In contrast to the identified ion types here, the mass-mobility results for the ions reported by Steiner et al. (generated by an Am-241 source in N_2, a 1:1 mixture of N_2 and

air and in filtered lab air and 30% relative humidity) are considerably more scattered. While, again, these results have been influenced by dissociation and charge exchange, overall, combining the results of both studies shows that it is not always appropriate to apply a universal mass-mobility relationship, as mobility is primarily a function of ion structure (not mass). In fact, issues in data interpretation will arise when misapplying the Kilpatrick regression equation. For example, a recent study (Fang et al. 2014) reports the masses of clusters ions possibly containing Si and Ti (deriving from flame synthesis reactors); these masses were estimated from mobility measurements by applying the Kilpatrick regression equation. This curve is undoubtedly inaccurate for ions containing such heavy elements, leaving the chemical identities of the ions detected ambiguous.

2.3.3 Scattering Calculation Predictions

In the free molecular (Knudsen number, $Kn \rightarrow \infty$) regime, in which gas phase nanometer scale ions at atmospheric pressure and room temperature reside, an ion's mobility can be directly linked to its collision cross section *via* the Mason-Schamp equation (Mason and McDaniel 1988):

$$Z = \frac{3ze}{4\rho_{gas}} \sqrt{\frac{\pi}{8kT}\left(\frac{m_i m_g}{m_i + m_g}\right)} \frac{1}{\Omega} \qquad (2.2)$$

where z is the ion charge state (integer value), e is the unit electron charge, kT is the thermal energy (the product of Boltzmann's constant and the temperature), m_i is the ion mass, m_g is the background gas mass, and Ω is the collision cross section. Recently,

Table 2.1. A summary of the names, formulae, nominal masses, mobilities (at 300 K and 1 bar), possible structures, and mode of ionization for chemically identified ions in this study.

Name	Chemical Formula	Nominal Mass [Da]	Mobility [$cm^2 V^{-1}s^{-1}$]	Structure	Ionization Mechanism
Acetone (Protonated)	$C_3H_7O^+$	59	2.18		protonation
Nitrate	NO_3^-	62	2.16		deprotonation
Hexoxide	$CH_3(CH_2)_5O^-$	102	1.72		deprotonation
Octoxide	$CH_3(CH_2)_7O^-$	130	1.51		deprotonation
Nonoxide	$CH_3(CH_2)_8O^-$	144	1.46		deprotonation
Decoxide	$CH_3(CH_2)_9O^-$	157	1.40		deprotonation
Undecoxide	$CH_3(CH_2)_{10}O^-$	171	1.36		deprotonation
Dodecoxide	$CH_3(CH_2)_{11}O^-$	185	1.31	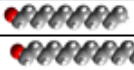	deprotonation
Tridecoxide	$CH_3(CH_2)_{12}O^-$	199	1.27	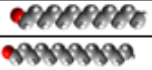	deprotonation
Tetradecoxide	$CH_3(CH_2)_{13}O^-$	213	1.23	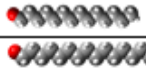	deprotonation
Pentadecoxide	$CH_3(CH_2)_{14}O^-$	227	1.20		deprotonation
Hexadecoxide	$CH_3(CH_2)_{15}O^-$	241	1.19		deprotonation
Heptadecoxide	$CH_3(CH_2)_{16}O^-$	256	1.16	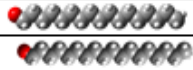	deprotonation
Octadecoxide	$CH_3(CH_2)_{17}O^-$	269	1.14	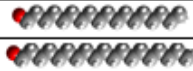	deprotonation
Nonadecoxide	$CH_3(CH_2)_{18}O^-$	284	1.12		deprotonation
Perfluoroethanoate	CF_3COO^-	113	1.85		deprotonation
Perfluoropropanoate	$CF_3(CF_2)COO^-$	163	1.70		deprotonation
Perfluorobutanoate	$CF_3(CF_2)_2COO^-$	213	1.59		deprotonation
Perfluoropentanoate	$CF_3(CF_2)_3COO^-$	263	1.49		deprotonation
Perfluorohexanoate	$CF_3(CF_2)_4COO^-$	313	1.39		deprotonation
Perfluoroheptanoate	$CF_3(CF_2)_5COO^-$	363	1.31		deprotonation
Perfluorooctanoate	$CF_3(CF_2)_6COO^-$	413	1.23		deprotonation
Perfluorononanoate	$CF_3(CF_2)_7COO^-$	463	1.13		deprotonation
Perfluorodecanoate	$CF_3(CF_2)_8COO^-$	513	1.12		deprotonation
Perfluoroundecanoate	$CF_3(CF_2)_9COO^-$	563	1.06	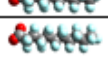	deprotonation
Perfluorododecanoate	$CF_3(CF_2)_{10}COO^-$	613	1.01	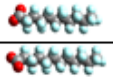	deprotonation
Bis(2-ethylhexyl) phthalate (protonated)	$C_{24}H_{39}O_4H^+$	391	1.13		protonation
cyclo-penta(dimethylsiloxane)	$(C_2H_6OSi)_5H^+$	371	1.27		protonation
cyclo-hexa(dimethylsiloxane)	$(C_2H_6OSi)_6H^+$	445	1.20		protonation
cyclo-hepta(dimethylsiloxane)	$(C_2H_6OSi)_7H^+$	519	1.10		protonation
cyclo-octa(dimethylsiloxane)	$(C_2H_6OSi)_8H^+$	593	1.04		protonation

Larriba-Andaluz (Larriba and Hogan 2013a, Larriba and Hogan 2013c, Larriba-Andaluz and Hogan 2014) has developed a suite of algorithms to calculate directly collision cross sections (and hence mobilities for known mass ions) for ions in diatomic gases, which is distinct from prior approaches (developed primarily for measurements in Helium (Shvartsburg et al. 2007)). These algorithms, which have been tested/utilized in a number of circumstances (Kumar et al. 2014, Larriba-Andaluz et al. 2015, Ouyang et al. 2013, Jen et al. 2014), are contained within the IMoS computation package (freely available from Dr. Carlos Larriba-Andaluz) and enable comparison of predicted mobilities to measurements in a much more rigorous manner than the use of empirically derived mass-mobility relationships. The IMoS algorithms take as inputs all-atom candidate structures for ions, the locations of charges on ions, and either atomic radii or Lenard-Jones parameters for gas molecules and the atoms within ions. The collision cross section for each examined ion is inferred directly from the rate of momentum transfer from individual gas molecules (determined from gas molecule trajectory simulations), and the influences of both the induced dipole potentials and Lenard-Jones potentials on gas molecule trajectories can be considered.

The IMoS calculation algorithms were applied here for comparison to measurements. To obtain a candidate structure for each ion, the Gaussian 09 software package (Gaussian Inc., Wallingford, CT) was used to infer local energy minimum candidate structures. A single candidate structure was used for each ion; prior work demonstrates that the collision cross section is not sensitive to small changes in ion structure, hence local minimum structures are typically sufficient for collision cross

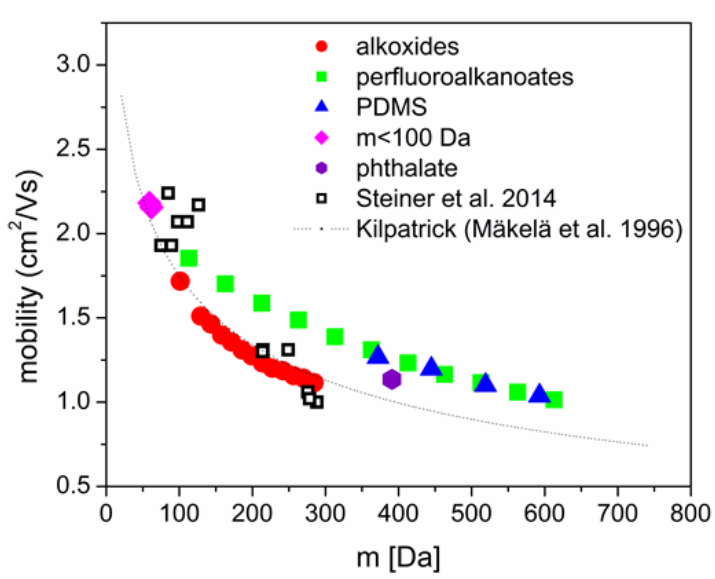

Figure 2.4. A plot of the measured mobility versus mass for all chemically identified ions in this study. Results from Steiner et al (2014) and a regression equation to the results of Kilpatrick (1971) are also provided for comparison. m < 100 Da refers to protonated acetone and nitrate.

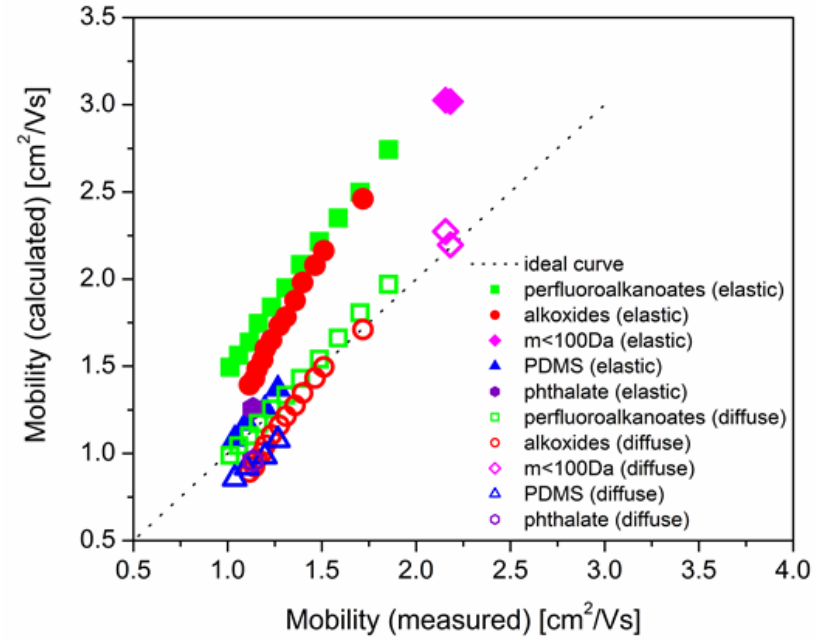

Figure 2.5. Comparison of measured and calculated mobilities for all chemically identified ions using both DHSS (diffuse) and EHSS (elastic) scattering rules.

section calculations. The AM1 semi-empirical parameterization (Dewar et al. 1985) was employed, symmetry restrictions were not applied, and vibration frequencies were calculated. The resulting structures are depicted in table 2.1 (with atomic radii proportional to the van der Waals radii). All structures presented showed positive frequencies, indicating they are truly local minima structures rather than transition states.

IMoS calculations are described in detail in prior reports (Larriba and Hogan 2013a, Larriba and Hogan 2013c). Gas molecules were modeled as spheres with radii of 0.15 nm and a polarizability of 1.7×10^{-30} m^3. Excess charges were placed at specific locations on all ion structures (the site of protonation/deprotonation) and each atom was represented as a hard sphere with a radius equivalent to its van der Waals radius. Using the noted polarizability, the influence of the ion-induced dipole on gas molecule trajectories was considered. Two types of calculations were performed: (1) diffuse hard spheres scattering calculations (DHSS), in which incident gas molecules onto an ion were reemitted from the ion surface at a random angle and velocity sampled from a Maxwell-Boltzmann distribution (slightly temperature reduced) and (2) elastic hard sphere scattering calculations (EHSS), in which incident gas molecules were emitted from the ion surface at specular angles, with their translational kinetic energies conserved. The DHSS approach leads to results in excellent agreement with the measurements of Millikan (1923) and with measurements of organic ions in diatomic gases (Larriba and Hogan 2013c, Larriba-Andaluz et al. 2015b), while the EHSS approach has found good agreement with measurements in helium (Shvartsburg and Jarrold 1996), and better agreement with ions composed of heavy elements (e.g. cesium iodide) in air (Ouyang et

al. 2013b). These two collision models arise because of the use of frozen ion structures in calculations and lead to results which are 10-30% different from one another. Comparison of both to measurements is hence critical to understand how ion mobility is linked to ion structure.

DHSS and EHSS calculated mobilities are plotted as functions of the measured mobilities for all ions in Figure 2.5 (open symbols: DHSS, closed symbols: EHSS). The dashed black line indicates 1:1 agreement between measurements and theory. For nearly all ions, i.e. the protonated acetone ion, nitrate, small alkoxide ions, and perfluoroalkanoate ions, DHSS calculations are in excellent agreement with measurements (we remark that there are no fit parameters in calculations), while EHSS calculations lead to drastic overestimation of mobilities. For the alkoxide ions, increasing deviation between DHSS predictions are evident with increasing chain length (i.e. for lower mobility structures). This deviation arises because the input structures for DHSS calculations were straight chains; through molecular dynamics (MD) simulations, it is found that such long chains are not necessarily straight at 300 K, hence the predictions are lower limits for the alkoxide ion mobilities. Better agreement between measurements and predictions is brought by sampling structures from MD simulations (Larriba and Hogan 2013c).

For the protonated phthalate ion as well as the cyclic PDMS ions, results are intermediate to both calculation procedures, and in slightly better agreement with EHSS calculations. For the PDMS ions, this observation is in line with the findings of Ouyang et al (2013) and Larriba-Andaluz et al (2015); both of these studies find systematically

that for ions composed of atoms heavier than the impinging gas molecules, gas molecule ion collisions are more specular in nature. However, the agreement between EHSS calculations and the phthalate ion measured mobility was not anticipated based upon prior work. It can be speculated that the perceived specular nature of collisions for PDMS and phthalate ions may have to do with the planar structures of these ions, but future work will be necessary to better understand why measurements for these ions disagree with DHSS calculations. Despite the disagreement found for these ions, it is found overall that the use of IMoS calculations enables reasonably accurate predictions of ion mobilities from structural models and advocate their use in comparing calculations of ion structures to mobility measurements in diatomic gases.

2.3.4 Expected Bipolar Charge Distribution

The work in this section was done by Dr. Anne Maisser, the leading author on the published journal article this chapter is based on. This section is included in this thesis for completeness. The diffusion charging of aerosol particles occurs *via* collisions between ions and particles. After a certain time, in a properly designed bipolar charger (de La Verpilliere, Swanson and Boies 2015, Hoppel and Frick 1990, Alonso and Alguacil 2003), a steady-state charge distribution is reached, which is typically the desired charge distribution for electrical mobility based size distribution measurements. The steady-state charge distribution can be calculated as function of particle size by solving a system of population balance equations, as described in detail in numerous previous studies (Fuchs 1963a, Reischl, Scheibel and Porstendörfer 1983, Wiedensohler and Fissan 1990).

However, the difficulty involved in solving such equations increases drastically if polydisperse ion properties are considered; the particle-ion collision rate for each ion type and each particle charge state must be considered. As an alternative, Gopalakrishnan et al (2013b) developed a Brownian dynamics based approach to steady-state charge distribution determination, which has been found to agree reasonably well with measurements (Gopalakrishnan et al, 2015). Uniquely, the computation time with this approach is influenced negligibly by considering polydisperse ion distributions, and this approach is invoked here to determine the expected charge distribution arising from the chemical identified ions. Details on the calculation method are provided in prior reports (Gopalakrishnan et al. 2013b, Gopalakrishnan et al. 2015a). For the results reported, < 100 Da ions (protonated acetate and nitrate only), the phthalate ion, cyclic PDMS ions, perfluoroalkanoate ions, and alkoxide ions were considered. Equal concentrations of positive and negative ions were assumed, and each specific ion's relative concentration was weighted by its signal intensity in the mass spectrometer. Conducting, spherical particles were considered (with Coulomb and image potentials between particles and ions accounted for), and calculations were performed for particles in the 10 – 500 nm diameter range. Ions were modeled as point masses in calculations, and the system temperature and pressure were 300 K and 1 bar, respectively. Convergence criteria for simulations were identical to those used by Gopalakrishnan et al (2013).

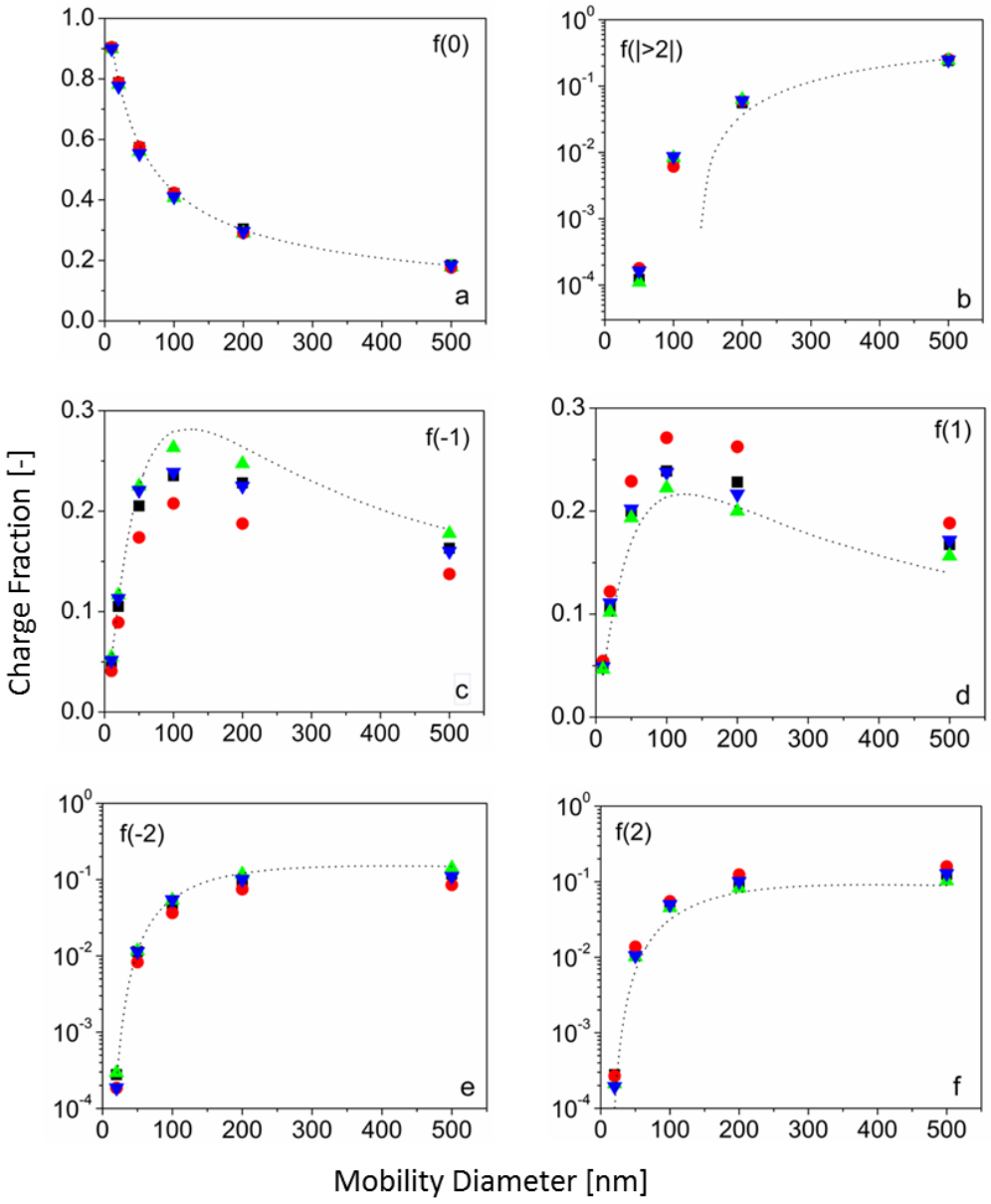

Figure 2.6. The results of Brownian dynamics simulations of the charge distribution. **(a.)** neutral particles; **(b.)** >|2| charge state particles; **(c.)** -1 charge state particles; **(d.)** +1 charge state particles; **(e.)** -2 charge state particles; **(f.)** +2 charge state particles. In all plots, the Wiedensohler (1988) regression curves are plotted. Black squares: simulations including all chemically identified ions; green triangles: simulations excluding perfluoroalkanoate ions; red circles: simulations excluding acetone and nitrate; blue triangles; simulations with number weighted mean mass and mean mobility for each polarity only considered.

With the noted conditions, calculated charge distribution results are provided in figure 2.6a-f (which are plots of the fraction of particles, *f*, with 0, -1, +1, -2, +2, and >|2|, respectively). Each data point is an average of at least 5 simulations. Charge distributions for the chemically identified ions (black squares) to distributions excluding perfluoroalkanoate ions (green triangles), distributions excluding acetone and nitrate (red circles), and distributions obtained using monodisperse ions, with the number weighted mean mass and mean mobility for each polarity are compared. Number weighted mean mass and mobilities corresponding to these input cases are summarized in Table 2.2; though the true polydisperse ion distributions measured were input into calculations, calculation of mean values including and excluding certain ion populations shows how each ion type influences overall ion properties. Finally, we plot the regression equations of Wiedensohler (1988), which are used prevalently in charge distribution calculations.

Though not shown, it is found that the inclusion of chemically unidentified ions as well as the exclusion of alkoxide ions negligibly influences charge distributions. Further, independent of input ion distribution, we find that there is little influence on the fraction of neutral particles between simulations, and that the neutral fraction calculated is in excellent agreement with the Wiedensohler (1988) regression equations. Considering all (chemically identified) ions in calculations, a more symmetric charge distribution is found than is predicted by the regression equations; this finding is in line with prior Brownian dynamics calculations with measured polydisperse ion inputs (Gopalakrishnan et al. 2015a, Gopalakrishnan et al. 2013b). Also in line with prior simulations, it is observed that the Wiedensohler distribution (1988) underestimates the fraction of

particles with more than two charges (of both polarities). As discussed previously (Gopalakrishnan and Hogan 2012b, López-Yglesias and Flagan 2013), this underestimation arises primarily because of issues in the collision rate approach of Fuchs (1963), wherein the full distribution of ion thermal velocities is not appropriately considered. However, for the singly and doubly charged ions, the difference between calculation predictions and Wiedensohler (1988) distribution are mitigated by the removal of perfluoroalkanoate ions (PTFE derived ions), and it is reiterated that these ions appear to derive from degradation of our Po-210 source housing. For this reason and in-line with Gopalakrishnan et al (2015), it is confirmed that the Wiedensohler (1988) distribution can be used to estimate the lower charge states of the bipolar charge distribution when information on ion properties is lacking, and when measurements are made in air at 300 K and near 1 bar.

Table 2.2. A summary of the mean masses and mobilities (number weighted) of ions based upon DMA-MS measurements, both considering all ions and excluding certain chemical species.

	positive		**negative**	
ion composition	**mean mass [Da]**	**mean mobility (cm^2 V^{-1} s^{-1})**	**mean mass [Da]**	**mean mobility (cm^2 V^{-1} s^{-1})**
all/mean	129.48	1.70	141.39	1.74
w/o perfluoroalkanoates	129.48	1.70	98.42	1.84
w/o alkoxides	129.48	1.70	139.69	1.79
w/o PDMS	122.35	1.71	139.69	1.79
w/o < 100 Da	130.57	1.66	197.11	1.58

Through comparison of Figure 2.6 and Table 2.2, it becomes evident that the mean masses and mobilities of the ions are correlated with the resulting charge

distribution, with lower mass and higher mobility ions for a particular polarity shifting charge distributions towards that polarity. This is most evident in simulations wherein the protonated acetone and nitrate ions have been omitted. Nitrate removal shifts the mean negative ion mobility and mass from 1.74 to 1.58 $cm^2\ V^{-1}\ s^{-1}$ and from 141.39 to 197.14 Da, respectively. Conversely, for the positively charged ions the exclusion of the protonated acetone ion has a comparably minor effect, shifting the positive ion mean mobility from 1.70 to 1.66 $cm^2\ V^{-1}\ s^{-1}$ and positive ion mean mass from 129.48 to 130.57 Da. The resulting charge distribution shows that in the absence of nitrate, the positively charged fraction exceeds the negatively charged fraction by ~35 % for singly charged particles, and up to 38% for doubly charged particles. For comparison, removal of the perfluoroalkanoate ions (and inclusion of nitrate) leads to negatively charged particles in excess of positively charged particles by ~30 % and ~15 %, for singly and doubly charged particles, respectively. Using the mean mass and mobility in calculations, in-lieu of polydisperse properties, does lead to noticeable differences in calculation results, however, the differences are small and in the range of the standard deviation of every simulated point. In total, charge distribution simulation results show that for small particles sizes and low charge states, the anticipated charge distribution does not differ appreciably from the Wiedensohler (1988) distribution. Further, in the absence of PTFE derived ions, agreement with the Wiedensohler distribution is improved. At the same time, by varying the input ion distribution, we find that ion composition can influence the particle charge distribution; in particular, it appears that the degree of bias of the charge distribution towards the negative polarity is largely dependent on the relative abundance

of highly mobile, low mass nitrate ions relative to other species. This finding may serve to better explain recent experimental studies (Jiang et al. 2014) where deviations in the charge distribution from Wiedensohler (1988) distribution were observed.

2.4 Conclusions

A DMA-MS system was used to examine the masses and mobilities of ions generated by a Po-210 source in dry air. The measurement system was composed primarily of stainless steel and Teflon tubing. Unique from prior studies, we compared measured mobilities to the predicted mobilities of gas molecule scattering calculations (using the IMoS program). Based on this study, the following conclusions can be drawn:

1. In large part, the ions detected appear to derive from system components (or compounds used in the manufacture of system components) and specifically from compounds with parts per trillion to parts per billion vapor phase concentrations. While the particular ions detected were specific to our measurement system, phthalate ions, acetone, nitrate, PDMS, and alkoxide ions are likely to be found in other systems and given the prevalent use of PTFE in measurement systems, perfluoroalkanoate ions may also be generated.
2. Direct calculation of ion mobilities from structural models shows good agreement with measurements when a diffuse scattering model is applied. The exception to this conclusion is found for highly planar ions, i.e. cyclic PDMS and phthalate. We believe application of this calculation approach in

analyzing IMS-MS measurements in aerosols, as well as in DMA measurements of sub 2.0 nm particles, will enable researchers to extract more information from mobility measurements beyond a mobility equivalent size, as is frequently reported.

3. Brownian dynamics calculations show that in the absence of PTFE derived perfluoroalkanoate ions, Wiedensohler (1988) distribution predictions of the neutral, -1, +1, -2, and +2 fractions describe well the anticipated charge distribution for the measured ions. At the same time, calculations show that ion composition can directly influence the charge distribution. It is noted that prior studies along these lines (Steiner et al, 2014), have only examined ion composition effects on collision rate, which is more sensitive to ion composition than the steady-state charge distribution (i.e. the steady-state charge distribution depends on the relative masses and mobilities of one polarity to the other). Calculations suggest that the bias observed in charge distributions is primarily dependent upon the concentration of nitrate ion in the gas phase. Nitric acid has an anomalously high gas phase acidity for its mass, and can persist in the gas phase in higher concentrations than other low mass (<100 Da) species.
4. Future work in bipolar charging should focus on assessing the influences of water vapor on ion properties, in particular for the nitrate ion. Additionally, the possibility of "doping" bipolar ion sources with control chemical composition vapor phase species should be explored. This may enable better

control over ion properties, which in turn would remove ambiguities in charging calculations.

Chapter 3: Ion Mobility Spectrometry-Mass Spectrometry Examination of the Structures, Stabilities, and Extents of Hydration of Dimethylamine-Sulfuric Acid Clusters

Abstract: This chapter deals with the application of an atmospheric pressure differential mobility analyzer (DMA) coupled to a time-of-flight mass spectrometer to examine the stability, mass-mobility relationship, and extent of hydration of dimethylamine-sulfuric acid cluster ions, which are of relevance to nucleation in ambient air. Cluster ions were generated by electrospray ionization and were of the form: $[H((CH_3)_2NH)_x(H_2SO_4)_y]^+$ and $[(HSO_4)((CH_3)_2NH)_x(H_2SO_4)_y]^-$, where $4 \leq x \leq 8$, and $5 \leq y \leq 12$. By analyzing cluster ion mobility at atmospheric pressure upstream of the mass spectrometer, under dry conditions, we find that positively charged cluster ions dissociated via loss of both multiple dimethylamine and sulfuric acid molecules after mobility analysis but prior to mass analysis, and few parent ions were detected in the mass spectrometer. Dissociation also occurred for negative ions, but to a lesser extent than for positive ions for the same mass spectrometer inlet conditions. Under humidified conditions (relative humidities up to 30% in the DMA), positively charged cluster ion dissociation in the mass spectrometer inlet was mitigated and occurred primarily by H_2SO_4 loss from ions containing excess acid molecules. DMA measurements were used to infer collision cross sections (CCSs) for all identifiable cluster ions. Stokes-Millikan equation and diffuse/inelastic gas molecule scattering predicted CCSs overestimate measured CCSs by more than

15%, while elastic-specular collision model predictions are in good agreement with measurements. Finally, cluster ion hydration was examined by monitoring changes in CCSs with increasing relative humidity. All examined cluster ions showed a modest amount of water molecule adsorption, with percentage increases in CCS smaller than 10%. The extent of hydration correlates directly with cluster ion acidity for positive ions.

3.1 Introduction

New particle formation events occur in the ambient atmosphere when condensed phase particles form from trace vapor phase precursors. There is a growing body of evidence from both field and laboratory measurements that sulfuric acid and amine vapors prominently serve as the precursors in ambient new particle formation events, and that the first steps of nucleation often involve the formation of amine-sulfuric acid clusters.(Kurten et al. 2014, Qiu and Zhang 2013, Zhao et al. 2011, Smith et al. 2010b, Chen et al. 2012, Makela et al. 2001) The structures, stabilities, and reactivities of such clusters are hence of interest, and have been examined in a number of recent computational(Loukonen et al. 2010, Tsona et al. 2015, DePalma et al. 2012, DePalma, Doren and Johnston 2014, Kurten et al. 2008, Nadykto et al. 2014, Nadykto et al. 2011, Ortega 2014) and experimental(Bzdek, Ridge and Johnston 2011, Jen, McMurry and Hanson 2014b, Johnson and Johnson 2013, Bzdek et al. 2013) studies. Nonetheless, many of the properties of amine-sulfuric acid clusters which strongly influence the interpretation of field and laboratory measurements remain uninvestigated. Smaller

clusters (typically containing fewer than ten sulfuric acid molecules) are frequently detected via chemical ionization-mass spectrometry,(Zhao et al. 2010, Almeida et al. 2013b, Kulmala et al. 2013, Kurten et al. 2014, Bianchi et al. 2014) and in many instances, the highest signal intensity clusters detected are composed of amine-sulfuric acid molecules in a near 1:1 ratio (i.e. the clusters are predominately aminium bisulfate clusters). However, because clusters must undergo high energy collisions with gas molecules in the inlets of mass spectrometers (i.e. to efficiently transmit clusters from high pressure to low pressure), excess acid or excess base molecules may dissociate(Bzdek et al. 2013) prior to mass analysis; this possibility has not been fully examined in prior studies. Aside from chemical ionization-mass spectrometry, electrical/ion mobility analysis (referred to simply as mobility analysis in this work) coupled with condensation based detection is commonly employed for the measurement of larger clusters (nanoparticles).(Yu, McGraw and Lee 2012, Jiang et al. 2011d) The masses of such clusters are typically inferred via assumed relationships(Jiang et al. 2011d, Larriba et al. 2011) between mobility and mass or from computations;(Tsona et al. 2015) neither of these approaches have been experimentally verified for these clusters, and in fact they have recently been shown not to apply to all species in the 1 nm size range.(Ouyang et al. 2013a, Maisser et al. 2015) Additionally, an important question is the extent of water vapor uptake by dimethylamine-sulfuric acid clusters under atmospherically relevant conditions, i.e. whether such clusters can be considered dry species, or are better modeled as nanodroplets. Though computational studies have been performed on 1:1 ratio clusters(Tsona et al. 2015, DePalma et al. 2014) (suggesting there

is little water uptake) and water uptake measurements have been made on 3-10 nm particles(Ouyang et al. 2015) as well as larger particles(Qiu and Zhang 2012, Lavi et al. 2013) (suggesting particles are partially hydrated under atmospherically relevant conditions), the hydration of smaller clusters has not been examined experimentally.

This study focuses on the stabilities of dimethylamine ($(CH_3)_2NH$)- sulfuric acid (H_2SO_4) clusters in a mass spectrometer inlet region, the link between cluster mobilities in air and their structures/masses, and the extent of cluster hydration under atmospherically relevant conditions. Each of these cluster properties is examined via ion mobility spectrometry-mass spectrometry (IMS-MS) with a differential mobility analyzer coupled to a mass spectrometer (DMA-MS).(Rus et al. 2010a) Here, the focus is specifically on dimethylamine because a recent study suggests that dimethylamine-sulfuric acid clusters are particularly stable under ambient conditions.(Jen et al. 2014b) In the DMA-MS system, unique from other forms of IMS-MS (notably drift tube IMS-MS), the mobility measurement is made at atmospheric pressure, near room temperature, and with an easily controllable gas composition.(Oberreit et al. 2015) Mobility measurements are therefore made for clusters which are equilibrated with their surroundings and prior to cluster passage through any high pressure drop, high electrical field strength interface (where they may dissociate).(Hogan and Fernandez de la Mora 2010) In the subsequent sections, measurements are described in detail. Measurements follow a parallel-structure to prior DMA-MS measurements of the structures and extents of water vapor uptake of salt cluster ions.(Oberreit et al. 2015) The discussion section describes the identification of cluster ion dissociation events in the mass spectrometer

inlet region, and the comparison of measured electrical mobilities (at low relative humidity) to gas molecule scattering calculations(Larriba and Hogan 2013b, Larriba and Hogan 2013a, Larriba-Andaluz and Hogan 2014) for chemically identified cluster ions of the form $[H((CH_3)_2NH)_x(H_2SO_4)_y]^+$ and $[(HSO_4)((CH_3)_2NH)_x(H_2SO_4)_y]^-$, where $4 \leq x \leq 8$, and $5 \leq y \leq 12$, and the extent of hydration of cluster ions near 304 K, atmospheric pressure, and relative humidities (*RH*) in the 3% to 30% range. The results presented in this chapter provide greater insight into the properties of clusters commonly formed in ambient new particle formation events and provide guidance in interpreting ambient field and laboratory measurements of cluster formation.

3.2 Experimental Methods

3.2.1 Cluster Ion Generation

Similar to Ouyang et al,(Ouyang et al. 2015) cluster ions were generated by electrospray ionization, using a solution of 1 mM dimethylamine (40% in water, Sigma-Aldrich) and 2 mM sulfuric acid (~ 98 %, Sigma-Aldrich) in a solvent of 95% methanol (HPLC grade, Fisher Scientific) and 5 % deionized water. The solution was driven from a 1.5 mL polypropylene vial through a 40 μm inner diameter, 360 μm outer diameter silica capillary (Polymicro Technologies, Phoenix, AZ) by applying gauge pressures of 250 -300 mbar across the capillary. Electrospray operation was facilitated by applying a potential difference between the solution (using a silver electrode placed within the polypropylene vial) and the upper electrode of the DMA. The capillary outlet was tapered, and a stable Taylor cone(Cloupeau and Prunet-Foch 1989) during electrospray

operation was visually confirmed with a camera and by monitoring ion currents, which were steady in the 200 to 250 +/- 5 nA range and 200 to 400 +/- 10 nA range for positive and negative modes of electrospray, respectively. Electrospray ionization of solutions with solute concentrations in the millimolar range typically yields both singly charged cluster ions and larger multiply charged cluster ions.(Gamero-Castano and Fernandez de la Mora 2000c, Gamero-Castano and Fernandez de la Mora 2000b) Singly and multiply charged cluster ions were also observed in this study, and IMS-MS can be applied to analyze sizes and structures of both cluster types.(Fernandez de la Mora, Thomson and Gamero-Castano 2005, Fernández-García and Fernández de la Mora 2014) This chapter focuses only on the singly charged clusters, with a particular emphasis on those in the 700-1600 Da mass range.

3.2.2 Ion Mobility Spectrometry - Mass Spectrometry

IMS-MS measurements of cluster ions were made with a parallel plate DMA (model P5, SEADM, Boecillo, Spain) coupled to a time-of-flight mass spectrometer (QSTAR XL, AB Sciex, Concord, ON, Canada). The DMA-MS system was operated as described in detail in prior studies(Rus et al. 2010a, Oberreit et al. 2015) with a recirculating sheath flow. In this system, ions are sampled electrostatically into the DMA by holding the electrospray source at a voltage 2-3 kV above (or below, for negative ions) the upper electrode of the DMA, while the inlet operates with a counterflow of ~50 cm^3 min^{-1}. The supply gas for the recirculating sheath flow, the counterflow, and the flow transporting ions from the DMA outlet (~500 cm^3 min^{-1}) into the mass spectrometer is

supplied from a separate port near the recirculating blower; this allows the composition of the supply gas to be controlled independently of the gas composition in which the cluster ions are generated. The sheath flow gas was ultrahigh purity air (Matheson, St.Paul, Minnesota) and was humidified using a heated nebulizer similar to that employed by Oberreit et al.(Oberreit et al. 2015, Oberreit, McMurry and Hogan 2014) The temperature of the sheath gas was measured to be 304-305 K with a Type-K thermocouple (Omega) during measurements. The relative humidity of the sheath flow was determined before and after DMA-MS measurements using a dew point hygrometer (General Eastern); the relative humidity was confirmed to be within 1 % of the value expected based upon nebulizer settings. Between measurements, the DMA-MS system was not used to examine any other samples (to avoid the possibility of contamination). The mass spectrometer remained under vacuum, with ultrahigh purity N_2 flowing into the DMA and MS when measurements were not being made.

For the results presented, the potential difference across DMA electrodes, which determines the mobilities of ions which can be transmitted to the lower electrode (and into the mass spectrometer),(Fernandez de la Mora et al. 1998) was varied in 10 V increments in the 500 to 4000 V range for positive ions and -600 to -5000 V for negative ions. For each applied DMA potential difference, time-of-flight mass spectra were collected using accumulation times of 2-3s in the 50 to 8000 Th range. Between the DMA and time-of-flight tube, ions were transmitted through an orifice plate, lens, and skimmer, followed by three quadrupole sections. Collectively, these form the mass spectrometer inlet region, in which the pressure drops from atmospheric pressure down to

10^{-7} Torr and ions are not in equilibrium with their surroundings. The quadrupoles were operated in RF only mode, with the "enhance all" option in the QSTAR XL software (Analyst 2.0) selected in an effort to transmit without any mass bias. The orifice plate, lens, and skimmer were all held at fixed DC potentials; here we kept the differences in potential to a minimum in an effort to prevent cluster dissociation, as prior DMA-MS studies reveal that complete cluster dissociation can occur with large potential differences in mass spectrometer inlets (even for extremely low volatility species).(Hogan and Fernandez de la Mora 2009, Hogan and Fernandez de la Mora 2010, Ouyang et al. 2013a) Specifically, the orifice plate and lens were held at the same potential, a 110 V difference was applied between the lens and skimmer (lower values led to substantially reduced ion transmission), and there was no constant potential difference between the skimmer and first quadrupole. Though different atmospheric pressure ion source mass spectrometer systems have distinct inlet configurations, the majority utilize lens-skimmer based systems to optimize ion transmission from atmospheric pressure to vacuum, where there is the potential for cluster ion dissociation.(Bzdek et al. 2013, Bzdek et al. 2011) Therefore, while examined extent of dissociation (described in the subsequent section) is specific to the mass spectrometer and settings employed, our conclusions are generally applicable to mass spectrometric analysis of cluster ions sampled at atmospheric pressure.

The resolving power of the DMA was in excess of 50 for measurements and applied voltages were known to within 1%, hence small changes in mobility were detectable. DMA calibration was performed in an identical fashion to prior studies through measurement of the potential difference required to transmit the

tetradodecylammonium$^+$ ion ($[CH_3(CH_2)_{11}]_4N^+$); this ion was generated via electrospray ionization of a 3 mM methanol solution of tetradodecylaminium bromide (Sigma-Aldrich). Its mobility was reported by Ude & Fernandez de la Mora(Ude and Fernandez de la Mora 2005) in air at 298 K, and was chosen for calibration because it was observed to have a mobility independent of the relative humidity of the sheath air in prior work.(Oberreit et al. 2015) For calibration, the $[CH_3(CH_2)_{11}]_4N^+$ mobility was adjusted by a factor of $(T/ 298\ K)^{1/2}$, where T is the measurement temperature. This approximately corrects for the temperature difference in the measurements made here. Little variation in the voltage (<1%) required to transmit $[CH_3(CH_2)_{11}]_4N^+$ across the DMA was observed throughout the course of this study. Nonetheless, to assess the influence of water vapor on ion mobilities, low water vapor content DMA-MS spectra were measured daily for all ions, and calibration was performed at each relative humidity.

3.3 Results and Discussion

3.3.1 Cluster Identification and Dissociation

The main advantage of electrospray ionization is that a variety of clusters can be generated with ample concentration for detection and identification via mass spectrometry.(Fernández-García and Fernández de la Mora 2014) However, the cluster formation process (either ion evaporation or the charge residue mechanism)(Gamero-Castano and Fernandez de la Mora 2000b, Higashi et al. 2015) in electrospray ionization differs considerably from nucleation processes, hence the presented relative abundances

of different cluster ions cannot be extrapolated to draw conclusions regarding their prominence during new particle formation events. Even so, measurements of electrospray generated clusters can be used to describe the physicochemical properties of chemically identified clusters which are not dependent on the cluster formation mechanism. It must be determined, however, if electrospray ionization can be used to produce clusters similar in chemical composition to those observed in acid-base nucleation chamber experiments.(Bianchi et al. 2014) Mass spectra for positive and negative cluster ions under dry conditions (i.e. without water vapor introduced into the sheath flow) and under moderately humidified conditions (RH = 16% and RH = 30%) are shown in Figure 3.1. Focusing first on the positive clusters, we find that the most abundant ions are of the form: $[H((CH_3)_2NH)_x(H_2SO_4)_{x-1}]^+$, i.e. most cluster ions contain dimethylamine and sulfuric acid in a 1:1 ratio with an additional dimethylammonium$^+$ cation. These ions are labeled as type "A" in the positive cluster ion spectra. At increased relative humidity, the relative signal intensity for higher mass clusters decreases. Possible reasons for this include (1) a change in the electrospray ionization process brought about by water vapor sorption to droplets (adjusting ion evaporation kinetics(Hogan and Fernandez de la Mora 2009) as well as the droplet Rayleigh limit) and (2) additional condensation of water onto ions after the DMA, as has been observed for ions undergoing free jet expansion in the presence of water vapor.(Bush, Saykally and Williams 2006, Fenn 2000, Searcy and Fenn 1974) The latter would presumably occur more frequently for larger mass ions, as classical theories suggest that heterogeneous condensation is more likely to occur on lower curvature surfaces (larger sized

species).(Thomson 1871) However, I elect not to investigate such changes here, as again the relative abundances of ions cannot be related to their abundances in new particle formation events.

Nonetheless, noteworthy is that positive mass spectra are qualitatively similar to those obtained in chamber experiments(Bianchi et al. 2014) (the ions themselves are identical in composition), wherein dimethylamine-sulfuric acid clusters are produced from dimethylamine, sulfuric dioxide, and ozone at RH= 38%, as well as to those obtained by Bzdek et al(Bzdek et al. 2011) utilizing a completely distinct mass spectrometer system and a different electrospray source. The negative ion spectra are found to be more complex, with ions of the form $[(HSO_4)(H_2SO_4)_x]^-$ (x = 0-2), $[(HSO_4)((CH_3)_2NH)_{y-2}(H_2SO_4)_y]^-$, and $[(HSO_4)((CH_3)_2NH)_{y-1}(H_2SO_4)_y]^-$ detected under both dry and humidified conditions. These clusters are labelled in spectra as types "I", "II", and "III", respectively. The negatively charged clusters are found to be similar in composition those detected in chamber experiments. Similar to the findings of Bzdek et al,(Bzdek et al. 2011) it can therefore be confirmed that although the electrospray process is distinct from vapor phase nucleation in the mechanism of cluster formation, cluster ions of the same chemical composition to those detected in chamber experiments can be produced via electrospray ionization of dimethylamine and sulfuric acid solutions.

In examining cluster ion mobilities, we elect to focus on the types "A", "II", and "III" ions. In the negative cluster spectra, type "I" ions are found to be dissociation products of multiply charged clusters in the negative mode, precluding clear identification of their mobilities (i.e. they appear at a broad range of mobilities(Hogan

and Fernandez de la Mora 2009)). For selected type “A” ions, inverse mobility spectra measured in the absence of water vapor (dry conditions) are shown in Figure 3.2a. Such results are obtained by isolating the detector signal at about a narrow (+/- 0.5 Th) mass range at a specific mass. The exact chemical composition and charge state of each ion is directly inferred from the exact mass as well as mass difference between isotopes (i.e. singly charged ions have isotopics differ by nominally 1 Th, doubly charged by nominally ½ Th, etc.).(Gross 2004) Further, in DMA-MS measurements, cluster ions of specific charge states group into specific bands;(Hogan and Fernandez de la Mora 2009) such bands are shown in the contour plots provided by Ouyang et al(Ouyang et al. 2015) for dimethylamine-sulfuric acid cluster ions. Results are plotted in terms of inverse mobility, as mobility is inversely proportional to collision cross section, a measurement of effective cluster size.(Mason and McDaniel 1988) Similar to prior studies of ionic liquid(Fernández-García and Fernández de la Mora 2014, Hogan and Fernandez de la Mora 2009) and iodide salt(Ouyang et al. 2013a) cluster ions, multiple peaks in inverse mobility spectra for each cluster ion are present. In many instances, cluster ions differing in composition by a single dimethylamine-sulfuric acid pair have peaks in inverse mobility which coincide with one another. This is indicative of cluster ion dissociation between the DMA and time-of-flight region of the mass spectrometer (i.e. in the inlet region), leading to peaks located at the inverse mobility of the parent cluster ion, but at the mass-to-charge ratio of the ion remaining after neutral loss. Such collision-induced dissociation appears to occur under dry conditions primarily via loss of cation-anion pairs for cluster ions:

$[H((CH_3)_2NH)_x(H_2SO_4)_{x-1}]^+ \rightarrow [H((CH_3)_2NH)_{x-m}(H_2SO_4)_{x-1-m}]^+ + [((CH_3)_2NH)_m(H_2SO_4)_m]$

In previous studies of cluster ions,(Hogan and Fernandez de la Mora 2010, Ouyang et al. 2013a) it has been possible to determine the true mobilities of many ions accounting for dissociation after mobility measurement and before mass analysis. However, for the dry inverse mobility spectra obtained here, dissociation was too substantial for unambiguous parent ion identification, even with mass spectrometer inlet settings adjusted to minimize collision-induced dissociation.

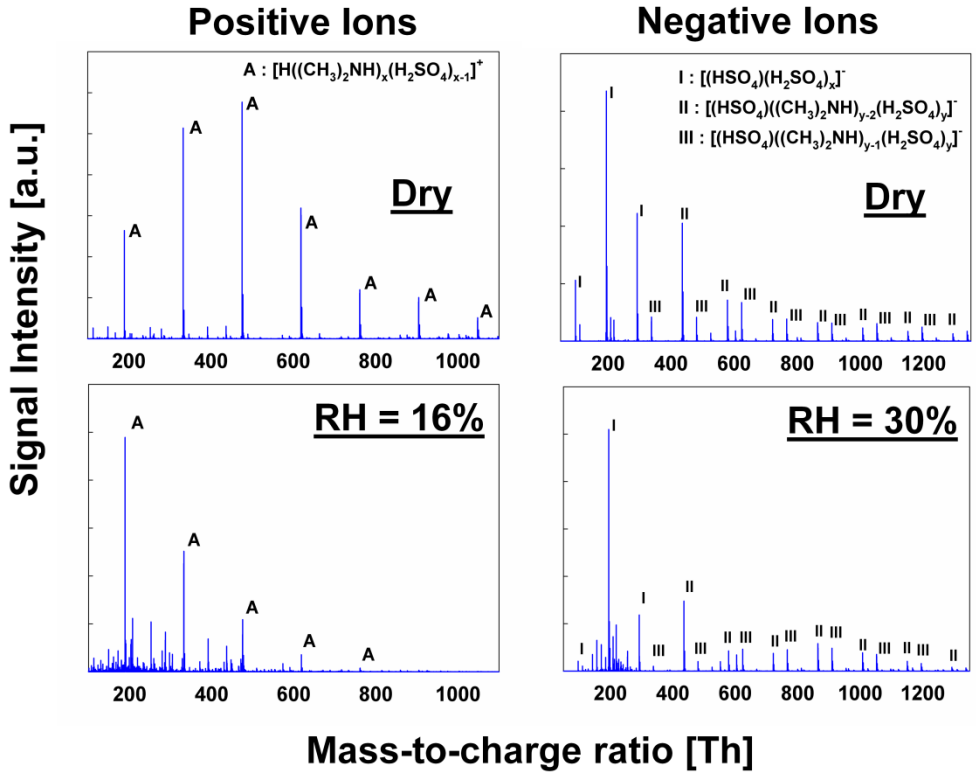

Figure 3.1. Integrated mass spectra for electrospray generated, positive and negative dimethylamine-sulfuric acid cluster ions. Prominent peaks in spectra are labeled. Type A: $[H((CH_3)_2NH)_x(H_2SO_4)_{x-1}]^+$; Type I: $[(HSO_4)(H_2SO_4)_x]^-$; Type II: $[(HSO_4)((CH_3)_2NH)_{y-2}(H_2SO_4)_y]^-$; Type III: $[(HSO_4)((CH_3)_2NH)_{y-1}(H_2SO_4)_y]^-$.

In contrast, in Figure 3.2b, at RH = 19%, inverse mobility spectra for the same type "A" ions are plotted, and do not reveal the same dissociation pattern (for the same mass spectrometer inlet orifice plate-lens-skimmer settings as the dry conditions); although multiple peaks are present for these ions, peak positions do not precisely align for ions differing in mass by a cation-anion pair (this is made clear via comparison of the vertical lines provided in Figures 3.2a & 3.2b). Instead, under humidified conditions (RH ≥ 3.5%), most peaks in inverse mobility spectra are found to arise from the dissociation of clusters containing excess sulfuric acid molecules only, i.e. the electrospray ionization process produces clusters with excess acid which are transmitted through the DMA, but reactions of the following form take place in the inlet region:

$$[H((CH_3)_2NH)_x(H_2SO_4)_{x+m}]^+ \rightarrow [H((CH_3)_2NH)_x(H_2SO_4)_{x+m-n}]^+ + [(H_2SO_4)]_n)$$

This is evidenced in Figure 3.3, which displays the inverse mobility spectra for cluster ions of the form $[H((CH_3)_2NH)_6(H_2SO_4)_y]^+$ with y = 5-8. The dissociation patterns under humidified conditions are significantly simpler to interpret than those observed under dry conditions (there are fewer peaks attributable to dissociation), and parent ion identification is possible in a number of instances. For example, in Figure 3.3, the peak labeled at "a" corresponds to the inverse mobility of the ion $[H((CH_3)_2NH)_6(H_2SO_4)_5]^+$, while "b" and "c" correspond to $[H((CH_3)_2NH)_6(H_2SO_4)_6]^+$ and $[H((CH_3)_2NH)_6(H_2SO_4)_7]^+$, respectively. In total, under humidified conditions, for positive ions we are able to identify the mobilities of 18 ions of the form $[H((CH_3)_2NH)_x(H_2SO_4)_y]^+$ with x = 6-8 and y = 5- 12 and are able to monitor shifts in the

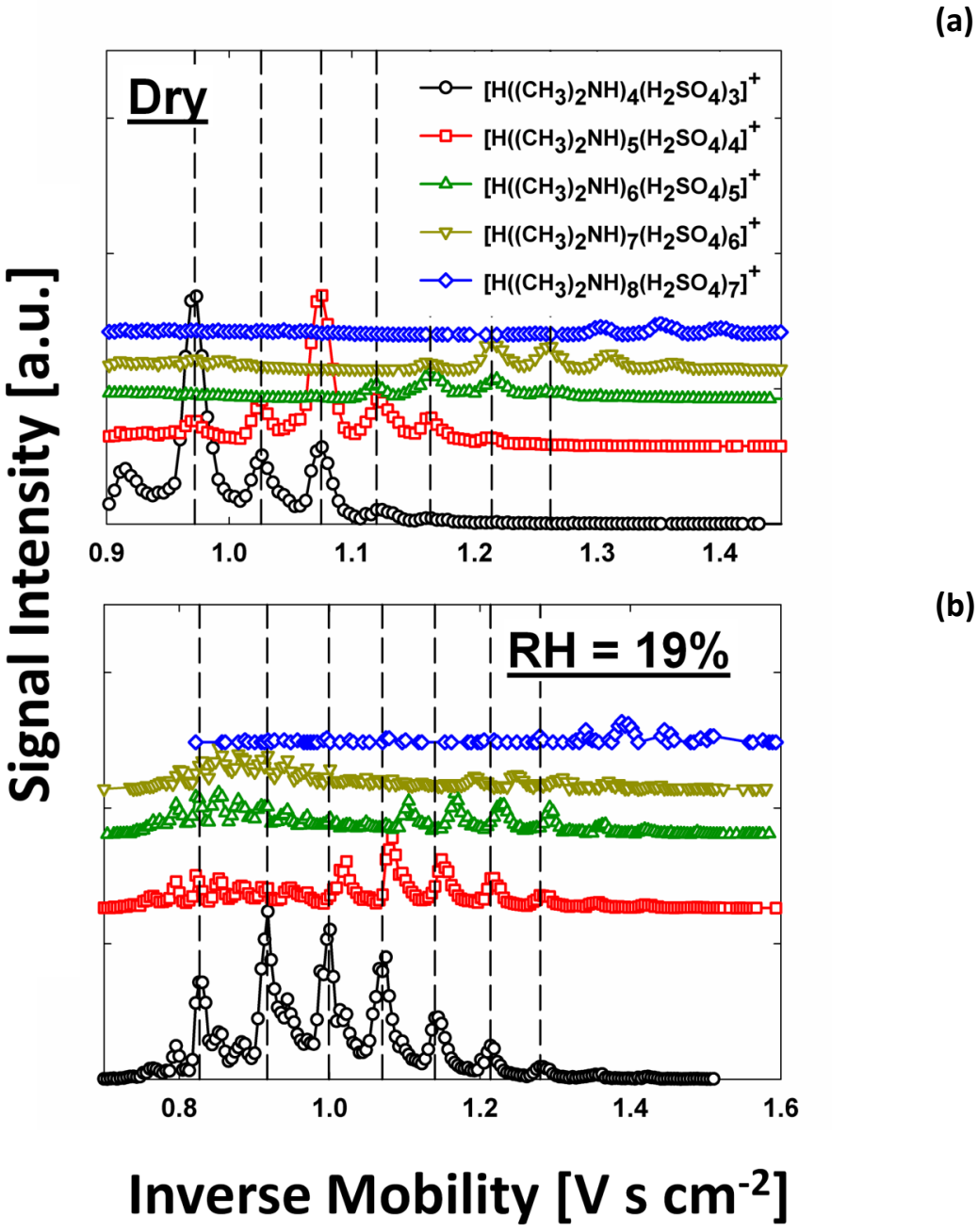

Figure 3.2. Inverse mobility spectra for mass-selected, chemically identified, positive, singly charged, type A ions with $x = 4$-8, under **(a.)** dry conditions and **(b.)** a relative humidity of 19%. Vertical guidelines are provided at peak locations for the lowest selected mass, showing that dissociation of gives rise to these peaks under dry conditions, but not under humidified conditions.

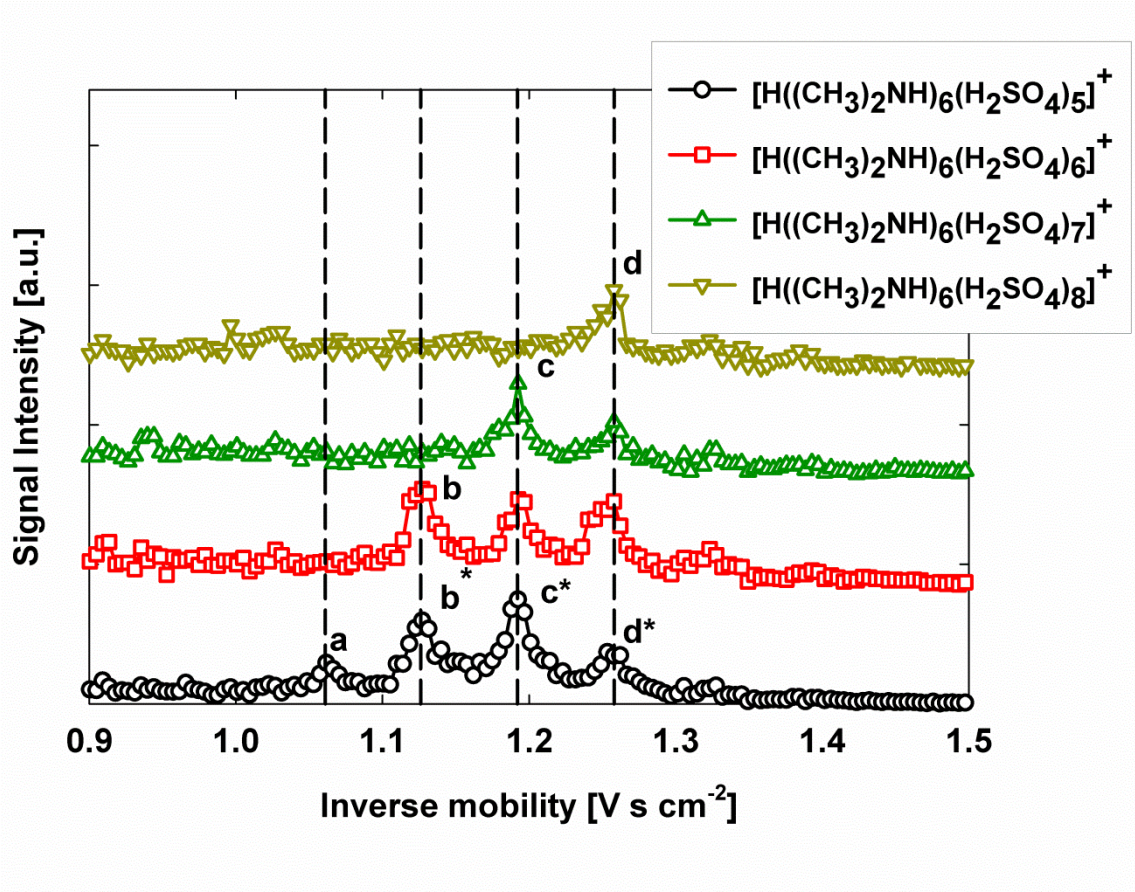

Figure 3.3. Inverse mobility spectra for positive, singly charged, ions of the form $[H((CH)_3)_2NH)_6(H_2SO_4)_x]^+$ with x = 5-8, at relative humidity of 19%. Vertical guidelines are provided to demonstrate that multiple peaks arise due to the dissociation of sulfuric acid from clusters after mobility measurement but before mass analysis.

mobilities due to water vapor uptake beginning at RH = 3.5%. The baseline mobilities of these ions at RH = 3.5% are provided in Table 3.1. The stark differences observed in the inverse mobility spectra of mass identified ions measured under dry and modestly humidified conditions allow us to make several inferences about the properties of positively charged clusters. Identical electrosprays were employed for dry and

Table 3.1. List of the cluster ions studied with mobilities and mobility equivalent diameters at the lowest relative humidity where the ions were discernable. a: corrected for gas molecule diameter. b: corrected for the ion-induced dipole potential and gas molecular diameter. c: 'dry' refers to conditions where the DMA sheath flow gas was not doped with water vapor.

Species	Relative Humidity, %	Mobility, $cm^2V^{-1}s^{-1}$	Mobility diameter [a], Nm	Mobility diameter[b], nm	Collision cross Section, $Å^2$
$[H((CH_3)_2NH)_6(H_2SO_4)_5]^+$	3.5	0.966	1.17	1.12	231
$[H((CH_3)_2NH)_6(H_2SO_4)_6]^+$	3.5	0.920	1.21	1.16	244
$[H((CH_3)_2NH)_6(H_2SO_4)_7]^+$	3.5	0.880	1.24	1.20	253
$[H((CH_3)_2NH)_6(H_2SO_4)_8]^+$	3.5	0.844	1.27	1.23	263
$[H((CH_3)_2NH)_6(H_2SO_4)_9]^+$	3.5	0.804	1.31	1.27	277
$[H((CH_3)_2NH)_6(H_2SO_4)_{10}]^+$	3.5	0.771	1.34	1.31	287
$[H((CH_3)_2NH)_7(H_2SO_4)_6]^+$	3.5	0.887	1.24	1.19	253
$[H((CH_3)_2NH)_7(H_2SO_4)_7]^+$	3.5	0.851	1.27	1.23	263
$[H((CH_3)_2NH)_7(H_2SO_4)_8]^+$	3.5	0.817	1.30	1.26	273
$[H((CH_3)_2NH)_7(H_2SO_4)_9]^+$	3.5	0.786	1.33	1.29	284
$[H((CH_3)_2NH)_7(H_2SO_4)_{10}]^+$	3.5	0.753	1.36	1.33	294
$[H((CH_3)_2NH)_7(H_2SO_4)_{11}]^+$	3.5	0.725	1.39	1.36	305
$[H((CH_3)_2NH)_8(H_2SO_4)_7]^+$	3.5	0.822	1.29	1.25	270
$[H((CH_3)_2NH)_8(H_2SO_4)_8]^+$	3.5	0.795	1.32	1.28	280
$[H((CH_3)_2NH)_8(H_2SO_4)_9]^+$	3.5	0.764	1.35	1.32	291
$[H((CH_3)_2NH)_8(H_2SO_4)_{10}]^+$	3.5	0.737	1.38	1.35	301
$[H((CH_3)_2NH)_8(H_2SO_4)_{11}]^+$	3.5	0.712	1.41	1.38	312
$[(HSO_4)((CH_3)_2NH)_4(H_2SO_4)_6]^-$	dry [c]	0.942	1.19	1.14	237
$[(HSO_4)((CH_3)_2NH)_5(H_2SO_4)_6]^-$	dry	0.908	1.22	1.17	247
$[(HSO_4)((CH_3)_2NH)_5(H_2SO_4)_7]^-$	dry	0.865	1.25	1.21	257
$[(HSO_4)((CH_3)_2NH)_6(H_2SO_4)_7]^-$	dry	0.835	1.28	1.24	267
$[(HSO_4)((CH_3)_2NH)_6(H_2SO_4)_8]^-$	dry	0.812	1.30	1.27	273
$[(HSO_4)((CH_3)_2NH)_7(H_2SO_4)_8]^-$	dry	0.781	1.33	1.30	284
$[(HSO_4)((CH_3)_2NH)_7(H_2SO_4)_9]^-$	dry	0.758	1.36	1.32	294
$[(HSO_4)((CH_3)_2NH)_8(H_2SO_4)_9]^-$	dry	0.729	1.39	1.36	305

humidified experiments, hence under both conditions cluster ions with excess sulfuric acid molecules were produced. Other than the addition of water vapor, both the DMA and MS were operated identically for dry and humidified cluster measurements. Under dry conditions, it appears that positively charged clusters are too unstable to be transmitted into the DMA, i.e. they dissociate to form $[H((CH_3)_2NH)_x(H_2SO_4)_{x-1}]^+$ clusters on a rapid (unobservable) timescale, and these clusters further dissociate at the DMA outlet/mass spectrometer inlet via the loss of multiple dimethylamine-sulfuric acid pairs. Interestingly, dissociation within DMA does not appear to occur. As discussed in previous work,(Hogan and Fernandez de la Mora 2009) cluster ion dissociation during transit through the DMA leads to broad streaks in mass-selected inverse mobility spectra, which are bounded by the inverse mobilities of the parent and dissociation product ions. Such streaks are not observed for the singly charged ions examined here. In contrast to dry conditions, under humidified conditions, excess sulfuric acid clusters are not only stable enough for DMA measurement and at the DMA outlet/mass spectrometer inlet, but also they dissociate primarily through loss of sulfuric acid only. Without mobility measurement prior to mass analysis, the excess sulfuric acid clusters, which were in similar signal intensity to the $[H((CH_3)_2NH)_x(H_2SO_4)_{x-1}]^+$ clusters under humidified conditions (evidenced by the similar sizes of the peaks "a", "b*", "c*", and "d*" in Figure 3.3), would be thought to be present in lower concentration or may go undetected. This suggests that mass spectrometry alone may not enable adequate detection of clusters with excess acid molecules, unless inlet conditions (electric field intensities and extent of pressure drop per unit distance) can be tuned to minimize collision-induced dissociation

more so than was possible here. Further, the detection of excess acid cluster ions only under humidified conditions suggests that water is bound to such clusters within the DMA, and that water serves to enhance acidic cluster stability. The extent of water uptake by cluster ions is examined subsequently, in the "*Extent of Hydration*" subsection.

Figure 3.4 contains plots of the inverse mobility spectra for selected, negatively charged type "II" and type "III" ions. Unlike the positively charged clusters, negatively charged cluster ion inverse mobility spectra contain simpler dissociation patterns, and distinct behavior is not observed between dry and humidified conditions (cf. Figure 3.4a and Figure 3.4b). Though dissociation is found to occur via loss of dimethylamine, sulfuric acid, and dimethylamine-sulfuric acid pairs, we are able to identify the mobilities of 8 parent ions of the form $[(HSO_4)((CH_3)_2NH)_x(H_2SO_4)_y]^-$, with x = 4-8 and y = 6-9. The mobilities of these ions are also noted in table 1 for dry conditions.

3.3.2 Comparison between Measured and Predicted Mobilities

Atmospheric pressure mobility separation coupled with mass spectrometry enables identification of dissociation events in mass spectrometer inlets and examination of how cluster ion mobility relates to cluster structure/mass. In the free molecular regime, the mobility, *K*, is linked to the collision cross section (CCS) of the ion via the Mason-Schamp equation:(Mason and McDaniel 1988)

$$K = \left(\frac{3ze}{4\rho_{gas}}\right)\sqrt{\frac{\pi\mu_r}{8kT}}\frac{1}{\Omega} \tag{3.1}$$

where z is the cluster ion charge state, e is the unit electron charge, μ_r is the reduced mass of the cluster ion-gas molecule pair, k is Boltzmann's constant, T is the system temperature, and Ω is the CCS. Expanded upon in a number of prior studies,(Larriba and

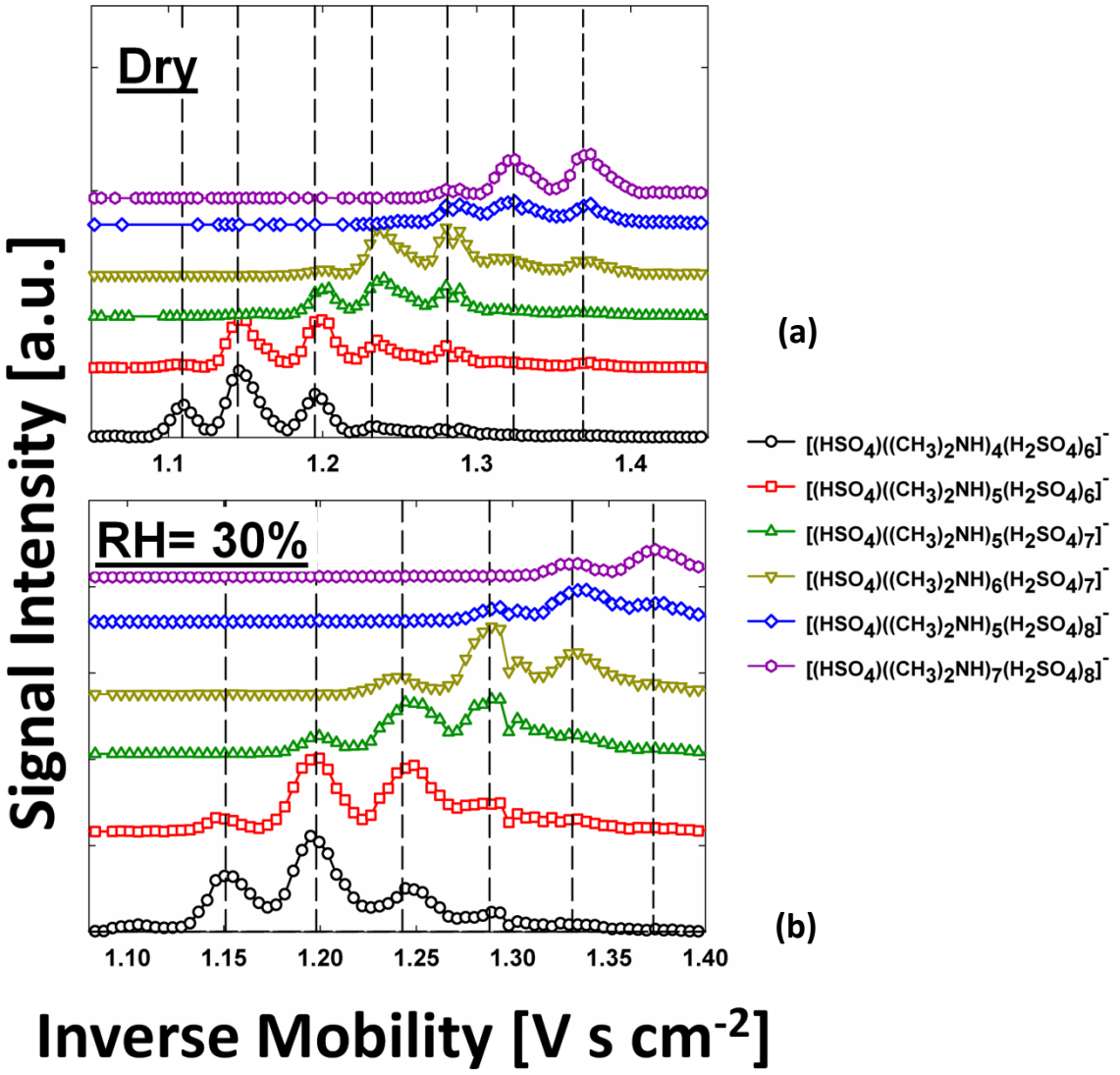

Figure 3.4. Inverse mobility spectra of selected type "II" and type "III" negative cluster ions, under (a.) dry conditions and (b.) RH = 30%.

Hogan 2013b, Larriba and Hogan 2013a, Larriba-Andaluz and Hogan 2014, Larriba-Andaluz et al. 2015a, Mesleh et al. 1996, Shvartsburg and Jarrold 1996, Shvartsburg, Mashkevich and Siu 2000) the CCS is a complex parameter which is a function of the structure of the cluster ion, the structure of the gas molecule, the potential interactions between gas molecules and the cluster ion, and the manner in which gas molecules impinge and are reemitted from cluster ions (i.e. the extent of exchange between different modes of kinetic energy upon collision). In most studies of new particle formation events, the CCS is most commonly related to an analyte's mobility equivalent diameter (d_m) via the free molecular limit of the Stokes-Millikan equation:(Tammet 1995)

$$\Omega = 1.36\frac{\pi}{4}\left(d_m + d_g\right)^2 \tag{3.2a}$$

in which d_g is the effective gas molecule diameter (3 Å in air)(Ku and Fernandez de la Mora 2009) and the factor 1.36 results from Davies interpretation of Millikan's oil drop measurements.(Davies 1945) More recently, it has been pointed out that even for spherical species, equation (3.2a) would not apply if the ion-induced dipole potential between gas molecules and ion appreciably influences gas molecule trajectories on close approach to the ion.(Fernández-García and Fernández de la Mora 2014) Based on calculations,(Larriba and Hogan 2013b) the influence of this potential can be accounted for by introducing a correction factor L into equation (3.2a), such that the CCS and mobility equivalent diameter are linked via the equation:

$$\Omega = 1.36L\frac{\pi}{4}\left(d_m + d_g\right)^2 \tag{3.2b}$$

$$L \simeq 1 + \Psi_{pol}\left(0.322 + \frac{1}{1.36}\left(0.0625 + 0.1212\Psi_{pol}\right)\right); \quad \Psi_{pol} < 1 \tag{3.2c}$$

$$\Psi_{pol} = \frac{2\alpha_{pol} z^2 e^2}{\pi\varepsilon_0 (d_m + d_g)^4 kT} \quad (3.2d)$$

where Ψ_{pol} is the potential energy to thermal energy ratio during gas molecule impingement, ε_0 is the permittivity of free space, and α_{pol} is the gas molecule polarizability (in length cubed). In addition to displaying cluster ion mobilities, Table 3.1 also lists the mobility equivalent diameters for all discernable cluster ions calculated via equation (3.1) in conjunction with equation (3.2a) and equation (3.2b). Directly calculated CCSs (in square Å) are also provided in the table.

Of interest is comparison between inferred CCSs/mobility equivalent diameters and predictions based on cluster ion structural models. The examined clusters are in a size/mass range (~1 nm in mobility diameter and <2000 Da) where it is not clear to what extent the CCS can be approximated by the Stokes-Millikan equation, or alternative approaches. A simple assumption adopted in prior work(Jiang et al. 2011d) is that cluster ions are approximately spherical and their mobility equivalent diameters can be determined by assuming that cluster ion densities are similar to bulk densities. Along these lines, Figure 3.5a is a plot of experimentally measured CCS values versus ion masses for the positive cluster ions, as well as CCS calculated using equation (3.2a), with the density of each ion determined based upon the number of dimethylamine molecules (density of 670 kg m^{-3}) and sulfuric acid molecules (1,840 kg m^{-3}) it consists of. As the induced dipole potential correction only changes the inferred mobility equivalent diameter modestly (by several percent), it is neglected in this comparison. A gas molecule diameter of 3 Å was also applied in calculations. Immediately apparent in Figure 3.5a is the Stokes-Millikan based predictions of CCS are higher (by 15% in most

instances) than those inferred from measurement (which are similar in accuracy to the accuracy of the applied voltage), which is in contrast with the assumptions of prior studies. Therefore, caution is advised against direct application of the Stokes-Millikan equation for precise inference of cluster size. At the same time, it may be noted that the Stokes-Millikan inferred mobility equivalent diameters are often within 10% of measurements and may be of use in instances where a rough approximation of size is needed.

Because of the observed disagreement between Stokes-Millikan based predictions and measurements of cluster ion CCSs, a more detailed examination of the link between CCS and cluster ion structure was performed. A key feature of the Stokes-Millikan equation is that it is consistent with models in which gas molecules impinge and are reemitted inelastically and diffusively from ion surfaces (when modeling ions as rigid structures).(Epstein 1924) Several recent studies (Larriba-Andaluz et al. 2015a, Maisser et al. 2015, Ouyang et al. 2013a) have found evidence that such diffuse/inelastic scattering is a reasonable approximation when the gas molecule mass is large relative to the masses of atoms/functional groups comprising the ion (as is the case for organic species in air/nitrogen) but that gas molecule collisions are more specular/elastic when the gas molecule mass is small relative to the species it collides with (as is the case for helium with all species, or air/N_2 with heavier atoms). The reemission model utilized in calculations has a substantial influence on the CCS in the size/mass range examined here, and clusters composed of dimethylamine and sulfuric acid consist of a collection of the

former and the latter. Therefore, it is not clear how gas molecules impinge and are remitted from their surfaces.

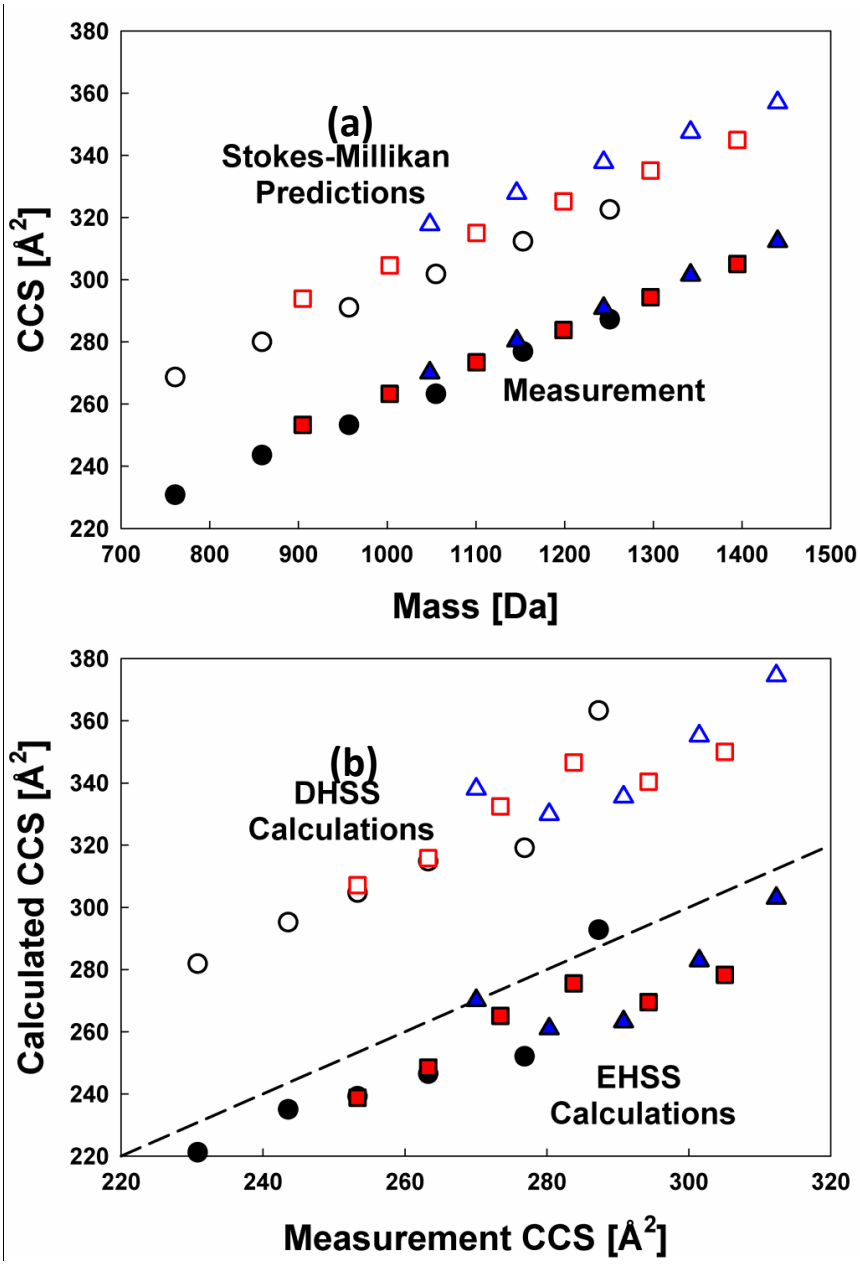

Figure 3.5. **(a.)** The inferred collision cross sections versus cluster ion mass from measurements (closed symbols) and from the Stokes-Millikan equation (open symbols). **(b.)** A comparison of positively charged dimethylamine-sulfuric acid cluster ion collision cross sections (CCSs) determined via gas molecule scattering calculations with computationally generated structures to DMA-MS measurement inferred CCSs. Open symbols denote diffuse/inelastic gas molecule scattering during calculations (DHSS),

while closed symbols denote elastic/specular gas molecule scattering during calculations (EHSS). Circles- Clusters containing six dimethylamine molecules; squares- Clusters containing seven dimethylamine molecules; triangles- Clusters containing eight dimethylamine molecules. A 1:1 guideline is also provided.

To examine predictions with disparate reemission models, structures for positively charged cluster ions were calculated and used the gas molecule scattering calculation approaches developed by Larriba-Andaluz(Larriba and Hogan 2013b, Larriba and Hogan 2013a) to infer CCSs. The structures were calculated by Joseph DePalma and Prof. Murray Johnston at the University of Delaware using the Gaussian09 software package (Gaussian Inc., Wallingford, CT) to calculate local energy minimum candidate structures for each ion. The PM6 semi-empirical parameterization(Stewart 2007) was employed, symmetry restrictions were not applied, and vibration frequencies were calculated. All structures presented showed positive frequencies, indicating they are true local minima structures rather than transition states. For gas molecule scattering calculations, which directly output the CCS for the structure under examination, spherical gas molecules with diameters of 3 Å and polarizabilities of 1.7 $Å^3$ were applied. The van der Waals radii were used to describe the size of each atom in examined cluster structures. CCS calculations were performed at the measurement temperature, using both the diffuse/inelastic (DHSS) and the specular/elastic (EHSS) algorithms. The DHSS algorithm, described by Larriba & Hogan,(Larriba and Hogan 2013b) was developed to lead to agreement between calculations and the Stokes-Millikan equation in the absence of potential interactions. Conversely, the EHSS algorithm, in which gas molecules impinge and are remitted with translational energy conserved, has shown good agreement

with measurements of ion mobilities in helium.(Shvartsburg and Jarrold 1996, Larriba-Andaluz et al. 2015a) Input parameters for calculations are provided in the Appendix.

A comparison of calculated and measured results is provided in Figure 3.5b, and depictions of the cluster structures employed are provided in the Appendix (along with atomic coordinates). As was the case for Stokes-Millikan inferred CCSs, those determined with DHSS calculations are substantially larger than measured values. DHSS calculations differ modestly from Stokes-Millikan predictions, with differences resulting from the asphericity of the ions as well as the influence of the ion-induced dipole potential. Meanwhile, EHSS predicted CCS values are in good agreement with measurements, and we note that there are no fitting parameters in the calculations which give rise to this agreement. This suggests that most gas molecules collide primarily with the heavier sulfate groups in cluster ions, and during such collisions there is little kinetic energy exchange between the ions and gas molecules (the slight underestimation of most CCSs with the EHSS reemission model suggests that gas molecule-ion collisions are not completely elastic and specular, but that there is only a modest degree of energy exchange during each collision). This finding is in line with prior measurements on metal iodide salt cluster ions(Ouyang et al. 2013a) as well as siloxane ions(Maisser et al. 2015) in air, and reinforces the argument that the gas molecule reemission process hinges upon the mass ratio of the gas molecule to the atoms/functional groups comprising an ion. Except in limited circumstances, it is presently not possible to prescribe a precise reemission model *a priori*, hence caution should be exercised in linking mobility

measurements to ion structures and sizes without experimental examination of the reemission process for the gas molecules and ions in question.

3.3.3 Extent of Hydration

A final application of tandem mobility-mass measurements is to infer the extent to which cluster ions uptake water in environments of controlled relative humidity. As noted in the *Experimental Methods* section and in prior studies,(Ouyang et al. 2015, Oberreit et al. 2015, Rawat, Vidal-de-Miguel and Hogan 2015, Meyer et al. 2016, Oberreit et al. 2014) the sheath flow/bath gas of the mobility analyzer is humidified for such measurements, and a shift in mobility/CCS as a function of relative humidity is monitored. When coupled with mass spectrometry, the adsorbed water molecules dissociate from clusters prior to mass analysis. Mass spectrometry therefore merely serves to aid in cluster identification. It is also important to note that for water vapor in differential mobility analysis, cluster ions are in equilibrium with their surroundings. In this case the number of water molecules bound during measurement is not a constant; water molecules are constantly adsorbing and desorbing from cluster ion surfaces and each ion probes the equilibrium distribution of adsorbed water molecules.(Oberreit et al. 2015, Oberreit et al. 2014, Rawat et al. 2015)

For the positively charged ions, the shift in CCS (inferred from the Mason-Schamp equation in all instances) is plotted as a function of water relative humidity in Figure 3.6, while for negative ions shifts results are summarized in Figure 3.7. Shifts are expressed relative to the CCS observed at RH = 3.5% for positive ions and under dry

conditions for negative ions. All examined ions show a detectable shift in CCS, indicating that water does adsorb to cluster ions of both polarities. For the positively charged cluster ions, it is also clear that the more acidic clusters display larger shifts in CCS, indicating that a larger number of water vapor molecules adsorb to such clusters. This is consistent with observations of cluster ion dissociation; excess acid clusters were only found stable under humidified conditions. Presumably, the adsorption of water protects such species in mass spectrometer inlets, as the dissociation of water leads to evaporative cooling, preventing excess acid dissociation. Findings are also in agreement with water uptake measurements made for larger particles,(Ouyang et al. 2015, Qiu and Zhang 2012, Lavi et al. 2013) and suggest that the adsorption of water to dimethylamine-sulfuric acid cluster ions should be considered when modeling the properties (e.g. evaporation rates) of these clusters under atmospherically relevant conditions. At the same time, the extent of water uptake observed is modest. For example, many metal iodide salt cluster ions were observed to have CCS shifts of 10% or larger under similar conditions,(Oberreit et al. 2015) while no observed dimethylamine-sulfuric cluster ion CCS shifts by more than 10%. Though the number of water molecules is not a constant, we can reasonably estimate that for the measured cluster ions in the relative humidity range examined, typically fewer than 10 (and likely fewer than 5) water molecules are adsorbed. Therefore, cluster ions cannot be characterized as droplets or as extremely hydrated species, rather several water molecules are bound to their surfaces.

3.4 Conclusions

Differential mobility analysis in combination with mass spectrometry (a form of IMS-MS) has been applied to examine the stabilities, structures, and hydration of electrospray generated, singly charged clusters of the form $[H((CH_3)_2NH)_x(H_2SO_4)_y]^+$ and $[(HSO_4)((CH_3)_2NH)_x(H_2SO_4)_y]^-$, where $4 \leq x \leq 8$, and $5 \leq y \leq 12$. Despite the use of electrospray ionization to generate cluster ions, detected clusters are similar in chemical composition to those observed in chamber experiments where clusters form from vapor phase precursors.(Bianchi et al. 2014) The results presented in this chapter allow one to make the following concluding remarks:

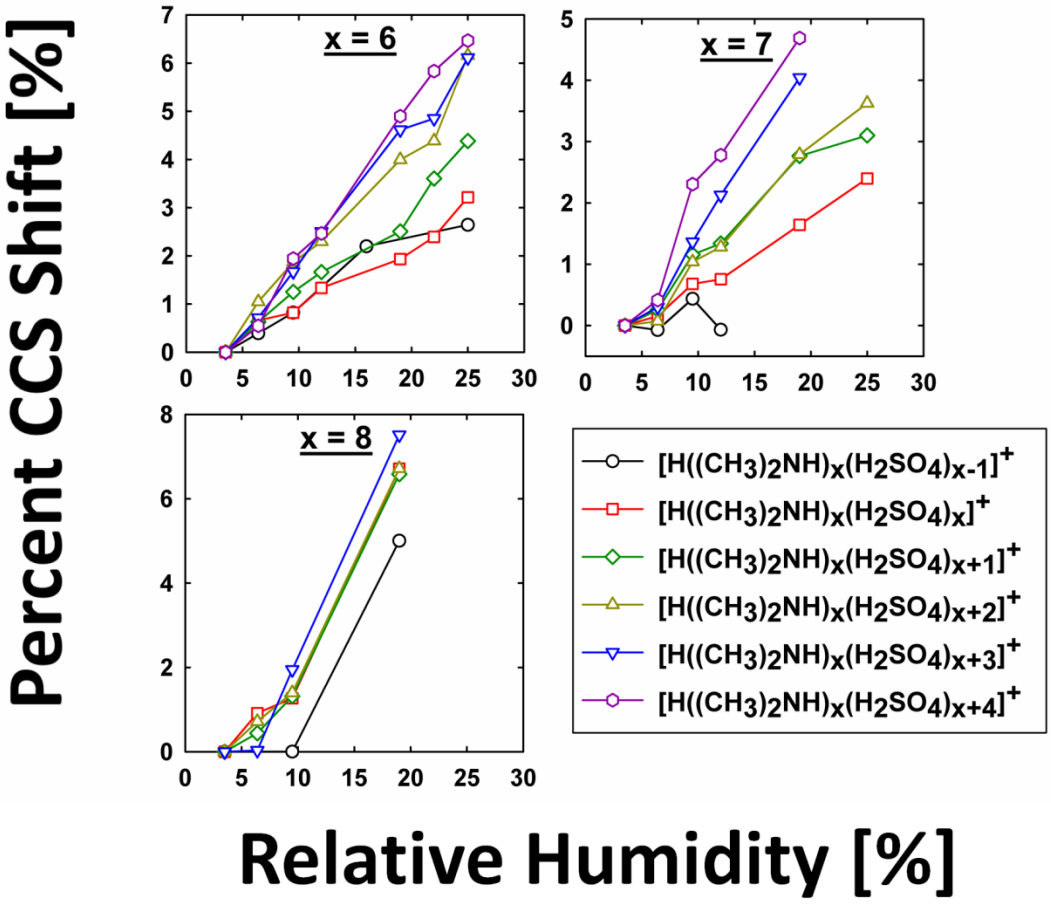

Figure 3.6. The percent shift in collision cross section (CCS) observed for positively charged dimethylamine-sulfuric acid clusters as a function of relative humidity. The three plots are grouped by the number of dimethylamine molecules per cluster ion.

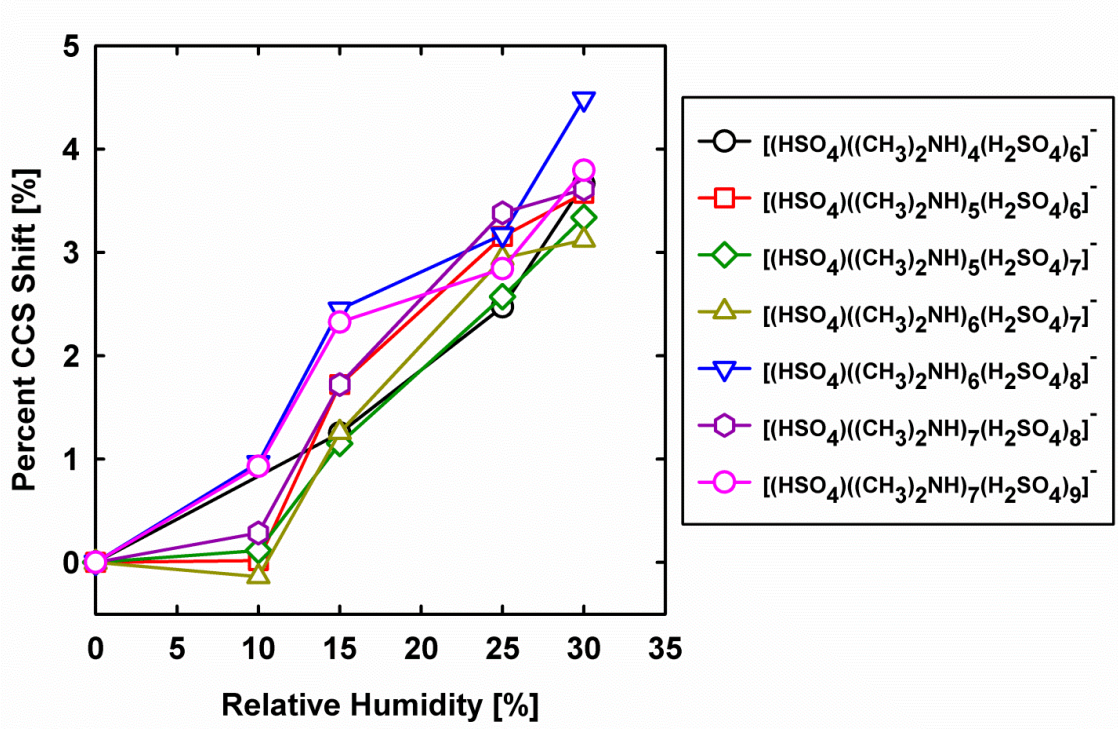

Figure 3.7. The inferred shifts in collision cross sections with change in relative humidity for negatively charged cluster ions.

1. In the absence of water vapor, dissociation of positively charged cluster ions was found substantial in the inlet region of a mass spectrometer designed to sample ions from atmospheric pressure, even when applied potential differences in the inlet were minimized to mitigate dissociation. This prevented clear identification of the mobilities of chemically identified cluster ions. However, with small amounts of water vapor introduced (RH = 3.5%), clusters of the form $[H((CH_3)_2NH)_x(H_2SO_4)_{x-1}]^+$ and $[H((CH_3)_2NH)_x(H_2SO_4)_y]^+$ (with $y \geq x$) were

stable at atmospheric pressure and only dissociated in the mass spectrometer inlet via loss of one or several H_2SO_4. Reduced dissociation permitted identification of the mobilities of a number of ions. As we find that cluster ions with excess sulfuric acid are more hydrated (indicated by larger shifts in their collision cross sections at elevated relative humidity), it is presumably the dissociation of water in the mass spectrometer inlet region which prevented substantial dissociation upon introduction to the mass spectrometer. Caution is advised against utilizing the signal intensities observed in mass spectrometry to quantify absolute as well as relative cluster concentrations; such intensities can be altered via dissociation, which in turn is dependent upon the extent of cluster hydration. I also remark that atmospheric pressure mobility analysis prior to sample introduction into vacuum systems does permit identification of dissociation reactions for cluster ions. Further applications of IMS-MS along these lines may enable better quantification of cluster concentrations in new particle formation studies.

2. In line with other studies,(Larriba-Andaluz et al. 2015a, Maisser et al. 2015, Ouyang et al. 2013a) the presence of high mass sulfate groups in dimethylamine-sulfuric acid cluster ions appears to lead to collisions with gas molecules which are more elastic and specular in nature. In the sub ~2 nm mobility equivalent diameter range, such collisions lead to a reduction in cluster collision cross sections over what is expected based on both the Stokes-Millikan equation(Larriba et al. 2011) and diffuse/inelastic gas molecule scattering models.(Larriba and Hogan 2013b, Larriba and Hogan 2013a) To apply mobility

measurements for more refined structural characterization of clusters in this size range under atmospherically relevant conditions, more detailed study of gas molecule reemission will be required. This will be particularly important in the study of clusters composed of sulfuric acid, amines, and other organic species, as molecular nitrogen and oxygen impingement and reemission from organic ions appears to be more diffuse and inelastic in nature than from inorganic ions.

Chapter 4: Differential Heat and Mass Transfer Rate Influences on the Activation Efficiency of Laminar Flow Condensation Particle Counters

Abstract

Laminar flow condensation particle counters (CPCs) are uniquely sensitive detectors for aerosol particles in the nanometer size range (i.e. below 10 nm in size they can have single particle sensitivity). Their operation hinges upon the creation of supersaturation of a working fluid; particles exposed to supersaturated vapor grow by condensation to optically detectable sizes. The degree of supersaturation is fully controlled via differential rates of heat transfer and working fluid vapor mass transfer. Because of the Kelvin relationship governed vapor pressure of small particles, in all CPCs there is a critical size (diameter), and particles smaller than this size do not grow and are not detected efficiently. While efforts have been made to control the CPC activation efficiency (i.e. the fraction of particles detected as a function of size), prior studies have not examined how differential heat and mass transfer in CPCs are governed by changes in gas composition. Here, CPC activation efficiencies (with n-butanol as the working fluid) are measured and modeled in mixtures of gases of disparate thermophysical properties, namely helium and molecular nitrogen. These experiments show that the activation efficiency of smaller particles (i.e. below 8 nm in the tested CPC) can be increased by adding a modest amount of helium to the aerosol (mole fractions near 0.20). This is expected based upon the increased Lewis number brought about by Helium addition, and

supported by predictions of CPC activation efficiency based upon thermophysical property variable models of coupled heat, mass, and momentum transfer within the CPC. Interestingly, it is found that when operating with a constant precision orifice diameter (choked flow), the activation efficiency for a given sub-10 nm particle diameter first increases with Helium mole fraction and then decreases as the Helium mole fraction increases beyond 0.67. In comparison, experiments with constant mass transfer Peclet number (Pe_m = 77) show an increase in CPC activation efficiency up to a helium mole fraction of 0.67, but then the activation efficiency decreases more modestly beyond this helium mole fraction. These contrasting results are attributed to the increased flowrate through the instrument under constant orifice diameter conditions which affects the performance of the CPC saturator. Finally, through modeling, I show that the ability to enhance the activation efficiency of a CPC via a modest amount of Helium addition is general and can be applied with other heavy working fluids. The results presented in this study elucidate the importance of gas composition and Lewis number controlled differential heat and mass transfer rates on the performance of condensation-based nanoparticle detectors.

4.1 Nomenclature

c	concentration of working fluid [mol m^{-3}]
C_p	specific heat at constant pressure [J kg^{-1} K^{-1}]
$\hat{C}_p$	molar specific heat at constant pressure [J mol^{-1} K^{-1}]

d_c	critical particle diameter [m]
d_p	particle diameter [m]
D_{AB}	binary diffusivity [$m^2\ s^{-1}$]
k	thermal conductivity [$W\ m^{-1}\ K^{-1}$]
k_B	Boltzmann constant [$J\ K^{-1}$]
Le	Lewis number, $k/\rho\ C_p\ D_{AB}$
m	mass of molecule [kg]
M	molecular weight [$g\ mol^{-1}$]
p	pressure [$N\ m^{-2}$]
Pe_m	mass transfer Peclet number, $uL/\ D_{AB}$
Pr	Prandtl number, $\mu\ C_p\ /k$
R	universal gas constant [$J\ mol^{-1}\ K^{-1}$]
Re	Reynolds number, $Lu\rho/\mu$
S	saturation ratio
T	temperature [K]
$\boldsymbol{u}$	gas velocity [$m\ s^{-1}$]
v_m	molecular volume [m^3]
x	species mole fraction

Greek letters

α,β	species indices
γ	working fluid surface tension [$N\ m^{-1}$]

ε	Lennard-Jones energy parameter [J]
η_{CPC}	CPC activation efficiency
θ	dimensionless temperature
μ	gas viscosity [kg m^{-1} s^{-1}]
ρ	gas density [kg m^{-3}]
σ	Lennard-Jones size parameter [m]
τ_v	DMA transfer function
$\phi_{\alpha\beta}$	dimensionless quantities in viscosity and thermal conductivity mixing rules
χ	helium mole fraction
Ω_D	collision integral for diffusivity
Ω_μ	collision integral for viscosity

Subscripts

b	1-butanol
in	saturator conditions
He	helium
N_2	nitrogen

4.2. Introduction

The condensation of supersaturated vapor onto nanoparticles and ions in the gas phase has long been utilized as a measurement method to determine nanoparticle number

concentration, dating to the cloud chamber work of Wilson.(Wilson 1912, Wilson 1897, Wilson 1911) In condensation based detection, the supersaturation of a vapor (termed the working fluid) is controlled, such that the vapor will condense onto nanoparticles, while the rate of homogeneous nucleation remains small.(McMurry 2000) Fast condensation growth kinetics result in nanoparticles growing to supermicrometer sizes, which can enable optical detection of individual particles. This process is utilized in a wide variety of commercially available condensation particle counters (CPCs). There is a wide range of applications of CPCs, including ambient new particle formation monitoring,(Bianchi et al. 2016, Smith et al. 2010a) vehicle emissions monitoring,(Yli-Ojanperä et al. 2012, Collings et al. 2014) nanoparticle concentrations in clean rooms,(Ensor, Donovan and Locke 1987) respirator fit testing,(Holton and Willeke 1987) and nanoparticle exposure assessment in industrial settings.(Schmoll, Peters and O'Shaughnessy 2010, Kuhlbusch et al. 2011, Brouwer, Gijsbers and Lurvink 2004) Given their widespread use, careful characterization of the capabilities and limitations of CPCs is paramount.

Though only investigated in limited circumstances,(Fisenko et al. 2007, Stolzenburg and McMurry 1991, Hering and Stolzenburg 2005, Barmpounis et al. 2018, Lewis and Hering 2013, Kuang et al. 2012) CPC performance is largely dependent upon control over heat and mass transfer to generate a controlled temperature profile and controlled working fluid supersaturation profile. The maximum supersaturation achieved governs the critical size for particles (which is specifically governed by the Kelvin equation);(Stolzenburg and McMurry 1991) particles larger than the critical size will efficiently grow and can be detected, while those smaller than it are not detected

efficiently. While earlier “cloud chamber” experiments utilized a gas expansion to create supersaturation (which is still used in laboratory measurements (Pinterich et al. 2016)), the vast majority of commercially available CPCs generate superstation via two distinct methods: (1) turbulent mixing of hot and cold gas streams,(Wang et al. 2002) and (2) controlled heating and cooling of a laminar flow. (Bricard et al. 1976, Stolzenburg and McMurry 1991) The former method, which was developed in Russia and subsequently Japan several decades ago, (Okuyama, Kousaka and Motouchi 1984, Fuchs 1959, Fuchs and Sutugin 1965) has enabled detection of particles smaller than 2.0 nm in diameter. (Gamero-Castano and Fernandez de la Mora 2000a, Sgro and Fernandez de la Mora 2004, Seto et al. 1997) However, turbulent mixing CPCs often experience day-to-day variability in their saturation profiles and critical sizes, and often have a non-negligible amount of homogeneous nucleation occur during measurement. For this reason, the vast majority of CPCs in use today rely upon heating and cooling of a laminar flow (so-called laminar flow CPCs). In laminar flow CPCs, a nanoparticle laden aerosol is sampled into tube whose walls are saturated with the working fluid vapor and held at a fixed temperature (the saturator). Subsequently, the particle and vapor laden flow passes into a second tube (the condenser) whose walls are held at a different fixed temperature but also saturated with working fluid vapor. The working fluid typically has a larger molecular weight than that the background gas molecules, and the condenser temperature is below the saturation temperature.(Agarwal and Sem 1980, Stolzenburg and McMurry 1991) Therefore, heat transfer from the incoming hot, saturated flow to the walls of the

condenser occurs faster than mass transfer, leading to supersaturation near the centerline of the flow.

Control over the critical size is largely application specific (i.e. the goal in CPC design is not always to minimize the critical size), and since the introduction of laminar flow CPCs,(Agarwal and Sem 1980, Bricard et al. 1976) to control the critical size while avoiding homogeneous nucleation (which occurs when the supersaturation level is too high), a number of researchers have made modifications and improvements to condensation based detection systems. Notably, Stolzenburg and McMurry (Stolzenburg and McMurry 1991) introduced a concentric tube geometry and sheath gas to increase the supersaturation and to maximize particle exposure to the supersaturated region. In doing so, they shifted the CPC critical size with n-butanol as the working fluid from 10 nm to 2.5 nm. Hering and coworkers developed water based CPCs with similar capabilities to the butanol CPCs.(Iida et al. 2008, Hering et al. 2017) Additionally, research focusing on optimization of the working fluid,(Iida, Stolzenburg and McMurry 2009) as well as the saturator and condenser temperature profiles (Kuang et al. 2012, Barmpounis et al. 2018) to maximize the difference between heat transfer and mass transfer rates in organic working fluid CPCs has shown that the critical size can be pushed below 2.0 nm.

Ultimately, efforts to control the critical size via changing the working fluid amount to modulation of the Lewis (*Le*), which is specifically defined as the ratio of the thermal diffusivity $\left(\frac{k}{\rho C_p}\right)$ to the diffusion coefficient of the working vapor in the gas utilized (*D*), and typically governs differential heat and mass transfer in vapor laden systems (Kulkarni et al. 2017, Zhang 2012, Khan and Pop 2010). However, prior work

has only investigated Lewis modulation through working fluid modification (or more indirectly through temperature and flowrate changes). A more direct method of probing how differential heat transfer and mass transfer influence the critical size (and more specifically the activation efficiency curve in a CPC, defined as the fraction of particles grown and detected, as a function of particle size) would be performed by varying the operating gas composition, e.g. by examining performance in variable mixture of helium and molecular nitrogen. Varying the gas composition dramatically influences the thermal diffusivity and has modest influences on the mass diffusivity of the working fluid. Along these lines, examined here is the influence of Lewis number modulation on heat and mass transfer within a laminar flow CPC operating with butanol as the working fluid. Specifically, I report on measurements of the activation efficiency curve using size selected nanoparticles and make numerical predictions of the activation efficiency curve using a variable property coupled heat and mass transfer model of the CPC condenser, applying the Stolzenburg-Graetz (Stolzenburg and McMurry 1991) approach to predict activation efficiency. The results reported inform future CPC design efforts, aid in understanding how coupled heat and mass transfer affect instrument performance, and additionally are useful in understanding how CPC performance changes when examining in non-standard gas compositions (i.e. not in air or molecular nitrogen).

4.3. Experimental & Numerical Methods

4.3.1 Experiment

Figure 4.1(a) shows the experimental setup employed to evaluate the sensitivity of the activation efficiency curve of a clean room model CPC to shifts in gas composition (*i.e.* helium mole fraction); it is based upon prior CPC characterization schemes (Stolzenburg and McMurry 1991, Iida et al. 2009). A steady, polydisperse aerosol was generated using a glowing wire generator, wherein a stream of nitrogen gas flowed (nominally 5 L min^{-1}) past a coil of tungsten wire (diameter of 0.5 mm) subjected to resistive heating by a DC current of 13-16 A.(Peineke, Attoui and Schmidt-Ott 2006) Vaporized metal emanating from the wire homogeneously nucleated downstream, leading to the formation of aerosol of chemical composition WO_x (trace oxygen impurities are sufficient to oxidize tungsten nanoparticles in wire generation sytems). Subsequent coagulational growth resulted in a polydisperse particle population with particle diameters in the 2-20 nm range. Following growth, the aerosol was passed through a tube housing a ^{210}Po alpha particle source, which generated roughly equal concentrations of positively and negatively charged ions (termed bipolar ions) from trace gas impurities present in the flow.(Maißer et al. 2015) When exposed to a sufficiently high concentration (relative to particle concentration) of bipolar ions for a sufficient time, particles in the gas phase attain a steady state charge distribution *via* diffusion charging. At steady-state particles in the 2-20 nm size range are primarily neutral, and the vast majority of the charged particles have ±1 net charge.(Gopalakrishnan et al. 2013a, Wiedensohler 1988) After attaining the steady-state charge distribution, a monodisperse

size fraction of the particles was isolated using a differential mobility analyzer (nano-DMA, TSI, St. Paul, Minnesota). The design and operation of size particular DMA utilized is described in detail previously. (Chen et al. 1998) Briefly, DMAs are used to isolate charged particles with electrical mobilities (charge/drag ratios) in a narrow, prescribed range, which adjustable by tuning the DMA applied voltage (with other operating conditions held fixed). (Knutson and Whitby 1975c) For 2-20 nm nanoparticles exposed to bipolar ions (which are at most singly charged) the electrical mobility can be directly converted into particle diameter,(Larriba et al. 2011) hence the size distribution of particles exiting the DMA was monodisperse and tunable (in the 4-15 nm range in this study). The DMA was operated with a recirculating sheath flowrate 15 L min^{-1}. The aerosol flow rate entering the DMA for classification was the sum of the aerosol flowrates through the detectors downstream, i.e. 1.12 L min^{-1} for the electrometer and a variable flow in the 0.345 to 1.41 L min^{-1} range (depending on the He mole fraction in the experiment) aspirated by the CPC. The excess flow from the aerosol generator was passed through a filter at the polydisperse aerosol inlet of the DMA.

For variable DMA applied voltages (and hence the nominally selected particle diameter in the 4-15 nm range), the concentration of the particles transmitted through the DMA was measured using both a Faraday cup electrometer (Iida et al. 2009) and a TSI Model 3760 CPC (the clean room CPC). The Faraday cup produced a current, proportional to product of the flow rate of aerosol into it and the number concentration of particles; this current was measured by a Keithley 642 electrometer. The flow through the

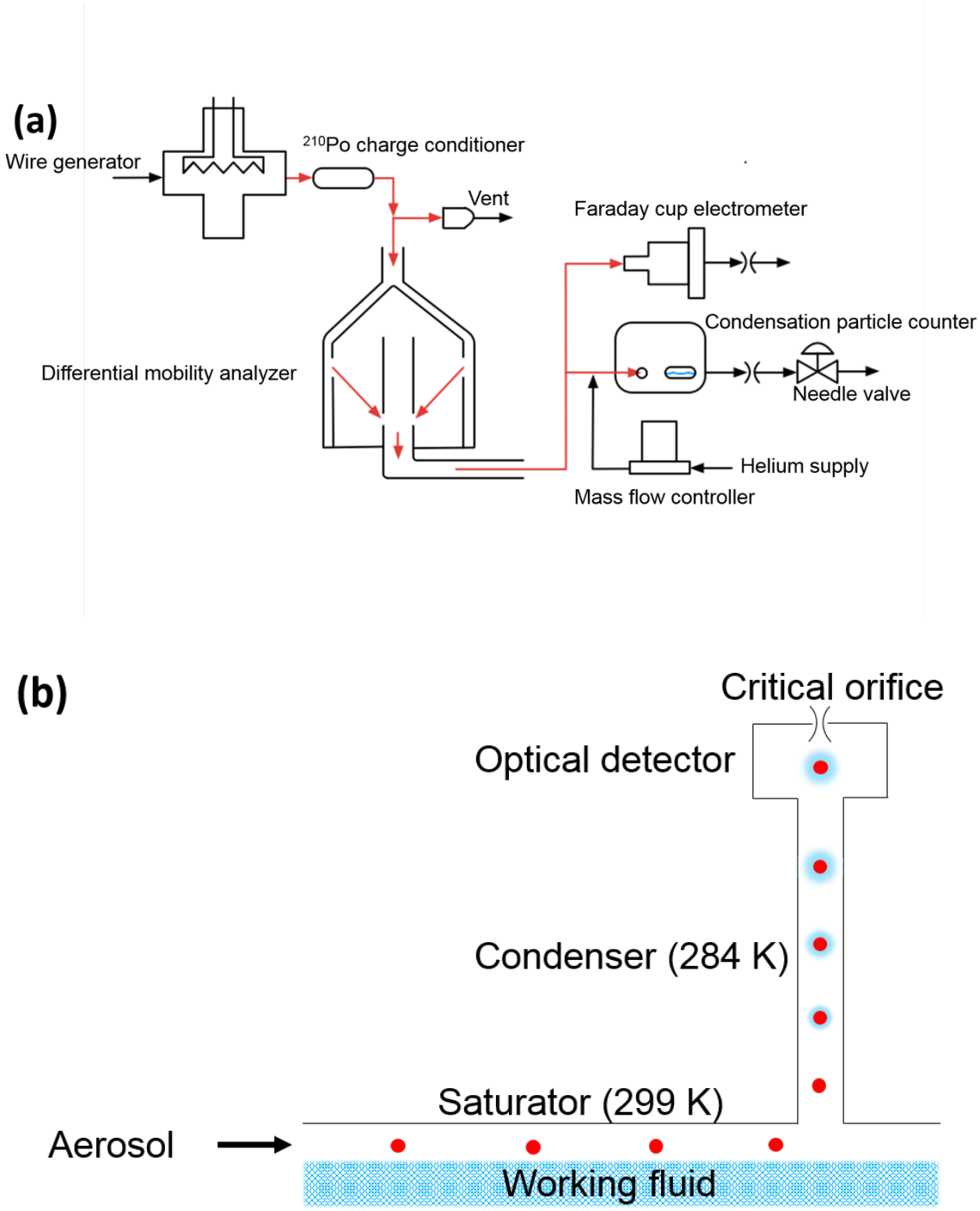

Figure 4.1. Schematic diagrams of **(a)** the experimental setup and **(b)** the TSI CPC 3760 used in the study.

Faraday cup was controlled using a critical orifice. For each measurement, electrometer signal was averaged for 60 seconds using an in-house written LabVIEW program. A schematic of the model 3760 CPC is shown in Figure 1b. Aerosol entering the instrument first passed through the saturator block which consists of a porous wick immersed in a pool of n-butanol held at 299 K. Under default flow conditions (in pure N_2), the aerosol reached this temperature and is saturated with the working fluid at the saturator exit. Next, the aerosol entered the condenser block, which was maintained at 284 K by a thermoelectric cooler. Simultaneous transport of heat and mass to the condenser walls at differing rates leads to a supersaturated region close to the growth tube axis. Particles which are exposed to sufficient supersaturation grow into optically detectable droplets and are detected in the single particle sensitive optical particle counter downstream of the condenser. A precision orifice in the optics block regulates the flow through the device to 1.41 L min^{-1} of nitrogen under choked conditions, and the instrument directly outputs pulse in response to detected particles, which we converted to number concentration via knowledge of flowrate through the optics. The concentration of particles detected by the CPC was corrected by dividing by 1-χ, as the addition of helium diluted the aerosol. For a given DMA setting (and nominal particle size) measurements hence enabled calculation of the ratio of the CPC measured concentration to the electrometer calculated concentration. Measured particle concentrations were near or below 10^4 cm^{-3} in all experiments; under these conditions coincidence errors in the CPC optical unit are negligible and both vapor and thermal depletion (due to condensation) do not have a substantial influence on heat and mass transfer in the CPC.

To examine the influence of gas composition on activation efficiency, helium gas, metered out by a mass flow controller (MKS Instruments), was mixed with the aerosol flow exiting the DMA and prior to the CPC inlet (Figure 4.1a). The aerosol and helium flow rates drawn by the CPC depended upon the gas composition under investigation and the mode of experimentation. Two modes of experiments were performed: (1) constant orifice diameter with choked flow (leading to different flowrates because of the speed of sound differences in N_2 and He) and (2) constant mass transfer Peclet number, Pe_m = 77 based upon saturator temperature. During constant orifice diameter experiments, the default orifice in the CPC was choked with sufficient vacuum pressure. Conversely, an external orifice (of larger diameter) was used in the constant Pe_m experiments as higher total flow rates (than achievable by critical flow with the default orifice) were required for this mode of measurement under certain helium mole fractions. For each helium mole fraction, the classified aerosol flow rate required to maintain the same Pe_m (as the default baseline condition of the CPC in 100 % nitrogen) was attained by adjusting a needle valve placed between the CPC external orifice and the vacuum source, while the helium mass flow controller provided the helium flow desired. Thus, this external orifice was operated under non-critical conditions for constant Pe_m experiments.

In total, I made measurements of the CPC to electrometer number concentration ratio for 20-30 specific DMA applied voltages and He mole fractions of 0, 0.19, 0.40, 0.53, 0.67, 0.76, and 0.88 under both constant orifice diameter and constant Pe_m conditions. Further details on the experiments are noted in Table 4.1. Homogeneous nucleation was not detected at any of these helium mole fractions at appreciably high

rates, such that without voltage applied to the DMA, the detected number concentrations by both instruments was below 1 particle cm^{-3}. With notable exceptions (Iida et al. 2009, Mordas, Sipilä and Kulmala 2008), CPC activation efficiency is often equated directly with the CPC to electrometer number concentration ratio and particle size is equated with the nominal diameter selected by the DMA. As discussed in section 4.4, a data inversion routine (developed by Xiaoshuang Chen in the Hogan group) was used to confirm the activation efficiency as a function of particle diameter.

4.3.2 Model

For every experiment, a prediction of the activation efficiency was made based upon solutions to the governing for coupled mass, momentum, and energy transport in the condenser region of the CPC. The cylindrical geometry of the condenser enables computations in an axisymmetric, two-dimensional model of length 5.1 cm, and radius 0.231 cm. The model used for prediction of activation efficiency includes the coupled equations of continuity (equation 4.1), momentum transport (equation 4.2), energy transport (equation 4.3) and gas phase mass transport of the working fluid (equation 4.4):

$$\nabla^*.(\boldsymbol{\rho}^*\boldsymbol{u}^*) \quad = \mathbf{0} \tag{4.1}$$

$$\rho^*(u^*.\nabla^*)u^* = \nabla^*.\left(-p^*I + \mu^*(\nabla^*u^* + \ (\nabla^*u^*)^T)\right) \tag{4.2}$$

$$\rho^* C_p^* u^*.\nabla^*\theta = \nabla^*.(k^*\nabla^*\theta) \tag{4.3}$$

$$u^*.\nabla^*c^* = \nabla^*.(D^*\nabla^*c^*) \tag{4.4}$$

Table 4.1. Flow rates of the two gases aspirated by the Model 3760 CPC at various experimental conditions. The cut-off size, *i.e* the particle size corresponding to 50% activation efficiency, at each experimental condition is also given. o.d.: orifice diameter.

□	**Experiment mode**	**Nitrogen flow, cm^3 min^{-1}**	**Helium flow, cm^3 min^{-1}**	**Cut-off size, nm**
0.0	Constant o.d. and Pe_m	1410	0	9.44
0.19	Constant o.d.	1180	273	8.48
0.40	Constant o.d.	1000	631	7.51
0.53	Constant o.d.	862	990	6.83
0.67	Constant o.d.	700	1440	6.48
0.76	Constant o.d.	571	1780	7.75
0.88	Constant o.d.	351	2460	8.69
0.19	Constant Pe_m	851	200	6.75
0.40	Constant Pe_m	714	476	6.56
0.53	Constant Pe_m	667	753	6.59
0.67	Constant Pe_m	609	1240	6.23
0.76	Constant Pe_m	546	1730	6.51
0.88	Constant Pe_m	384	2820	7.04

The operators and quantities denoted with "*"are scaled relative to inlet quantities and/or typical scales (average gas speed in the condenser tube for velocity, condenser tube diameter for spatial co-ordinate*s,* as noted in the nomenclature section) Quantities without subscripts refer to properties of the helium-nitrogen gas mixture. Specifically,

$$\rho^* = \frac{T_{in}}{T} \quad \textbf{(4.5)}$$

$$C_p^* = \frac{C_p}{C_{p,in}} \quad \textbf{(4.6)}$$

$$\mu^* = \frac{1}{Re_{in}} \frac{\mu}{\mu_{in}} \quad \textbf{(4.7)}$$

$$k^* = \frac{1}{Re_{in} Pr_{in}} \frac{k}{k_{in}} \quad \textbf{(4.8)}$$

$$D^* = \frac{1}{Re_{in} Pr_{in} Le_{in}} \frac{D}{D_{in}} = \frac{1}{Pe_m} \frac{D}{D_{in}} \quad \textbf{(4.9)}$$

The properties of the nitrogen-helium gas mixture (helium mole fraction □), a function of the composition and temperature, are described by the following ideal gas mixing rules:

$$M = M_{He} + (1 -)M_{N_2} \quad \textbf{(4.10)}$$

$$\rho = \frac{p}{k_B T}\left(m_{He} + (1 -)m_{N_2}\right) \quad \textbf{(4.11)}$$

$$C_p = \frac{\hat{C}_{p,He} + (1-)\hat{C}_{p,N_2}}{M} \quad \textbf{(4.12)}$$

The mixing rule of Wilke (Wilke 1950) for non-polar gases at low densities was used to predict the viscosity of helium-nitrogen gas mixtures at various helium mole fractions. An analogous method, developed by Mason and Saxena, was used to compute the low-density thermal conductivity of the same gas mixture from the values of each component: (Mason and Saxena 1958)

$$\mu = \sum_{\alpha=He,N_2} \frac{x_\alpha \mu_\alpha}{\sum_\beta x_\beta \varphi_{\alpha\beta}} \quad \textbf{(4.13)}$$

$$k = \sum_{\alpha=He,N_2} \frac{x_\alpha k_\alpha}{\sum_\beta x_\beta \varphi_{\alpha\beta}} \quad \textbf{(4.14)}$$

$$\varphi_{\alpha\beta} = \frac{1}{\sqrt{8}}\left(1 + \frac{M_\alpha}{M_\beta}\right)^{-1/2}\left[1 + \left(\frac{\mu_\alpha}{\mu_\beta}\right)\left(\frac{M_\beta}{M_\alpha}\right)^{1/4}\right]^2 \quad \textbf{(4.15)}$$

The diffusivity of the working fluid vapor in the mixture phase was calculated from the binary diffusion coefficients of the working fluid in each individual gas by using Blanc's law: (Marrero and Mason 1972)

$$\frac{1}{D} = \frac{\chi}{D_{bHe}} + \frac{1-\chi}{D_{bN_2}} \quad \textbf{(4.16)}$$

Polynomial model equations were used for component gas specific heat capacities:(Chase 1998)

$$\hat{C}_{p,He} = 2.5R \quad \textbf{(4.17)}$$

$$\hat{C}_{p,N_2} = 28.98641 + 1.853978\left(\frac{T}{1000}\right) - 9.647459\left(\frac{T}{1000}\right)^2 + 16.63537\left(\frac{T}{1000}\right)^3 - 0.000117\left(\frac{1000}{T}\right)^2 \quad \textbf{(4.18)}$$

Chapman-Enskog theory using Lennard-Jones parameters was employed for the viscosities of both gases, the thermal conductivity of helium, and the binary diffusivity of 1-butanol in helium or nitrogen: (Chapman and Cowling 1970)

$$\mu_{He,N_2} = \frac{5}{16}\frac{\sqrt{\pi m_{He,N_2} k_B T}}{\pi \sigma_{He,N_2}^2 \Omega_\mu} \quad \textbf{(4.19)}$$

$$\Omega_\mu = \frac{1.16145}{\left(\frac{k_B T}{\varepsilon}\right)^{0.14874}} + \frac{0.52487}{exp\left(0.77320\frac{k_B T}{\varepsilon}\right)} + \frac{2.16178}{exp\left(2.43787\frac{k_B T}{\varepsilon}\right)} \quad \textbf{(4.20)}$$

$$k_{He} = \frac{25}{32}\frac{\sqrt{\pi m_{He} k_B T}}{\pi \sigma_{He}^2 \Omega_\mu} \quad \textbf{(4.21)}$$

$$D_{\alpha\beta} = 1.8583x10^{-7}\sqrt{T^3\left(\frac{1}{M_\alpha[g/mol]} + \frac{1}{M_\beta[g/mol]}\right)}\frac{1}{p[atm]\sigma_{\alpha\beta}^2[\text{Å}]\Omega_D} \quad \textbf{(4.22)}$$

$$\sigma_{\alpha\beta} = \frac{1}{2}\left(\sigma_\alpha + \sigma_\beta\right) \quad \textbf{(4.23)}$$

$$\varepsilon_{\alpha\beta} = \sqrt{\varepsilon_\alpha \varepsilon_\beta} \quad \textbf{(4.24)}$$

$$\Omega_D = \frac{1.06036}{\left(\frac{k_B T}{\varepsilon_{\alpha\beta}}\right)^{0.15610}} + \frac{0.19300}{exp\left(0.47635\frac{k_B T}{\varepsilon_{\alpha\beta}}\right)} + \frac{1.03587}{exp\left(1.52996\frac{k_B T}{\varepsilon_{\alpha\beta}}\right)} + \frac{1.76474}{exp\left(3.89411\frac{k_B T}{\varepsilon_{\alpha\beta}}\right)} \quad \textbf{(4.25)}$$

Because Lennard-Jones parameters are not available for n-butanol, parameters for n-butane were used in its place. The validity of this assumption was verified by comparison

to available experimental data for n-butanol diffusivity in helium. (Seager, Geertson and Giddings 1963) Finally, Eucken's correlation for the thermal conductivity of polyatomic gases was used to describe the thermal conductivity of nitrogen gas. (Eucken 1913)

$$k_{N_2} = \left(C_{p,N_2} + 1.25\frac{R}{M_{N_2}}\right)\mu_{N_2} \quad \textbf{(4.26)}$$

Lennard-Jones parameters used for equations (4.19-26) are provided in the supplemental information. Together with these constitutive relations, the equations of continuity and transport (Equations 4.1-4) were solved using a finite element method with COMSOL 5.0. A grid independence check was performed for simulations with pure N_2 as the gas and the mesh utilized in this case, which consisted of 75899 domain elements and 2401 boundary elements, was subsequently used for all simulations. Larger element densities were not observed to have an influence on results. For the flow, no slip boundary conditions were used at the tube walls, and the incoming flow profile was assumed to be a fully developed laminar flow corresponding at the volumetric flow rate of the simulation condition. The flow exiting the axisymmetric domain was assumed to be normal to the surface. The inlet flow was also assumed to be fully saturated with the working fluid and in thermal equilibrium with the saturator, while the growth tube walls were held at the condenser temperature and saturated with working fluid vapor at that temperature. Solutions of the temperature and vapor concentration enabled calculation of saturation ratio profiles (the simulated 1-butanol concentration to 1-butanol concentration under saturated conditions) from the knowledge of equilibrium vapor pressure of the working fluid (given by an Antoine relationship for n-butanol (Kemme and Kreps 1969)).

With the saturation ratio profile determined via simulation, the method developed by Stolzenburg & McMurry (Stolzenburg and McMurry 1991) (hereafter termed the Stolzenburg-Graetz approach) was used to compute the activation efficiency of the CPC. This method is based on the fact that the maximum saturation value at any radial location has a monotonic dependence on the radial distance from the tube axis. Corresponding to each maximum saturation ratio value at any given radial location, there is a minimum particle diameter that can be activated to grow, determined by the Kelvin equation:

$$d_c = \frac{4\gamma v_m}{k_B T ln(S)} \quad \textbf{(4.27)}$$

Particles of the critical diameter are exposed to saturation ratios above the critical Kelvin supersaturation at radial locations inner to the location under consideration, and lower saturation ratios at locations radially further. The activation efficiency for the critical Kelvin diameter can hence be approximated as the ratio of particle flux through the disc of radius corresponding to the critical location to the total flux of particles entering the tube (of the critical size). The flux for particles of a given diameter (and hence diffusivity, via the Stokes-Einstein relationship) at each location in the condenser was determined by solving the convective-diffusion equations for particle transport (again via COMSOL 5.0 but without considering variation particle diffusivity due to temperature changes). This approach, which was utilized previously with the analytical Graetz solution for constant property systems, has guided prior CPC design,(Iida et al. 2009) and only makes the simplifying assumption that growth occurs quickly in the condenser for particles greater than the critical diameter.

In addition to comparing empirical activation efficiency profiles to those calculated by the Stolzenburg-Graetz method, this predictive approach was also used to determine the activation efficiency of a CPC using oleic acid as its working fluid (a heavier working fluid than n-butanol) for variable helium mole fraction of the TSI CPC 3760. The operating temperatures for these calculations were set to those used by Iida and co-workers. (Iida et al. 2009) The mixing rules and constitutive equations required to describe substance properties and diffusivities were the same as those used for 1-butanol (equations 10-21 & 23-36). However, equation (22) was replaced with equation (28), following the semi-empirical method of Wilke and Lee, (Wilke 1950) for the prediction of binary diffusivities in the individual gases.

$$D_{\alpha\beta} = 10^{-7}\left(3.03 - \left(\frac{0.98}{M_{AB}^{0.5}}\right)\right) T^{1.5} \frac{1}{p[bar] M_{\alpha\beta}^{0.5} \sigma_{\alpha\beta}^{2}[\text{Å}] \Omega_D} \quad \textbf{(4.28)}$$

$$M_{\alpha\beta} = 2\left(\frac{1}{M_\alpha} + \frac{1}{M_\beta}\right)^{-1} \quad \textbf{(4.29)}$$

Table 4.2. Lennard-Jones parameters used for species employed in this study.

Species	σ/Å	ε/k_B K
Helium	2.576	10.2
Nitrogen	3.667	99.8
n-butanol	5.604	304
Oleic acid	8.81	728

4.3 Data Inversion Scheme

While differential mobility analyzers transmit only a narrow band of particles in terms of electrical mobility, DMA resolution is finite. For this reason, the true activation efficiency $\eta_{CPC}(d_p)$ is linked to the measured CPC to electrometer concentration ratio Ξ_V via the relationship (Iida et al. 2009):

$$\Xi_V = \frac{\int_0^\infty \tau_V(d_p)\eta_{CPC}(d_p)dd_p}{\int_0^\infty \tau_V(d_p)dd_p} \tag{4.30}$$

where $\tau_V(d_p)$ is the transfer function of the DMA for the operating conditions prescribed (Stolzenburg and McMurry 2008). In equation (4.30), is is assumed that the size distribution of produced is particles is broad relative to the width the DMA transfer function. To invert η_{CPC}, a modified version of the method of Buckley & Hogan (Buckley and Hogan 2017) was applied, which is based on the Twomey-Markowski scheme. (Markowski 1987) Details on the inversion are provided in the succeeding paragraphs. Use of this inversion routine ensures that the influence of the DMA transfer function and measurement error on results is accounted for.

Equation (4.30) shows that the ratio of the CPC inferred number concentration (corrected for Helium dilution) to the electrometer inferred number concentration is linked to the DMA transfer function and the CPC activation efficiency curve. More rigorously, this equation should be expressed as:

$$\Xi_V = \frac{\sum_{z=1}^\infty \int_0^\infty f_z(d_p)\tau_V(d_p,z)\eta_{CPC}(d_p)\frac{dn}{dd_p}dd_p}{\sum_{z=1}^\infty \int_0^\infty f_z(d_p)\tau_V(d_p,z)\frac{dn}{dd_p}dd_p} \tag{4.31}$$

where $\frac{dn}{dd_p}$ is the size distribution of particles exiting the wire generator, f_z is the fraction of particles of diameter d_p and charge state z after charge conditioning, $\tau_V(d_p, z)$ is the DMA transfer function with voltage V applied, which depends upon both d_p and z, and $\eta_{CPC}(d_p)$ is the CPC activation efficiency. However, for the size range examined, z = +1 (the DMA selected positively charged particles) is the only non-negligible charge state, and for all DMA applied voltages, the transfer function was extremely narrow compared to $f_1(d_p)\frac{dn}{dd_p}$, hence $f_1(d_p)\frac{dn}{dd_p}$ could be approximated as uniform over the integrals in the numerator and denominator of equation (4.31). These simplifications lead to equation (4.30).

The challenge still remains to infer the function $\eta_{CPC}(d_p)$ for Ξ_V measured at 20-30 distinct DMA voltages for each Helium mole fraction. Using each set of data, a modified version of the algorithm described by Buckley & Hogan (Buckley and Hogan 2017) was used to infer $\eta_{CPC}(d_p)$. In all cases, the diffusing transfer function described by Stolzenburg & McMurry (Stolzenburg and McMurry 2008) was utilized to compute $\tau_V(d_p)$ (with z = 1 assumed). First, equation (4.30) was rearranged to calculate the "signal", y_V (units of length) at each DMA applied voltage:

$$y_V = \Xi_V \int_0^\infty \tau_V(d_p, z) dd_p = \int_0^\infty \tau_V(d_p, z)\eta_{CPC}(d_p) dd_p \qquad \textbf{(4.32)}$$

An initial guess function for $\eta_{CPC}(d_p)$ was developed, which we denote as $\eta_{CPC}(d_p)|_0$, by first equating it with Ξ_V. For this initial guess d_p is based upon the maximally transmitted diameter for each DMA applied voltage. Intermediate values to specific d_p

are fit via linear interpolation, leading to $\eta_{CPC}(d_p)|_0$ represented at *m = 100* specific points, which is larger than the number of DMA applied voltages *n*. $\eta_{CPC}(d_p)|_0$ was iteratively adjusted with Twomey-Markowski loops, subsequently generating $\eta_{CPC}(d_p)|_1$, $\eta_{CPC}(d_p)|_2$, … $\eta_{CPC}(d_p)|_i$, where $\eta_{CPC}(d_p)|_i$ denotes trial activation efficiency curve *i*. In each Twomey-Markowski iteration, the trial solution of $\eta_{CPC}(d_p)|_i$ is first smoothed by Markowski's smoothing routine (Markowski 1987) designed to remove inversion derived oscillations in the trial solution:

$$\eta_{CPC}(d_{p,j})|_i = \frac{\eta_{CPC}(d_{p,j-1})|_i}{S_f} + \frac{\eta_{CPC}(d_{p,j})|_i(S_f-2)}{S_f} + \frac{\eta_{CPC}(d_{p,j+1})|_i}{S_f},\ j = 2\ to\ m-1$$

(4.33-a)

$$\eta_{CPC}(d_{p,1})|_i = \eta_{i,CPC}(d_{p,1}) \quad \textbf{(4.33-b)}$$

$$\eta_{CPC}(d_{p,m})|_i = \frac{\eta_{i,CPC}(d_{p,m-1})}{2S_f} + \frac{\eta_{i,CPC}(d_{p,m})(2S_f-1)}{2S_f} \quad \textbf{(4.33-c)}$$

S_f is a smoothing factor set to a value of 4. Smoothing is not applied to the initial guess function, but is applied to all other trial solutions. Upon each smooth step, the chi-square error $(\chi^2|_i)$ between the measurement and equation (4.32) prediction is calculated via the equation:

$$\chi^2|_i = \sum_V \frac{\left(\frac{y_{i,V}-y_V}{Ey_{V,max}}\right)^2}{n} \quad \textbf{(4.34)}$$

where the summation is over all measurements for a given Helium mole fraction, $y_{i,V}$ is the equation (4.32) calculated value of y_V based on the smoothed function $\eta_{CPC}(d_p)|_i$ and $y_{V,max}$ is the largest value of y_V for the Helium mole fraction examined. *E* is the

measurement error, equated here with 0.10, which the noted intrinsic measurement error for CPCs and significantly larger than counting statistic errors or other errors associated with the flow system. The smoothing process (equations S3a-c) is continuously applied until 1000 smoothing steps are repeated or until $\chi^2|_i > S_{lim}$. The smooth limit, S_{lim}, was lowered from 1 (as used Buckley & Hogan (Buckley and Hogan 2017)) to a value much less than 1 (shown in Table 4.3), because for CPC activation efficiency curves, even the initial guess yields $\chi^2|_0 \ll 1.0$. After the Markowski smoothing process, the smoothed trial solution $\eta_{CPC}(d_p)|_i$ is modified by a Twomey iteration until $\chi^2|_i < S_{lim}$ by calculating a new trial activation efficiency curve:

$$\eta_{CPC}(d_p)|_{i+1} = \left[1 + \frac{\left(\frac{y_V}{y_{i,V}} - 1\right)\tau_V(d_p)}{F}\right] \times \eta_{CPC}(d_p)|_i \tag{4.35}$$

After generating a new solution, equation (4.34) is then used to compute the chi-square error, and the equation (4.35) is applied iteratively until $\chi^2|_i < S_{lim}$ or until 2010 cycles pass. In equation (4.35), F is a correction factor design to prevent inversion overcorrection; here $F = 10$ is applied for the first 10 iterations and then for subsequent iterations, $F = 1$ is utilized.

At the end of each Twomey loop, the roughness of the solution is calculated following equation (12) of Buckley & Hogan (Buckley and Hogan 2017) (substituting in $\eta_{CPC}(d_p)|_i$ as the appropriate test function). If the roughness has decreased, the trial solution is further adjusted through Markowski smoothing (equation 4.33) and Twomey iteration (equation 4.35). Smoothing and Twomey iteration are continued until either the roughness is found to increase from one solution to the solution obtained from a previous

Twomey-Markowski iteration (in which case the prior solution is taken as an appropriately inverted function $\eta_{CPC}(d_p)$), or after 1000 total iterations have been carried out. For all examined cases, fewer than 1000 iterations (typically of order 10^2 iterations) were required for the inversion routine to exit and obtain a solution of minimum roughness satisfying the input χ^2 requirements.

Figure 4.2 displays equation 4.32 calculated y_V (from raw data), as well as a comparison between the $y_{V,i}$ for the final solutions we arrived at for selected He mole fraction. There is minimal change between the raw data calculated signal and final signal (from the inverted function), indicating that the inverted activation efficiency curves do represent the true CPC activation efficiency curves. Figure 4.3 shows a comparison between the initial guess activation efficiency and the final activation efficiency, for variable input S_{lim}, showing the influence this parameter on the result. Appropriately chosen values of S_{lim} lead to the removal of oscillations in the initial guess without other noticeable change in activation efficiency curve. Meanwhile values of S_{lim} which are too large lead to "oversmoothing" and values of S_{lim} which are too small lead to inversion induced oscillations in results. Overall, the inversion process minimally influences the conclusions of this work, i.e. it is found that raw data are quite similar to the activation efficiency curves. Nonetheless, it is important to establish data inversion routines to determine instrument response functions. Use of an inversion routine would be of greater importance for broader DMA transfer functions, i.e. in determining CPC activation efficiency for sub 2.0 nm diameter particles with conventional DMAs.

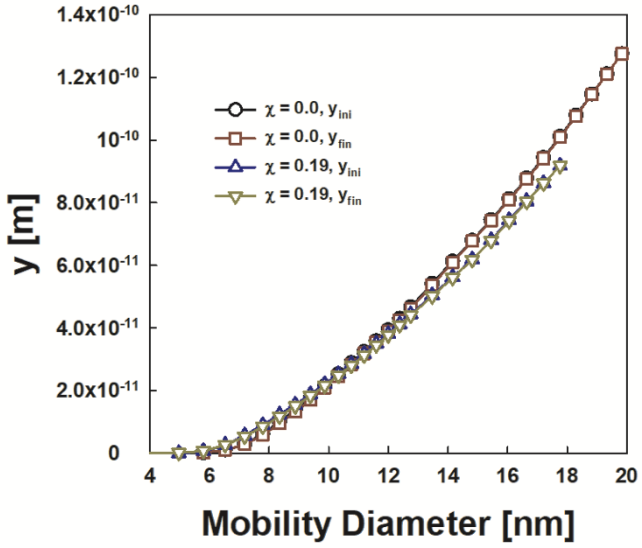

Figures 4.2. The raw data calculated signal (y_{ini}) and inverted activation efficiency curve calculated (y_{fin}) signal for Helium mole fractions of 0.0 and 0.19 from constant orifice diameter experiments.

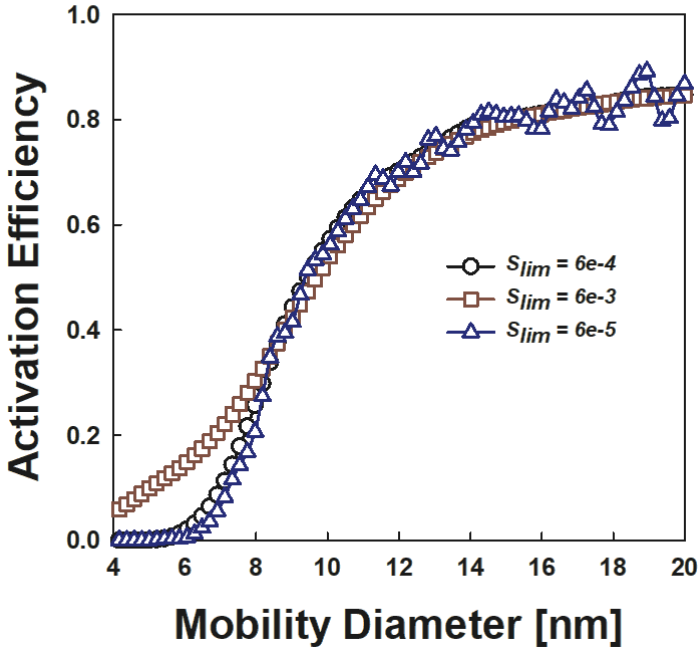

Figures 4.3. Plots of inversion determined $\eta_{CPC}(d_p)$ curves for Helium mole fractions of 0.0 with three input values of S_{lim}.

4.4 Results & Discussion

4.4.1. Activation Efficiency Curves

Helium has a higher thermal conductivity than molecular nitrogen, and although the diffusivity of n-butanol is higher in helium than in molecular nitrogen, the mixture laws invoked (i.e. equations 4.14-26) suggest that as the helium mole fraction increases,

Table 4.3. Values of S_{lim} used in the inversion algorithm for different experimental conditions.

χ	Experiment mode	S_{lim}
0.0	Constant o.d. and Pe_m	6.0e-4
0.19	Constant o.d.	6.0e-4
0.40	Constant o.d.	4.0e-3
0.53	Constant o.d.	3.0e-3
0.67	Constant o.d.	4.0e-4
0.76	Constant o.d.	5.0e-4
0.88	Constant o.d.	1.0e-2
0.19	Constant Pe_m	5.5e-2
0.40	Constant Pe_m	2.5e-2
0.53	Constant Pe_m	6.0e-2
0.67	Constant Pe_m	5.0e-2
0.76	Constant Pe_m	4.0e-2
0.88	Constant Pe_m	1.15e-2

the Lewis number should increase (at low helium mole fractions).(Chapman and Cowling 1970) As the Lewis number defines the differential rate of heat to mass transfer, the addition of helium should increase the activation efficiency for smaller sized particles. The activation efficiency curves (as a function of inferred mobility diameter after inversion) for constant orifice diameter and constant mass transfer Peclet number (Pe_m, equation 9) are shown in Figures 4.4a-b and 4.4c-d, respectively. Results for χ = 0.19-

0.53 are shown in Figures 4.4a & 4.4c, while χ = 0.67-0.88 are shown in Figures 4.4c & 4.4d, with the χ = 0.0 activation efficiency curve shown in all plots for reference. Results for the "cut-size", i.e. the particle diameter corresponding to an activation efficiency of 0.50, are also summarized in Table 4.1. All activation efficiency curves increase with increasing particle diameter, approaching 1.0 for sufficiently large particles. We note for several constant Peclet number mole fractions, there are non-monotonic oscillations in the activation efficiency curves; these were present in raw data, and while a smoothing

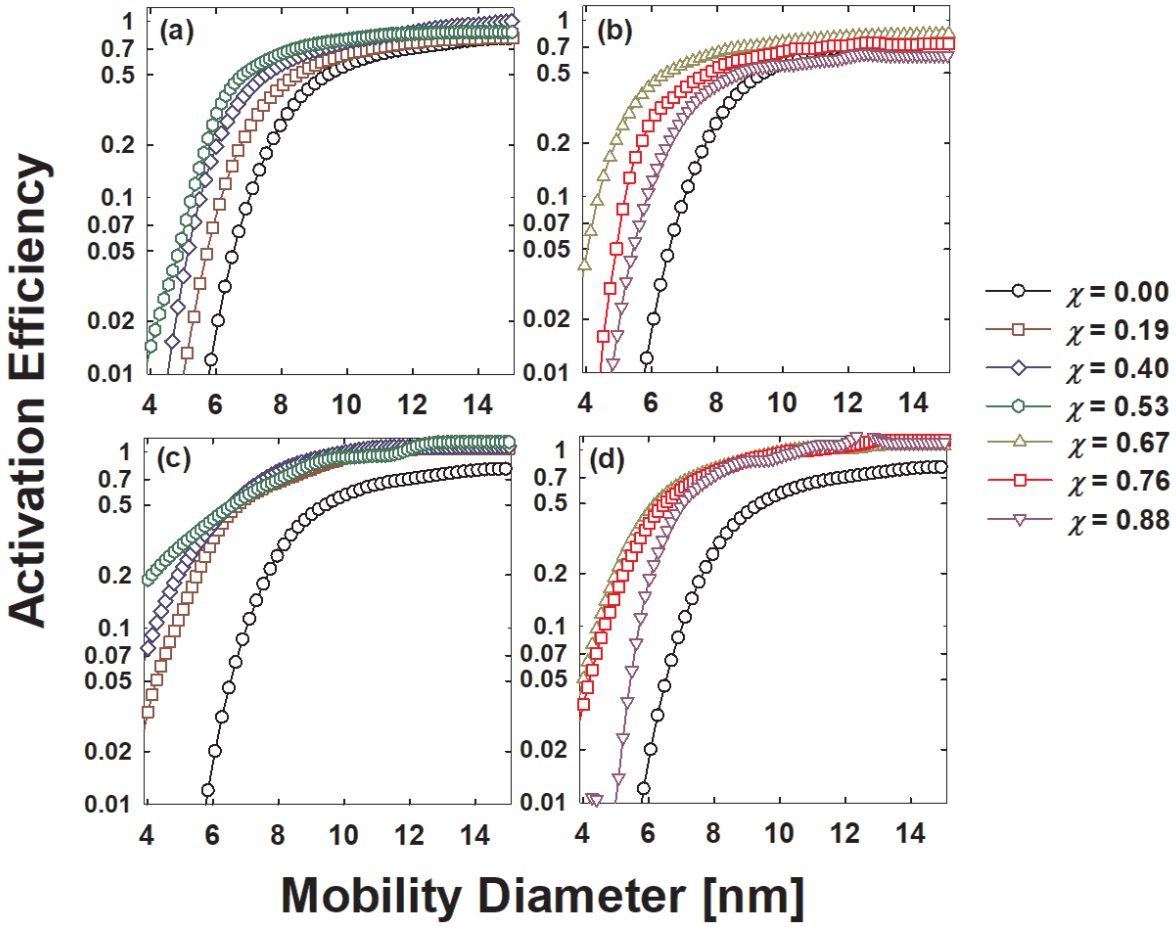

Figure 4.4. The inverted activation efficiency as a function of particle diameter (mobility diameter) for constant orifice diameter (**a&b**) and constant Pe_m (**c&d**)

procedure is incorporated into activation efficiency curve inversion (as described in the supplemental information), this does not completely remove such oscillations from inverted results. I do not comment on these oscillations further, however, as I believe them to be simply a measurement artifact. Focusing first on the constant orifice diameter experiments, consistent with predictions, as χincreases from 0.0 to 0.67, the activation efficiency for sub 8 nm particles increases monotonically, and that the cut-size decreases from near 9.4 nm to below 6.5 nm. This approximately corresponds to factor of two decrease in the surface area of the detectable particles, and only required a minor change to CPC operation. However, the monotonic increase in activation efficiency does not continue as the helium mole fraction is further increased. Shown in Figure 4.4b, as χ increases beyond 0.67 the activation efficiency at smaller sizes decreases. While this may be attributable to a decrease in Lewis number at higher Helium mole fraction (due to the non-linear manner in which Lewis number depends upon gas composition) it is additionally affected by the variable Peclet number for the flow through the saturation and condenser. The Peclet number increases with increasing helium mole fraction (because of the higher speed of sound in helium), and at sufficiently high Peclet number, the flow exiting the saturator will not be fully saturated with the working fluid. It is for this reason that I opted to perform constant Peclet number experiments (though it is remarked that constant orifice diameter would be the more tractable approach to implement of activation efficiency via gas composition modulation). As evidenced in Figures 4.4c & 4.4d, with constant Peclet number, as χ increases from 0 to 0.19, it is again found that the activation efficiency increases for smaller particles. However,

further increasing χ in the 0.53 to 0.76 range leads to little change in the activation efficiency curve. A decrease in the activation efficiency for smaller particles is again observed as χincreases from 0.76 to 0.88. This suggests that the decrease in activation efficiency at higher helium mole fractions when using a constant orifice diameter is largely, but not completely attributable to greater convective effects in the saturator.

4.4.2. Comparison to Simulation

In addition to comparing constant orifice diameter and constant Peclet number scenarios to one another experimentally, simulations to better under understand the non-monotonic dependence of the activation efficiency (at a given diameter) on helium mole fraction. The saturation ratio profiles in the condenser are displayed as contour plots in Figures 4.5a & 4.5b for constant orifice diameter and constant Peclet number simulations. For each contour plot, inlet Lewis number and maximum saturation ratio (found within the entire simulation domain) are labelled. Temperature contour plots for the same conditions are shown in Figure 4.6, and it is evident that the temperature profile develops fast as expected for this system with $Le > 1$. Saturation ratio profiles are hence largely determined by the vapor concentration profiles. Consistent with experimental observations, the highest Lewis numbers and saturation ratios are between χ = 0.53-0.67, the largest increase in Lewis number and saturation ratio occurs between χ = 0.0 and χ = 0.19, and beyond χ = 0.67 the Lewis number and maximum saturation ratio decrease slightly. A difference between constant orifice diameter and constant Peclet number with regards to the shape and location of the elevated saturation ratio region is also evident.

With constant orifice diameter, the region of maximum supersaturation shifts closer to the condenser inlet and decreases in length as χ increases. With constant Peclet number, a shift in size and location of the maximum supersaturation region is observed at low He

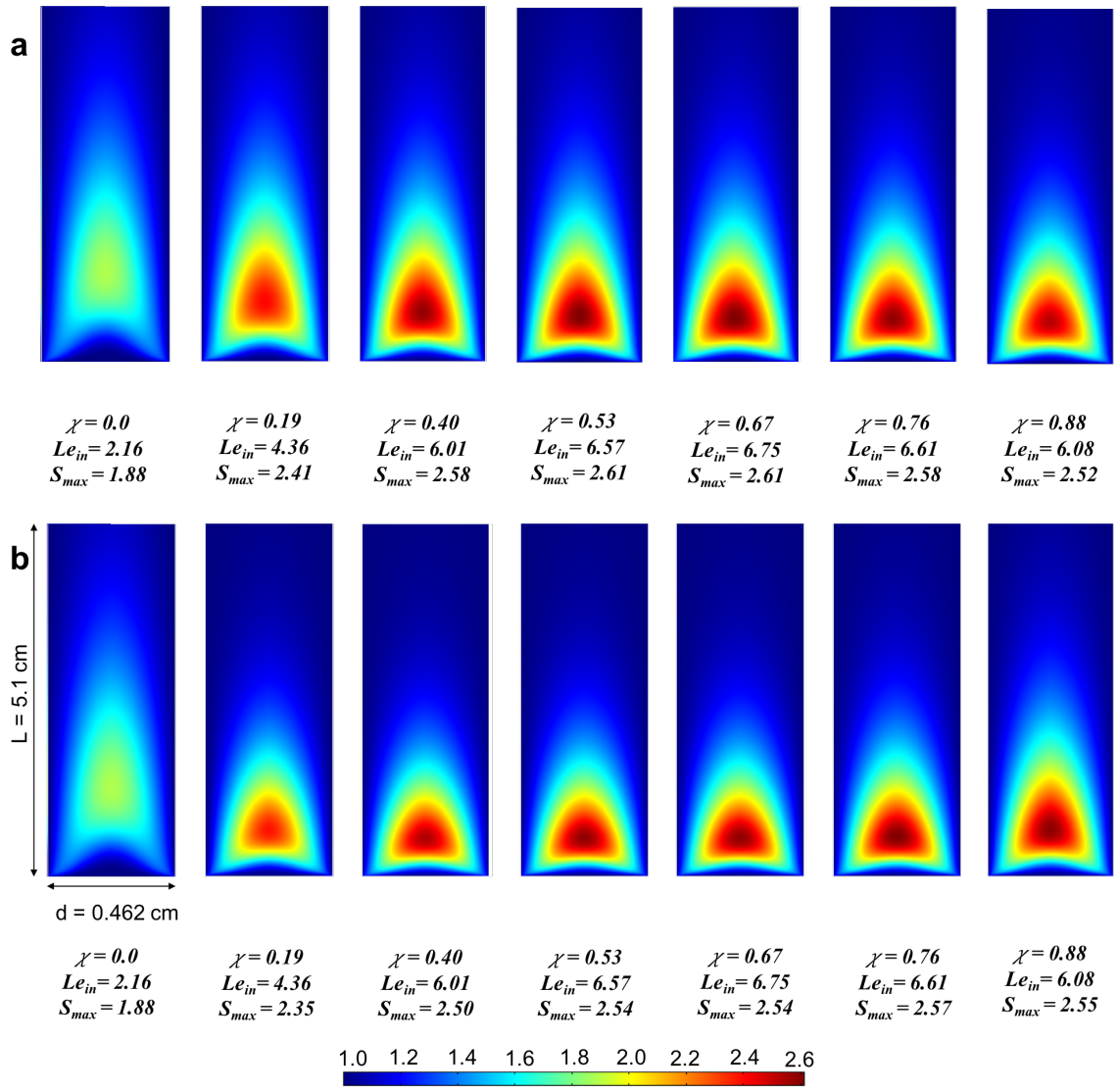

Figure 4.5. Contour plots of the saturation ratio (noted via color, as per the legend) in the condenser simulation with **(a)** constant orifice diameter and **(b)** constant Pe_m conditions for variable helium mole fraction (χ). The maximum saturation ratio for each condition is noted as is the inlet Lewis number Le_{in}. The dimensions of the condenser are noted in **(b).**

mole fraction but after the point maximum Lewis number, the region of maximum supersaturation begins to shift back towards its original location.

Figure 4.7 displays comparison of Stolzenburg-Graetz (Stolzenburg and McMurry 1991) predicted activation efficiency curves and curves inverted from experiments. In general modeled results are consistent with measurements; as helium mole fraction increases, at first there is an increase in the activation efficiency curve for smaller

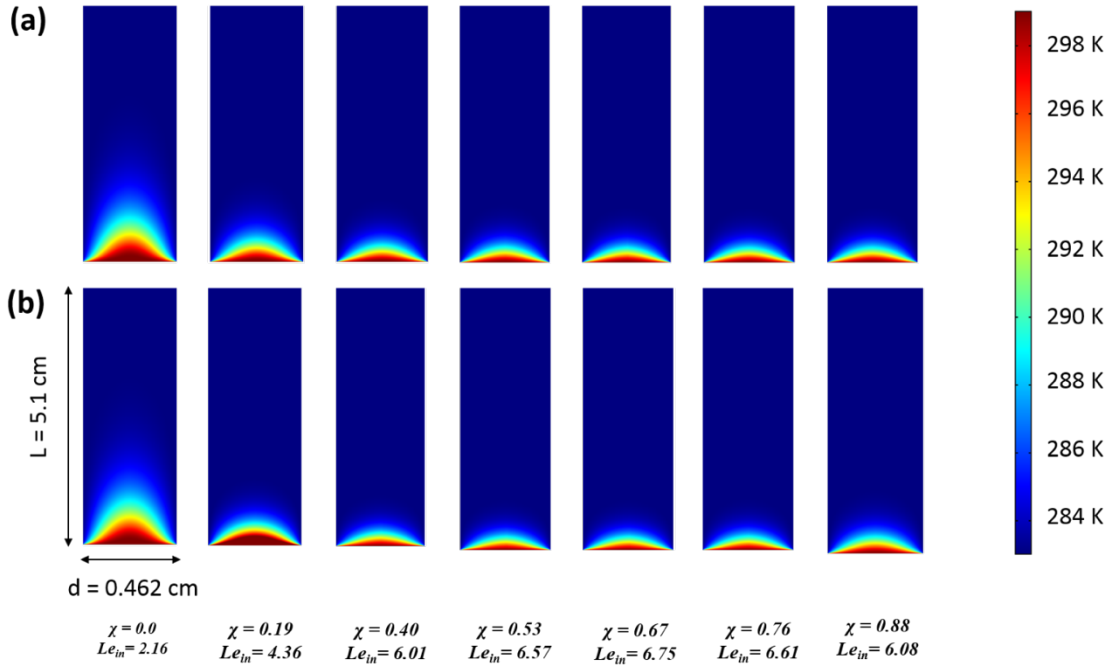

Figure 4.6. Contour plots of the temperature in the condenser simulation with **(a)** constant orifice diameter and **(b)** constant Pe_m conditions for variable helium mole fraction (χ). The dimensions of the condenser are noted in **(b).**

diameter particles (improved activation efficiency), but at increasing the helium beyond 0.53 results in a small, but perceptible shift of the activation efficiency curve towards its baseline (i.e. the 100% N_2 curve). There are quantitative differences between measurement inferred and predicted curves. These differences can be attributed to (1) the

assumption that the flow exiting the saturation is perfectly saturated with n-butanol at the saturator temperature (this assumption would break down as the flow rate increases as in constant orifice diameter experiments), (2) the boundary conditions in simulations effectively have a discontinuity at the inlet (the saturation temperature and working fluid concentration is assumed at the inlet, while the condenser temperature and working fluid concentration are assumed fixed at different values at the condenser walls), and (3) the Kelvin equation assumes perfect binding of vapor molecules to nanoparticles upon collision, and hence may be a lower limit for the critical size. Correcting (1-3) in modeling would require high precision measurements of the vapor concentration and temperature profiles in the condenser inlet region as well as fundamental studies of condensation kinetics. Nonetheless, even without these corrections, it is inferred that the Stolzenburg-Graetz can be applied to examine the extent of expected activation efficiency curve shift brought about by gas composition modulation, and hence confirmed that it can serve as a general design tool in CPC development. An even simpler approach than application of the Stolzenburg-Graetz method can be utilized to predict how the CPC activation efficiency curve will shift in response to gas composition modulation. Figure 4.8 displays plots of the n-butanol diffusivity, the gas thermal diffusivity, and the Lewis number calculated at the condenser inlet/saturator outlet conditions using equations (4.10-4.26) as functions of helium mole fraction.

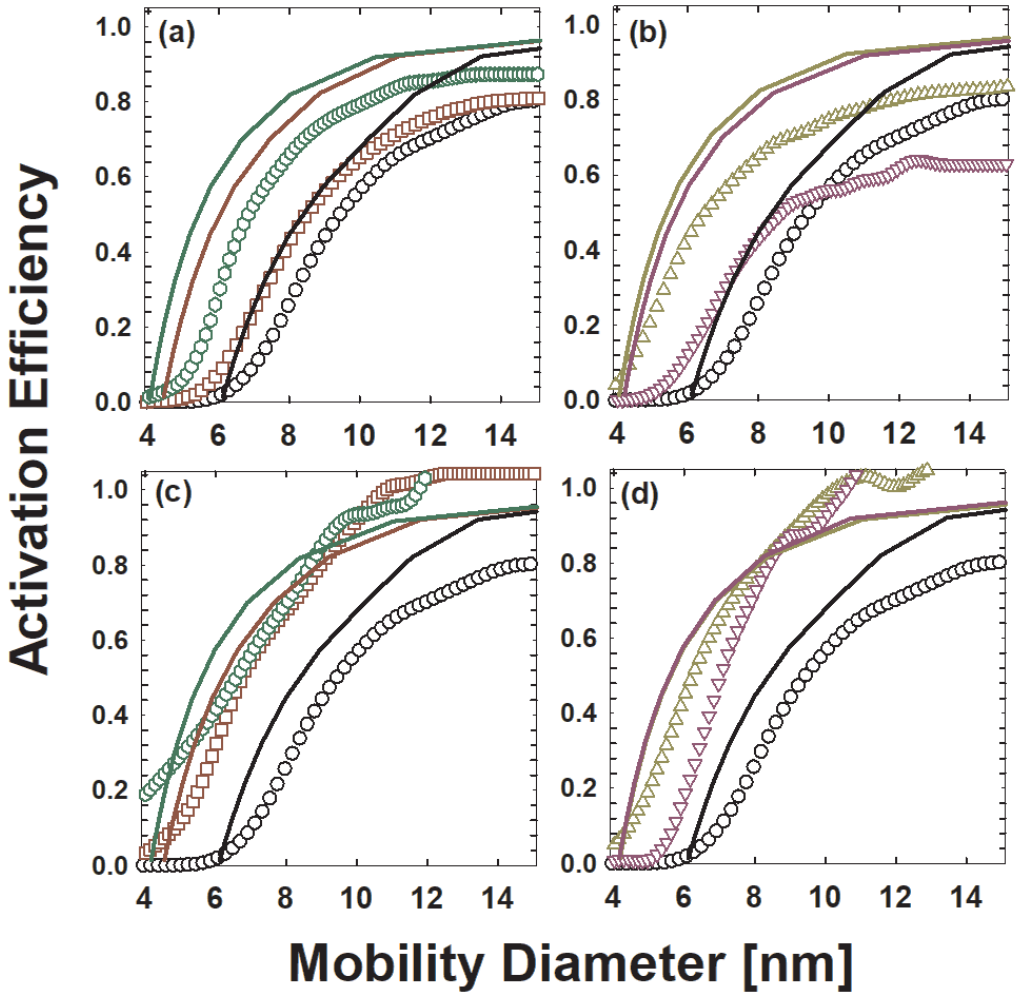

Figure 4.7. A comparison of the inverted activation efficiency as a function of particle diameter (mobility diameter) for constant orifice diameter (**a&b**) and constant Pe_m (**c&d**) experiments to predictions based upon the Stolzenburg-Graetz approach. Symbols: experimentally inverted activation efficiencies. Lines: Stolzenburg-Graetz predictions. The legend for figure 4.2 identifies the He mole fraction for set of symbols, and lines are matched in color to the experimental conditions they represent.

The maximum in Lewis number occurs near χ = 0.65, entirely consistent with measurements. I suggest that such simplified calculations coupled with the Stolzenburg-Graetz approach be employed in designing laminar flow CPCs to optimize differential

heat and mass transfer. (Lewis and Hering 2013, Stolzenburg and McMurry 1991, Barmpounis et al. 2018)

In general, my results show that increasing the helium mole fraction to the 0.20-0.40 range leads to significant shift in the activation efficiency curve and shifting beyond this mole fraction does little to drive further shifts. A question becomes whether this results is specific to n-butanol or if it can be generalized to other working fluids. Iida et al (Iida et al. 2009) theoretically examined more than 100 potential CPC working fluids in terms of their vapor pressures, surface tensions (influence the Kelvin critical diameter), and toxicity. Resulting from this analysis they found that oleic acid enables condensation onto smaller particles operating with a saturator temperature of 337.25 K and a condenser temperature of 289.25 K. Figure 4.9 displays Stolzenbrug-Graetz predicted activation efficiency for an oleic acid working fluid CPC using the same condenser dimensions and baseline flowrate as employed here, but with the noted saturator and condenser temperatures. Curves are shown for variable helium mole fraction at constant Peclet number (Pe_m = 144). A smaller, but still detectable shift is evident in the activation efficiency curve with helium added to the gas, but beyond a mole fraction of 0.40, the activation efficiency curve is relatively insensitive to helium mole fraction. This indicates that the ability to shift activation efficiency and control differential heat and mass transfer in CPCs is not specific to any single working fluid, but that the extent of curve shift is largely working fluid dependent.

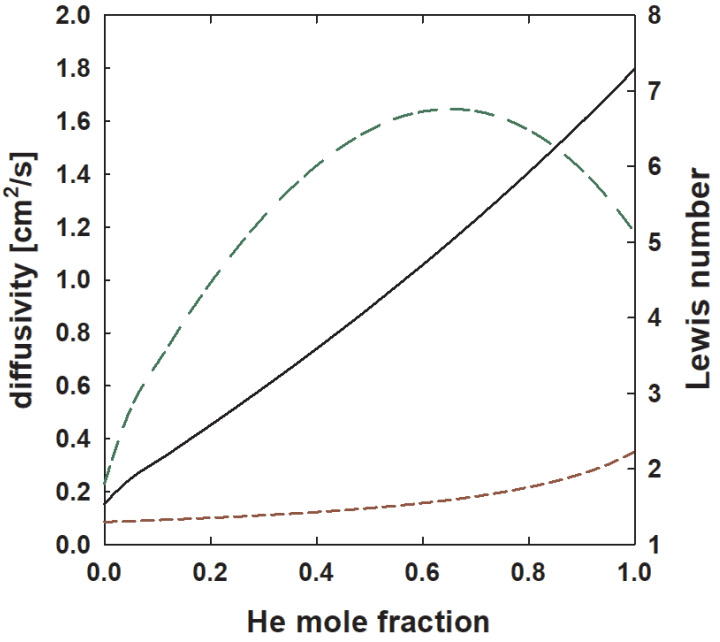

Figure 4.8. The thermal diffusivity (black solid line), the n-butanol mass diffusivity (brown dashed line) and Lewis number (green dashed line) as a function of He mole fraction at 299 K (the saturator temperature) and atmospheric pressure.

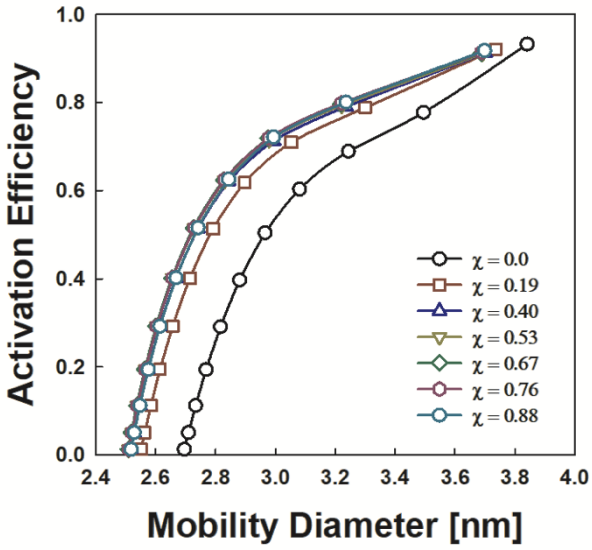

Figure 4.9. The Stolzenburg-Graetz predicted activation efficiency curve with Oleic acid as a working fluid for variable He mole fractions at constant Pe_m. The saturator temperature is 337.25 K and the condenser temperature is 289.25 K, following Iida et al.(Iida et al. 2009)

4.5. Conclusions

I have utilized a combination or experiments and numerical modeling to examine how gas composition modulation influences differential heat and mass transfer within a laminar flow CPC, which ultimately influences the fraction of particles detected as a function of particle diameter (the activation efficiency curve). Based on our empirical and numerical studies, we make the following concluding remarks:

1. The differential rates of heat and mass transfer can be modulated in a CPC growth tube by employing mixtures of gases of disparate properties. Specifically, adding Helium corresponding to a mole fraction between 0.40 and 0.67 enhances the performance of laminar flow CPCs using n-butanol as the working fluid. Further increase in the helium mole fraction does not improve the activation efficiency, as the Lewis number slightly decreases.
2. Modeling simultaneous heat and mass transfer enables prediction of activation efficiency curves following the Stolzenburg-Graetz technique. This approach is largely successful in predicting how the activation efficiency curve shifts in response to changes in gas composition. A simpler method, involving the calculation of the Lewis number of the gas mixture-working fluid system, is also able to predict the mole fraction at which activation efficiency is maximized for the CPC.
3. The experiments performed in this study were in a low particle concentration limit, such that the influences of condensational heating and vapor concentration reduction on the condenser temperature and vapor concentration profiles,

respectively, were negligible. Future studies, including models coupling condensational heating to heat and mass transfer, will be necessary to better understand how the interplay particle concentration and gas composition (the modulation of which involves dilution) govern activation efficiency. Also of interest are models of turbulent mixing CPCs, the design of which has been largely empirical to date.

Chapter 5: Drift tube mobility spectroscopy for size measurement of 4-40 nm particles

Synopsis

Temporal ion mobility spectrometers, also known as drift tubes, possess several advantages over spatial ion mobility classifiers, such as DMAs. These include the ability to reduce sampling time, potentially higher resolving power, and simpler instrumentation owing to the avoidance of turbomachinery associated with DMAs. However, drift tubes are most commonly used in the study of sub – 2 nm ions and molecular clusters and not in the size distribution function measurement of aerosols. Recently, the challenges encountered in the extension of drift tubes to the regime of aerosol science were overcome. A drift tube was developed which was capable of measuring particles in the 2 to 11 nm size range, its transfer functions were evaluated, and its resolution was studied in detail. The resolving power of the instrument in this size range was found to be better than that of the nano-DMA, which is ubiquitously used in this size range. In this chapter, the size range of the instrument is further enhanced (4-40 nm) by using a higher electric field than previously employed and a detector (a condensation particle counter) with a faster response time (enabling the detection of smaller particles as well).

5.1 Introduction

Electrical mobility spectroscopes come in two varieties: First, devices that separate particles of different mobilities into different spatial trajectories, such as the

DMA, described in detail in prior chapters of this thesis.(Knutson and Whitby 1975b, Chen et al. 1998, Fernandez de la Mora and Kozlowski 2013) These are most commonly used in aerosol science to measure particle size-distribution functions above 2 nm in mobility equivalent size.(Jeon et al. 2016, Smith et al. 2010b) Second, instruments that temporally separate particles, i.e., cause particles of different mobilities to arrive at a detector at different times, such as drift tube ion mobility spectrometers.(St. Louis and Hill 1990, Borsdorf and Eiceman 2006) Historically, these have been most commonly used in the detection, separation and analysis of sub-2 nm ions/clusters.(Mäkinen, Nousiainen and Sillanpää 2011, Tam and Hill 2004, Baumbach 2009, Ohshimo et al. 2015, Han and Ruotolo 2015) The physical principle behind the operation of both types of instruments is the same: charged particles are exposed to an electrostatic field gradient in a bath gas and are acted upon by two forces: an electrical force that accelerates the charged particles along electrical field lines and a frictional drag resulting from collisions with the bath gas molecules.(Revercomb and Mason 1975) The balance of the two forces causes the particles to migrate at a uniform terminal velocity, termed the drift speed.(Mason and McDaniel 1988) When the electrical field strength is low, this drift speed is proportional to the electrical field; the proportionality constant is the mobility of the particle. The mobility is a function of the particle structure, the properties of the surrounding gas molecules, and the nature of interactions between them during collisions. It is ultimately the difference in mobility of different particles that causes them to migrate along different trajectories in spatial mobility separators or arrive at different drift

(measurement) times in temporal mobility separators (commonly referred to as drift tubes).

DMAs have been successfully used in the particle-size distribution measurement of aerosols and can be used as sources of mono-mobile particles. While their use is widespread, they suffer from certain limitations that can be overcome by temporal separating drift tubes. First, DMAs lose resolution at smaller sizes. This is because of the way DMAs operate; they have the same mean transit time for particles of all mobilities. The scale for mean displacement of a diffusing particle is proportional to the product of its diffusivity and time, hence, smaller particles (with higher diffusivities) can be measured only with degraded resolution.(Stolzenburg and McMurry 2008, Downard, Dama and Flagan 2011) Ideal drift tubes, on the other hand, have a resolution independent of mobility, as more mobile, more diffusive particles require proportionally less time to traverse the instrument.(Revercomb and Mason 1975) Second, even fast size distribution function measurement techniques (such as SMPS) with DMAs take several seconds for sampling.(Wang and Flagan 1990) State-of-the-art drift tubes complete drift time measurement of ions/clusters in seconds and enabling sampling on sub-second intervals. The longer sampling time for DMAs limits their utility in the measurement of rapidly evolving aerosols, such as those encountered in drone-based atmospheric sampling or as quantitative analyte detectors of the non-volatile residue obtained by nebulization of the effluent in liquid chromatography systems. Third, DMAs require turbomachinery (e.g. blowers) in their operation, which particularly pose difficulties in attaining higher resolutions. This is because achieving high resolution in DMAs is

directly related to maintaining steady, laminar flows at high Reynolds numbers, which is inherently challenging.(Rus et al. 2010a) Unencumbered by this limitation, drift tubes have resolving powers in excess of 100 (Kemper, Dupuis and Bowers 2009, Merenbloom et al. 2009, Davis et al. 2017, Liu et al. 2017) , whereas the peak resolution of the best DMA's are in the range of 50-70(Martinez-Lozano and Fernandez de la Mora 2006, Rus et al. 2010b).

However, the extension of drift tube techniques from the world of molecular clusters to the larger particle size regime of aerosol science is not trivial because of several hurdles. First, cutting-edge drift tubes have drift regions which are several meters in length. Practical use of drift tubes in aerosol size distribution measurements would require optimization of the drift region length. Second, drift tubes used in ion mobility spectrometry operate under low pressures and use complex electrostatic gating to transmit ions to their drift region.(Dugourd et al. 1997) If implemented, this could lead to the alteration of the aerosol under study; most aerosol systems and aerosol detectors (CPCs, for example) are situated at atmospheric pressure (as shown previously in this dissertation, the atmospheric pressure to low pressure transition thermally excites ions/particles, and can lead to dissociation). Third, drift tubes use fast response, lower sensitivity detectors (Faraday plates) to measure ion currents as functions of time. Most aerosol systems have lower concentration than can be sensitively measured by Faraday plates, which necessitates coupling drift tubes with atmospheric pressure detectors such as CPCs. However, the CPCs would still need to be sufficiently fast in responding to particles to ensure efficient synchronization with the fast drift (measurement) times.

Oberreit and co-workers overcame these challenges with a drift tube-CPC combination capable of detecting particles in the size range of 2 to 11 nm.(Oberreit et al. 2014) It had a fluid mechanical gating capable of sampling particles continuously but let them into the drift region only upon application of the measuring electric field gradient. The voltage gradient, drift region length, and operating flows were chosen to be reasonable for measuring size distributions of monodisperse particles in this size range. Further, the detector used was a fast-response TSI water CPC, and the system was capable of measuring particles arriving at sub-second measurement times. Buckley and Hogan measured transmission functions of this drift tube system and characterized its resolving power in detail.(Buckley and Hogan 2017) The measurement of transmission functions and their fitting to parametric skewed Gaussian distributions enables the size distribution measurement of aerosols in this size range using the formal inversion process mentioned in the Introduction chapter. This chapter of this thesis focuses on the extension of the size range of this drift tube system. This is done by employing higher field strengths than before (67% higher) and CPC with a faster response time (around 100 ms).

5.2 Experiments

5.2.1 Instrument Description

A schematic of the drift tube is shown in Figure 5.1. The details of the instrument design and its operation to separate particles in time has been described previously.(Oberreit et al. 2014) A summary of the DT-IMS operating principles is provided for completeness. Frequent references to Figure 5.1 are made in this description.

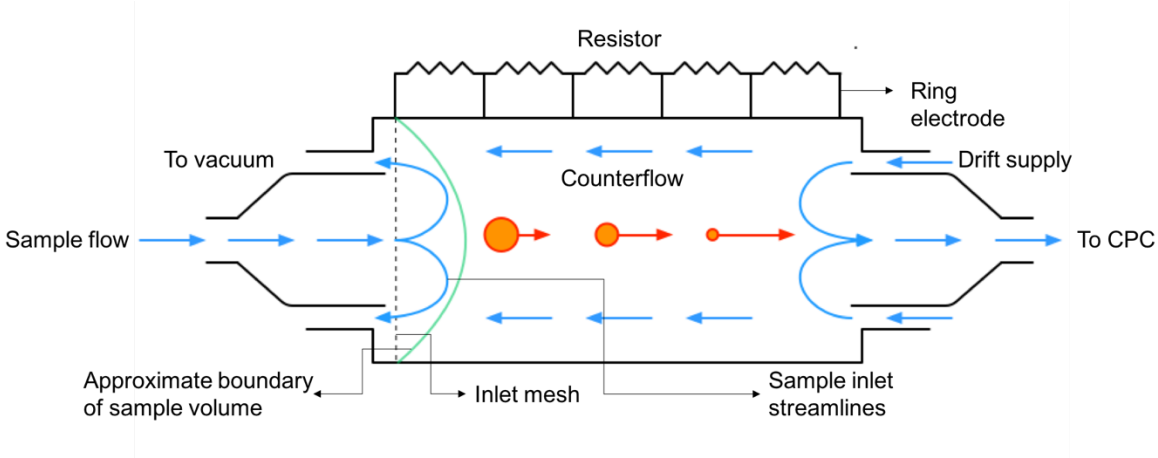

Figure 5.1. Schematic of the drift tube used in this study

The drift tube consists of three sections: the sample inlet region, the drift region, and the outlet region. At all times aerosol is continuously sampled into the sample inlet region. Before measurements start, there is no electric potential gradient in the instrument. Under these conditions, the particles entering the sample inlet region traverse the "sampling volume" and then flow to the "vacuum outlet" via the "sample inlet streamlines" schematized in Figure 5.1. At all times the device is operational, there is also counterflow originating from the "drift supply flow" sent in through the "drift supply inlet", that flows across the drift region and into the sample inlet region. This counterflow and the aerosol flow together are drawn out through the vacuum outlet by a pump. The presence of this counteflow prevents the entry of any particles into the drift region (except by diffusion) and this constitutes the fluid-mechanical gating of the device.

The drift region consists of a plastic tubing with 20 ring electrodes in it separated (from each other) by spacers, as shown in Figure 5.1. The electrodes are connected in series with 10 MOhm resistors between them. A conducting mesh screen is connected to

the first ring electrode (counting from the sample inlet region). As shown, sample inlet streamlines penetrate this mesh into the sample volume and then exit back through the same mesh. When measurements are performed, a voltage is applied to the uppermost (front) electrode and mesh screen, leading to a progressively lower voltage from electrode to electrode, and hence an axial electric field. Prior aerosol drift tube incarnations used voltages of 1 kV, 3 kV, 6 kV, and rarely 9 kV. In the original prototype, voltages larger than this led to corona discharge around the instrument. Modifications in the current version suppress such discharged, and now the first electrode (and the mesh screen) are held at 10 kV while the final electrode is held at ground voltage. As larger electric fields are required to drive the migration of lower mobility (larger) particles, a higher voltage extends the size range over which the drift tube can be applied.

The paths of uncharged particles remain unperturbed by the application of the high voltage; they continue to follow sample inlet streamlines from the aerosol inlet to the excess outlet. As the sample inlet is always at ground potential, particles of opposite polarity to the high voltage applied migrate electrophoretically to the mesh screen and do not enter the drift region. Thus, both neutrals and oppositely charged particles do not enter the drift region when the driving voltage is applied. However, particles of the same polarity as the applied voltage behave differently depending on their relative position with respect to the mesh screen. Those to the left of the mesh screen are repelled away to the sample inlet upon application of the driving electric field, whereas those to the right of the mesh are part of the sample volume. The latter enter the drift region and migrate

towards the outlet region. The fate of the particles entering the drift region depends on their drift velocity. If the drift velocity is higher than the counterflow velocity, the particles make their way to the outlet region (This sets the upper size limit that can be detected by the device). The outlet region is coupled to a fast response CPC. Particles reaching the outlet region can be sampled by the CPC and their time of detection since the application of the voltage can be measured. The time taken to travel the drift region depends on the drift velocity of the particles (which in turn depends on their mobility). Except for particles of the highest mobility, the time of detection is primarily a function of their mobility. The time of detection of highly mobile particles is a complicated function of their drift times (mobility dependent) and the CPC response time (detector dependent). This determines the lower size limit that can be detected by the instrument. The arrival time distribution of monodisperse particles sampled by the instrument is thus dependent on the sample volume (set by the inlet flow, the aerosol sampling flow, the instrument inlet design including the mesh), their drift time through the drift region (counterflow and electric field gradient dependent), and the CPC response function. If monomobile particles are selected using a DMA, the shape of the arrival time distribution will additionally depend on the transfer function of the DMA. The instrument is uniquely (compared to all other drift tube ion mobility spectrometers) capable of sampling charged particles at ground potential and at atmospheric pressure and measuring them with single particle sensitivity.

5.2.2 Measurement Setup

The measurement range of the drift tube is benchmarked by a tandem ion mobility spectrometry measurement technique similar to the ones used previously for the same purpose, but with a prototype limits to 11 nm diameter particles and smaller. (Oberreit et al. 2014). The experimental system consists of the following sections: aerosol generation, mobility classification by differential mobility analysis, mobility measurement and particle detection in the DT-CPC system and is shown schematically in Figure 5.2. The goal of this study is to find drift tube operating conditions which maximize the mobility range of measurement and maximize the resolution of the instrument (as given by the relative full width at half maximum of monomobile particles chosen by a DMA). Aerosol is generated by an evaporation-condensation technique from a length of tungsten wire undergoing resistive heating by a direct electric current. This "glowing wire generator" is similar to the aerosol generation scheme used in the previous chapter for activation efficiency characterization of CPCs and details may be found therein. Briefly, WO_x particles are generated from trace oxygen impurities from the carrier gas of industrial grade nitrogen gas flowed at a rate of 6 L per minute (nominally) through the wire generator chamber.

As repeated several times in this thesis, size measurement requires that the charge distribution on the aerosol be known. This is, as commonly done, achieved by passing the aerosol flow required for differential mobility analysis through a ^{85}Kr charge conditioner, which is a source of electrons by radioactive decay. The excess aerosol flows through a

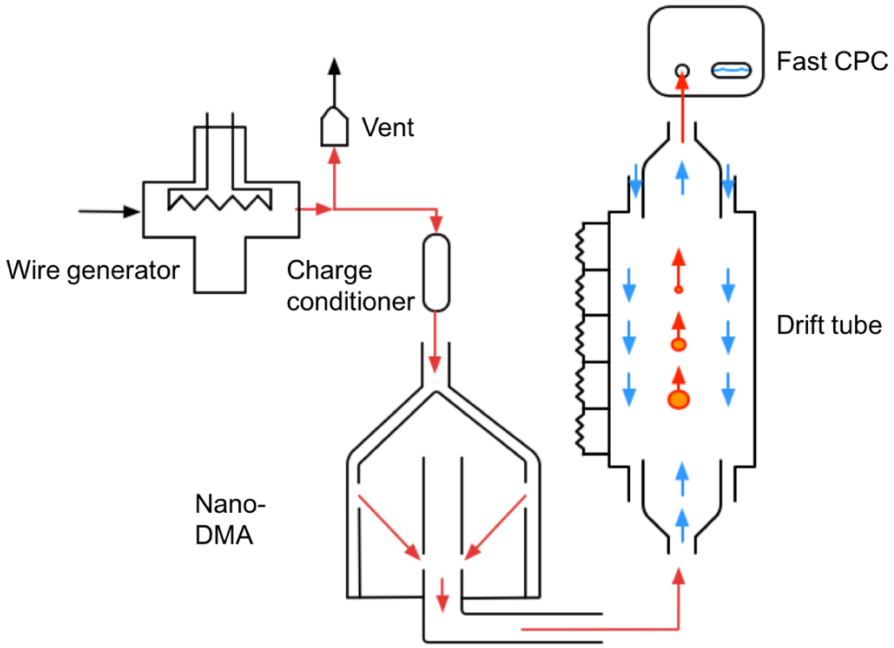

Figure 5.2. Experimental setup for the characterization of drift tube size range

HEPA filter vent into room air. Following collisions with the electrons generated in the charge conditioner, trace organic impurities in the gas phase produce roughly equal concentrations of positive and negative ions. Given sufficient contact time with bipolar ions produced, the particles generated from the aerosol source acquire the well-characterized bipolar steady state charge distribution. In this case, the fraction of particles that are neutral, singly charged, doubly charged, etc. are known as a function of particle size. For the selected operating conditions of the drift tube-CPC system, the aerosol sampling flow (and consequently, the flow through the charger) is 360 mL/min.

Differential mobility analysis is achieved by a TSI 3085 nano-DMA. The DMA is operated under recirculating mode with a sheath flow rate of 10 L per minute. Positive particles were chosen by applying a negative high voltage (wrt ground) on the inner

cylindrical electrode. Particles corresponding to the mobilities of (singly charged) 4 nm, 5 nm, 7 nm, 10 nm, 12 nm, 15 nm, 20 nm, 25 nm, 30 nm, and 40 nm particles were selected in turn by applying the appropriate voltage on the DMA inner electrode. The particles of selected mobility from the DMA monomobile outlet were then sampled by the DT-CPC system at a nitrogen gas flow rate of 360 mL/min. The CPC was operated in the 1.45 L/min flow mode and this became the outlet flow of the drift tube. The final operating counterflow of the drift tube chosen was 225 mL/min. Hence, the drift supply was 1.225 mL/min and the inlet flow aspirated by the DT pump was 585 mL/min. To measure arrival time distributions of mobility-selected particles, a voltage of 10 kV was applied at the first (from the sample inlet) electrode, while the last electrode was held at ground potential. Caution was also taken to maintain the fittings in the sample inlet at ground potential as well, which is required for the proper operation of the drift tube. Several cycles of high voltage application and turning off were performed. Each cycle consisted of pause times (between high voltage applications, to clear the particles which had not arrived at the CPC from the drift and outlet regions) between 10-30 s, depending on the mobility of the particles under study and drift times (this constituted the measurement time from the time the high voltage was switched on) in the range of 10 to 60 s. At least, 5 cycles of measurements were performed and the resulting scans were averaged to obtain the final arrival time distribution for each DMA-selected mobility.

The drift supply and inlet flow rates of the drift tube were varied in measurements. The CPC flow rate was a constant, hence changing the drift supply flow rate sets the counter flow. Changing the inlet flow changed the aerosol sampling flow

drawn by the drift tube (Of the four operating flows of the drift tube, only three are independent. The other is set by a mass balance between the four flows). Arrival time distributions were measured in the 4-40 nm size range at the mobilities mentioned above. The final operating conditions were chosen based on the following criteria:

1. Maximization of the size-range of (assuming singly charged) particles capable of being transmitted and measured by the drift tube. Any chosen operating condition has an upper limit determined by the counterflow. Particles with electrophoretic speeds greater than the counterflow may reach the detector at the end of the drift region, while those with drift speeds less than the counterflow fail to be detected by the CPC at any appreciable probability (only diffusion can lead to their detection). The minimum is set by particles reaching the detector so soon that it is not able to respond to changes in particle concentration and deliver reliable arrival time distributions.

2. Maximization of resolution of the arrival time distribution of mobility selected particles given by the relative width of the distribution at half its maximum value. DT-CPC conditions that lead to broadening of this resolution include, as mentioned in the *Instrument Description* section, the size of the sample volume (determined by instrument flows and the mesh screen), and the time taken by the particles to reach the detector (function of their electrophoretic speed and counterflow gas speed).

5.3. Results & Discussion

The normalized arrival time distributions of particles of nano-DMA selected mobilities are displayed in Figure 5.3. These were obtained for the optimized operating flows chosen, which a CPC flow rate of 1450 ml/min, a drift supply flow of 1625 ml/min, and a inlet flow rate of 585 ml/min (leading 360 ml/min of aerosol sampled into the device). The legend shows the size corresponding to the DMA chosen mobility, assuming singly charged particles. In line with previous characterization of this drift tube system, the asymmetry of the arrival time distributions increases with increasing peak drift time. This is expected for lower mobilities (i.e. larger particles) as they acquire lower drift speeds. The sampling of particles traveling at lower electrophoretic speeds (approaching the counter flow gas speed) in a drift tube with non-plug flow (i.e. there is variation in the gas speed with radial location) is expected to lead to this asymmetry. The same non-ideality leads to non-linearity in the peak drift time v. inverse mobility plot (Figure 5.4) at higher inverse mobilities. These particles only traverse the drift tube if they are farther down the tube at the beginning of the measurement, hence they derive from a spatially distinct sample volume and traverse a shorter distance. Linearity between the two quantities is expected for linear ion mobility spectrometry (which is achieved when the ratio of electric field to gas molecule number concentration is sufficiently low, such as in this instrument). The lack of non-linearities in the low inverse mobility region implies a negligible effect of the CPC response time on the measured drift times.

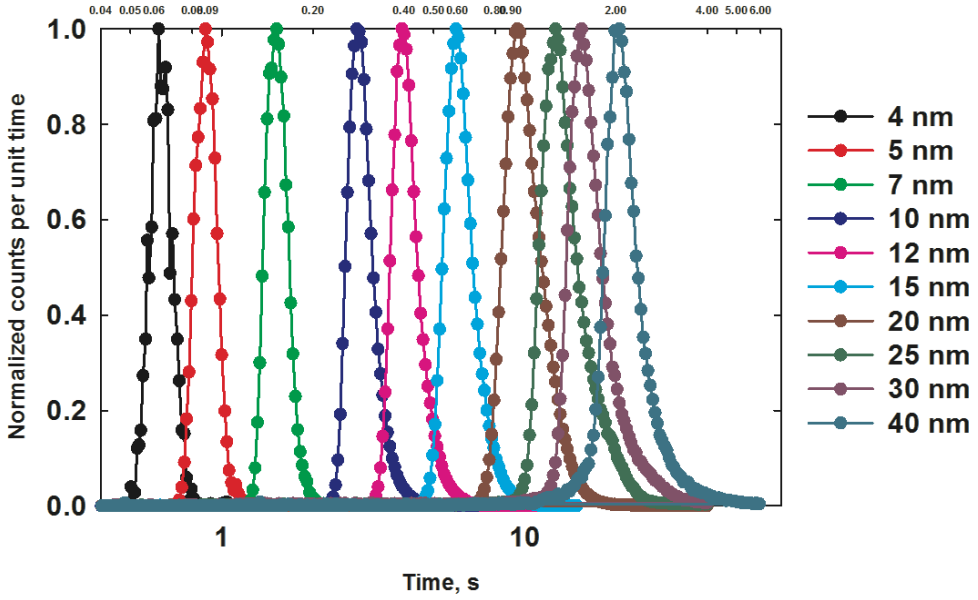

Figure 5.3. Normalized arrival time distributions of particles of selected mobilities.

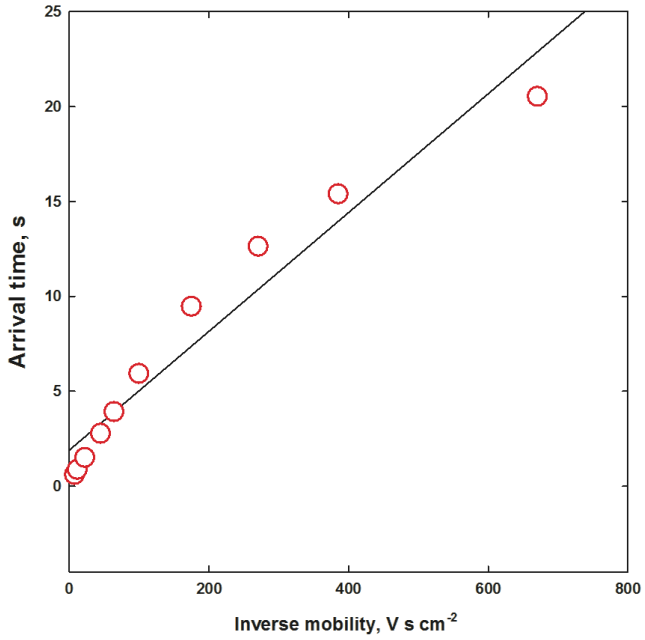

Figure 5.4. Variation of peak arrival time with inverse mobility. Non-linearity appears to be an influence of shrinking and moving sample volume for larger particles.

To investigate the resolving abilities of the DT-CPC system, the two plots in Figure 5.5 are displayed. Figure 5.5a shows the variation of the normalized full-width at half peak maximum (FWHM, normalized w.r.t. peak arrival time) of the arrival time distributions against the peak arrival time. This normalized FWHM can be seen as the summation of variances from different independent processes leading to peak broadening: the finite width of the DMA transfer function encountered during DMA selection, the broadening resulting from the spread of particles within the sampling volume region, diffusion broadening during drift through the measurement region of the device (captured by a time resulting from the combination of drift speed and counterflow speed). The latter two contribute to the resolution of the drift tube. The first contribution can be estimated from a simple analysis of the DMA transfer function. Figure 5.5b shows a ratio of the arrival time distribution inferred normalized FWHM to that of the normalized FWHM of the nano-DMA transfer function in inverse mobility space. (Stolzenburg & McMurry, 2008) In nearly all cases (except low drift tubes), the ratio of observed FWHM to that for the nano-DMA alone is greater than 2.0, suggesting that the resolving power of the drift tube under these modified conditions is below that of the nano-DMA (which has a resolving power in the 7-10). Therefore, the modified system is a low-resolution instrument. Nonetheless, it enables extremely rapid size measurements of particles without temporal signal smearing that is associated with DMAs.

5.4 Conclusion

The measurement range of the atmospheric pressure aerosol drift tube has been extended up to 40 nm from the previous 11 nm, using a combination of higher electric fields to drive the particle electrophoretically, as well as a fast response CPC to detect highly mobile particles at the lower end of the size range (in this work, this is 4 nm). While the measurement time shows the expected linear response to inverse mobility in the low to intermediate range of inverse mobility, deviations from linearity are observed at large inverse mobilities. The use of these operating parameters in the size distribution measurement of aerosols will require the measurement of the transmission functions (the drift tube equivalent of transfer functions) in the size range studied here.

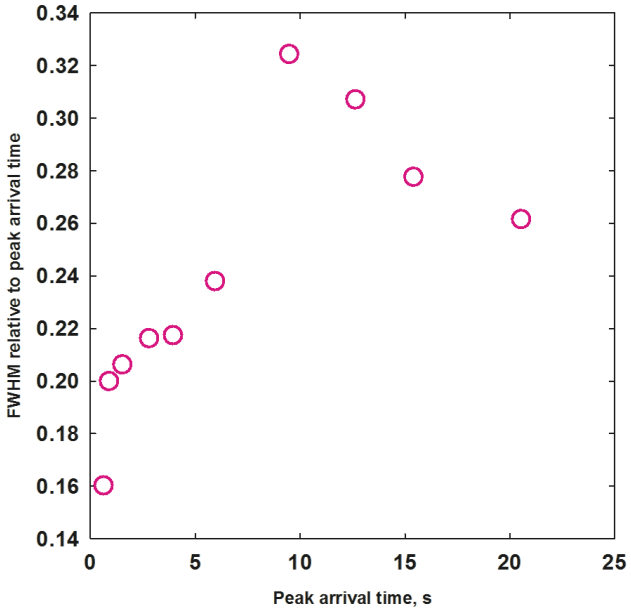

(a)

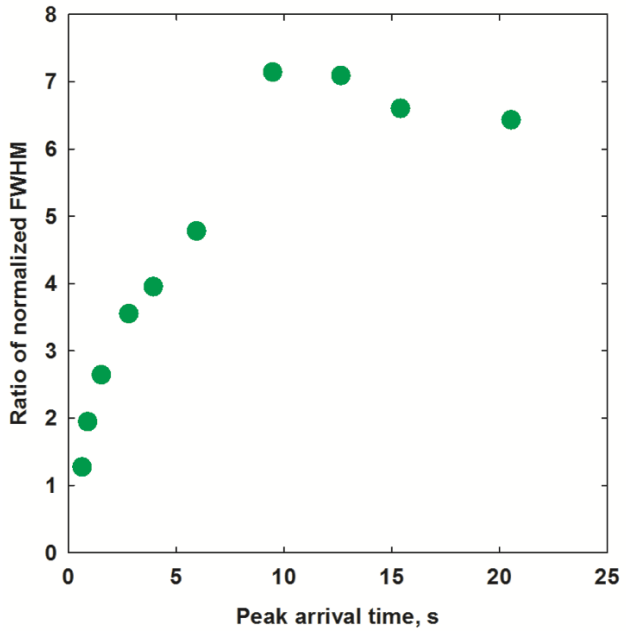

(b)

Figure 5.5. (a) Normalized FWHM of drift tube arrival time distributions **(b)** Ratio of normalized FWHM of drift tube ATD to that of the nano-DMA transfer function

Chapter 6: Conclusions

The studies performed in this thesis sought to further understanding in several areas of aerosol measurement science, which particularly relevant to aerosol size and structural characterization. Collectively, these studies lead to the following conclusions:

First, as far as the charging step is concerned, 31 ions specifically generated from trace vapor impurities in the carrier gas were identified. These impurities largely originate from the polymers used in system components, contrary to previous assumptions that ions arise from bath gas molecules, these impurities are almost always in high enough concentration to account for all ions produce in commonly used bipolar chargers. It is highly that such ions are present in most aerosol measurement systems and in systems where ionizers are generally in ambient air (e.g. smoke detectors). Also in contrast with the assumptions of previous studies, no universal mass-mobility relationship is observed for these ions. Calculation of the electrical mobilities of these ions from structural models reveal that gas molecule collisions are largely diffuse and inelastic with most of the identified species, with the exception the planar where specular and elastic collisions seem to dominate. Additionally, it is shown that the steady state charge distribution is a weak function of the specific ion population, the empirically observed skew towards negative particles can be explained by the predominance of the nitrate ion in the ion population. Despite the differences between the measured ion population and prior assumptions, available regression models of the steady state charge distribution are shown to largely capture the charge state distribution predicted from the

identified ion population. Recent studies have explored improvements to the charge distribution used in mobility-based size distribution measurement. These involve inversion of the size distribution from measurement of both positive and negative particles using SMPS.(Chen, McMurry and Jiang 2018) While such efforts represent progress in charge distribution prediction along the lines suggestion from our work on ion population characterization, in this recent study the underlying charge distribution is computed using collision rate coefficients derived from the Fuchs limiting sphere approach(Fuchs 1963b) with only one type of ion assumed per polarity whose properties are given by the Kilpatrick regression.(Kilpatrick 1971) This theory has limitations along with the noted limitations of assuming one ion type being present.

Second, coupled high resolution DMA- MS studies have augmented the understanding of the stability and hydration of atmospherically relevant sulfuric acid-dimethylamine ions. It is shown for the first time that these ions substantially fragment in typically used mass spectrometer inlets. Pioneering measurements of the extents of hydration by chemically identified cluster ions were performed and positive correlation of water uptake by clusters with excess acid molecules was demonstrated. The degree of water uptake was modest, implying the hydrated clusters could only be viewed as having adsorbed a few molecules of water, and not as droplets. Investigation into the mass and bulk density inferred size of cluster ions showed that these were reasonably close to the electrical mobility inferred sizes. Further, mobility calculations reveal that gas molecule collisions with the sulfur dominated clusters were more elastic and specular as compared to organic ions without sulfur present (i.e. without heavier atoms). Overall, this study

showed that the cluster ion population distribution measured in a mass spectrometer can be influence by fragmentation in the mass spectrometer inlet, and that the extent of fragmentation can be affected by the relative humidity. Since the completion and publication of this study, research focusing on the computation of fragmentation probabilities of sulfuric acid cluster ions combined with experimental validation thereof has started to appear in the literature and in conferences. Also, the measurement of extents of hydration of iodic acid based cluster ions, which are relevant to new particle formation in coastal environments(Sipilä et al. 2016), have been undertaken in the Hogan group.

Third, an alternative technique to modulate activation efficiency curves of a CPC was demonstrated, both empirically and numerically, which was based on directly augmenting the relative rate of heat transfer to mass transfer in the operational region of the CPC. The limits of this approach were probed; it was found that a helium mole fraction of 0.20 to 0.40 was ideal for activation efficiency improvements and at higher mole fractions, the activation efficiency actually decreased. It was also demonstrated that this approach to activation efficiency tuning is generally applicable to working fluids heavier than the gases used for modulation. The natural limit of this approach would be operating in 100% helium. Maisser and coworkers measured sub-1 nm silver atom clusters generated by spark discharge in helium gas using a CPC 3025A. This CPC has a cut-off diameter of 2.5 nm in air. Operating in helium thus decreased the cut-off diameter of the instrument. Further, they had to reduce the temperature window of operation from the default instrument values because the use of helium increased the saturation values to

such high levels with the default operating temperatures that there would be significant homogeneous nucleation of the working fluid. This mode of controlling the saturation ratio in the growth tube could be used to be probe heterogeneous nucleation further. Experiments would involve measurement of nucleation probabilities (inferred from the activation efficiency of monodisperse particles) as a function of the simulation inferred saturation values of the working fluid vapor. The saturation ratio would be computed by numerical simulations and the critical saturation ratio needed for activation would be inferred by matching the flux ratio corresponding to the activation efficiency. This approach would provide a convenient alternative for the characterization of particle/ion against the saturation ratio it would need to be activated to grow.

Finally, the size measurement range of an atmospheric pressure drift tube system with single particle sensitivity was extended to 4-40 nm from 2 to 11 nm in the past. This was accomplished by using higher particle-driving electric fields and fast CPC with sub-second response time. This measurement system can be used in the characterization of nucleation mode particles in atmospheric new particle formation studies (fast evolving sources such as those based on mobile sampling) and as a detector in quantification of a non-volatile analytes after liquid chromatography (after fast nebulization to convert the liquid phase analyte to aerosol). Together with lowering the CPC cut-off by addition of helium gas to modulate its activation efficiency, this system's range can be extended to sub-2nm ions.

References

Adachi, M., Y. Kousaka & K. Okuyama (1985) Unipolar and bipolar diffusion charging of ultrafine aerosol particles. *Journal of Aerosol Science,* 16**,** 109-123.

Agarwal, J. K. & G. J. Sem (1980) Continuous flow, single-particle-counting condensation nucleus counter. *Journal of Aerosol Science,* 11**,** 343-357.

Almeida, J., S. Schobesberger, A. Kurten, I. K. Ortega, O. Kupiainen-Maatta, A. P. Praplan, A. Adamov, A. Amorim, F. Bianchi, M. Breitenlechner, A. David, J. Dommen, N. M. Donahue, A. Downard, E. Dunne, J. Duplissy, S. Ehrhart, R. C. Flagan, A. Franchin, R. Guida, J. Hakala, A. Hansel, M. Heinritzi, H. Henschel, T. Jokinen, H. Junninen, M. Kajos, J. Kangasluoma, H. Keskinen, A. Kupc, T. Kurten, A. N. Kvashin, A. Laaksonen, K. Lehtipalo, M. Leiminger, J. Leppa, V. Loukonen, V. Makhmutov, S. Mathot, M. J. McGrath, T. Nieminen, T. Olenius, A. Onnela, T. Petaja, F. Riccobono, I. Riipinen, M. Rissanen, L. Rondo, T. Ruuskanen, F. D. Santos, N. Sarnela, S. Schallhart, R. Schnitzhofer, J. H. Seinfeld, M. Simon, M. Sipila, Y. Stozhkov, F. Stratmann, A. Tome, J. Trostl, G. Tsagkogeorgas, P. Vaattovaara, Y. Viisanen, A. Virtanen, A. Vrtala, P. E. Wagner, E. Weingartner, H. Wex, C. Williamson, D. Wimmer, P. L. Ye, T. Yli-Juuti, K. S. Carslaw, M. Kulmala, J. Curtius, U. Baltensperger, D. R. Worsnop, H. Vehkamaki & J. Kirkby (2013) Molecular understanding of sulphuric acid-amine particle nucleation in the atmosphere. *Nature,* 502**,** 359-363.

Alonso, M. & F. J. Alguacil (2003) The effect of ion and particle losses in a diffusion charger on reaching a stationary charge distribution. *Journal of Aerosol Science,* 34**,** 1647-1664.

Baumbach, J. I. (2009) Ion mobility spectrometry coupled with multi-capillary columns for metabolic profiling of human breath. *Journal of Breath Research,* 3.

Ballistreri, A., D. Garozzo & G. Montaudo (1984) Mass spectral characterization and thermal decomposition mechanism of poly (dimethylsiloxane). *Macromolecules,* 17**,** 1312-1315.

Barmpounis, K., A. Ranjithkumar, A. Schmidt-Ott, M. Attoui & G. Biskos (2018) Enhancing the detection efficiency of condensation particle counters for sub-2nm particles. *Journal of Aerosol Science,* 117**,** 44-53.

Bianchi, F., A. P. Praplan, N. Sarnela, J. Dommen, A. Kurten, I. K. Ortega, S. Schobesberger, H. Junninen, M. Simon, J. Trostl, T. Jokinen, M. Sipila, A. Adamov, A. Amorim, J. Almeida, M. Breitenlechner, J. Duplissy, S. Ehrhart, R. C. Flagan, A. Franchin, J. Hakala, A. Hansel, M. Heinritzi, J. Kangasluoma, H. Keskinen, J. Kim, J. Kirkby, A. Laaksonen, M. J. Lawler, K. Lehtipalo, M. Leiminger, V. Makhmutov, S. Mathot, A. Onnela, T. Petaja, F. Riccobono, M. P. Rissanen, L. Rondo, A. Tome, A. Virtanen, Y. Viisanen, C. Williamson, D. Wimmer, P. M. Winkler, P. L. Ye, J. Curtius, M. Kulmala, D. R. Worsnop, N. M. Donahue & U. Baltensperger (2014) Insight into Acid-Base Nucleation Experiments by Comparison of the Chemical Composition of Positive, Negative, and Neutral Clusters. *Environmental Science & Technology,* 48**,** 13675-13684.

Bianchi, F., J. Tröstl, H. Junninen, C. Frege, S. Henne, C. R. Hoyle, U. Molteni, E. Herrmann, A. Adamov, N. Bukowiecki, X. Chen, J. Duplissy, M. Gysel, M. Hutterli, J. Kangasluoma, J. Kontkanen, A. Kürten, H. E. Manninen, S. Münch, O. Peräkylä, T. Petäjä, L. Rondo, C. Williamson, E. Weingartner, J. Curtius, D. R. Worsnop, M. Kulmala, J. Dommen & U. Baltensperger (2016) New particle formation in the free troposphere: A question of chemistry and timing. *Science,* 352**,** 1109-12.

Borsdorf, H. & G. A. Eiceman (2006) Ion mobility spectrometry: Principles and applications. *Applied Spectroscopy Reviews,* 41**,** 323-375.

Bricard, J., P. Delattre, G. Madelaine & P. M. 1976. Detection of Ultra-Fine Particles by Means of a Continuous Flux Condensation Nuclei Counter. In *Fine Particles,* ed. B. Y. H. Liu. Academic Press, New York.

Brouwer, D. H., J. H. J. Gijsbers & M. W. M. Lurvink (2004) Personal Exposure to Ultrafine Particles in the Workplace: Exploring Sampling Techniques and Strategies. *The Annals of Occupational Hygiene,* 48**,** 439-453.

Buckley, D. T. & C. J. Hogan (2017) Determination of the transfer function of an atmospheric pressure drift tube ion mobility spectrometer for nanoparticle measurements. *Analyst,* 142**,** 1800-1812.

Burtscher, H., L. Scherrer, H. Siegmann, A. Schmidt-Ott & B. Federer (1982) Probing aerosols by photoelectric charging. *Journal of Applied Physics,* 53**,** 3787-3791.

Bush, M. F., R. J. Saykally & E. R. Williams (2006) Formation of hydrated triply charged metal ions from aqueous solutions using nanodrop mass spectrometry. *International Journal of Mass Spectrometry,* 253**,** 256-262.

Bzdek, B. R., J. W. DePalma, D. P. Ridge, J. Laskin & M. V. Johnston (2013) Fragmentation Energetics of Clusters Relevant to Atmospheric New Particle Formation. *Journal of the American Chemical Society,* 135**,** 3276-3285.

Bzdek, B. R., D. P. Ridge & M. V. Johnston (2011) Amine reactivity with charged sulfuric acid clusters. *Atmospheric Chemistry and Physics,* 11**,** 8735-8743.

Chapman, S. & T. G. Cowling. 1970. *The mathematical theory of non-uniform gases: an account of the kinetic theory of viscosity, thermal conduction and diffusion in gases*. Cambridge university press.

Chase, M. W. (1998) NIST-JANAF Thermochemical Tables. *Journal of Physical and Chemical Reference Data,* 27**,** I-II.

Chen, D. R., D. Y. H. Pui, D. Hummes, H. Fissan, F. R. Quant & G. J. Sem (1998) Design and evaluation of a nanometer aerosol differential mobility analyzer (Nano-DMA). *Journal of Aerosol Science,* 29**,** 497-509.

Chen, M., M. Titcombe, J. K. Jiang, C. Jen, C. A. Kuang, M. L. Fischer, F. L. Eisele, J. I. Siepmann, D. R. Hanson, J. Zhao & P. H. McMurry (2012) Acid-base chemical reaction model for nucleation rates in the polluted atmospheric boundary layer. *Proceedings of the National Academy of Sciences of the United States of America,* 109**,** 18713-18718.

Chen, X., P. H. McMurry & J. Jiang (2018) Stationary characteristics in bipolar diffusion charging of aerosols: improving the performance of electrical mobility size spectrometers. *Aerosol Science and Technology*, 1-13.

Cloupeau, M. & B. Prunet-Foch (1989) Electrostatic Spraying of Liquids in Cone-Jet Mode. *Journal of Electrostatics,* 22, 135-159.

Collings, N., K. Rongchai & J. P. R. Symonds (2014) A condensation particle counter insensitive to volatile particles. *Journal of Aerosol Science,* 73, 27-38.

Davis, A. L., W. Liu, W. F. Siems & B. H. Clowers (2017) Correlation ion mobility spectrometry. *Analyst*, 10.1039/C6AN02249A.

Davies, C. N. (1945) Definitive equations for the fluid resistance of spheres. *Proceedings of the Physical Society,* 57, 259-270.

de La Verpilliere, J. L., J. J. Swanson & A. M. Boies (2015) Unsteady bipolar diffusion charging in aerosol neutralisers: A non-dimensional approach to predict charge distribution equilibrium behaviour. *Journal of Aerosol Science,* 86, 55-68.

DePalma, J. W., B. R. Bzdek, D. J. Doren & M. V. Johnston (2012) Structure and Energetics of Nanometer Size Clusters of Sulfuric Acid with Ammonia and Dimethylamine. *Journal of Physical Chemistry A,* 116, 1030-1040.

DePalma, J. W., D. J. Doren & M. V. Johnston (2014) Formation and Growth of Molecular Clusters Containing Sulfuric Acid, Water, Ammonia, and Dimethylamine. *Journal of Physical Chemistry A,* 118, 5464-5473.

Dewar, M. J., E. G. Zoebisch, E. F. Healy & J. J. Stewart (1985) Development and use of quantum mechanical molecular models. 76. AM1: a new general purpose quantum mechanical molecular model. *Journal of the American Chemical Society,* 107, 3902-3909.

Downard, A. J., J. F. Dama & R. C. Flagan (2011) An Asymptotic Analysis of Differential Electrical Mobility Classifiers. *Aerosol Science and Technology,* 45, 727-739.

Dugourd, P., R. R. Hudgins, D. E. Clemmer & M. F. Jarrold (1997) High-resolution ion mobility measurements. *Review of Scientific Instruments,* 68, 1122-1129.

Ensor, D., R. Donovan & B. Locke (1987) Particle Size Distributions in Clean Rooms. *The Journal of Environmental Sciences,* 30, 44-49.

Epstein, P. S. (1924) On the Resistance Experienced by Spheres in their Motion through Gases. *Physical Review,* 23, 710-733.

Eucken, A. (1913) Über das Wärmeleitvermögen, die spezifische Wärme und die innere Reibung der Gase. *Physik. Z,* 14, 324-332.

Exner, O. & S. Böhm (2005) Acidities of Nitrous and Nitric Acids. *European Journal of Inorganic Chemistry,* 2005, 1747-1750.

Fang, J. X., Y. Wang, M. Attoui, T. S. Chadha, J. R. Ray, W.-N. Wang, Y.-S. Jun & P. Biswas (2014) Measurement of Sub-2 nm Clusters of Pristine and Composite Metal Oxides during Nanomaterial Synthesis in Flame Aerosol Reactors. *Analytical Chemistry,* 86, 7523-7529.

Fenn, J. B. (2000) Mass spectrometric implications of high-pressure ion sources. *International Journal of Mass Spectrometry,* 200, 459-478.

Fernandez de la Mora, J., L. de Juan, T. Eichler & J. Rosell (1998) Differential mobility analysis of molecular ions and nanometer particles. *Trac-Trends in Analytical Chemistry,* 17**,** 328-339.

Fernandez de la Mora, J. & J. Kozlowski (2013) Hand-held differential mobility analyzers of high resolution for 1-30 nm particles: Design and fabrication considerations. *Journal of Aerosol Science,* 57**,** 45-53.

Fernandez de la Mora, J., B. A. Thomson & M. Gamero-Castano (2005) Tandem mobility mass spectrometry study of electrosprayed tetraheptyl ammonium bromide clusters. *Journal of the American Society for Mass Spectrometry,* 16**,** 717-732.

Fernández-García, J. & J. Fernández de la Mora (2013) Measuring the Effect of Ion-Induced Drift-Gas Polarization on the Electrical Mobilities of Multiply-Charged Ionic Liquid Nanodrops in Air. *Journal of the American Society for Mass Spectrometry,* 24**,** 1872-1889.

--- (2014) Electrical mobilities of multiply charged ionic-liquid nanodrops in air and carbon dioxide over a wide temperature range: influence of ion-induced dipole interactions. *Physical Chemistry Chemical Physics,* 16**,** 20500-20513.

Fisenko, S. P., W.-N. Wang, M. Shimada & K. Okuyama (2007) Vapor condensation on nanoparticles in the mixer of a particle size magnifier. *International Journal of Heat and Mass Transfer,* 50**,** 2333-2338.

Fuchs, N. A. 1959. *Evaporation and Droplet Growth in Gaseous Media*. Pergamon Press, London.

Fuchs, N. A. (1963) On the Stationary Charge Distribution on Aerosol Particles in a Bipolar Ionic Atmosphere. *Geofis. Pura Appl.,* 51**,** 185-193.

Fuchs, N. A. & A. G. Sutugin (1965) Coagulation Rate of Highly Dispersed Aerosols. *Journal of Colloid Science,* 20**,** 492-500.

Gamero-Castano, M. & J. Fernandez de la Mora (2000a) A condensation nucleus counter (CNC) sensitive to singly charged sub-nanometer particles. *Journal of Aerosol Science,* 31**,** 757-772.

--- (2000b) Mechanisms of electrospray ionization of singly and multiply charged salt clusters. *Analytica Chimica Acta,* 406**,** 67-91.

--- (2000c) Modulations in the abundance of salt clusters in electrosprays. *Analytical Chemistry,* 72**,** 1426-1429.

Gopalakrishnan, R., P. H. McMurry & C. J. Hogan (2015) Bipolar Charging of Nanoparticles: A Review of Existing and Development of New Analysis Approaches. *Aerosol Science and Technology,* In Review.

Gopalakrishnan, R., M. J. Meredith, C. Larriba-Andaluz & C. J. Hogan (2013) Brownian dynamics determination of the bipolar steady state charge distribution on spheres and non-spheres in the transition regime. *Journal of Aerosol Science,* 63**,** 126-145.

Gopalakrishnan, R. & C. J. Hogan (2012) Coulomb-influenced collisions in aerosols and dusty plasmas. *Physical Review E,* 85**,** 026410.

Greenspan, L. (1977) Humidity fixed points of binary saturated aqueous solutions. *Journal of Research, National Bureau of Standards (US), Series A, Physics and Chemistry,* 81**,** 89-96.

Gross, J. 2004. *Mass Spectrometry: A Textbook*. Berlin Heidelberg: Springer-Verlag.

Han, L. & B. T. Ruotolo (2015) Ion Mobility-Mass Spectrometry Differentiates Protein Quaternary Structures Formed in Solution and in Electrospray Droplets. *Analytical Chemistry,* 87**,** 6808-6813.

Hering, S. V., G. S. Lewis, S. R. Spielman, A. Eiguren-Fernandez, N. M. Kreisberg, C. Kuang & M. Attoui (2017) Detection near 1-nm with a laminar-flow, water-based condensation particle counter. *Aerosol Science and Technology,* 51**,** 354-362.

Hering, S. V. & M. R. Stolzenburg (2005) A method for particle size amplification by water condensation in a laminar, thermally diffusive flow. *Aerosol Science and Technology,* 39**,** 428-436.

Hering, S. V., M. R. Stolzenburg, F. R. Quant, D. R. Oberreit & P. B. Keady (2005) A laminar-flow, water-based condensation particle counter (WCPC). *Aerosol Science and Technology,* 39**,** 659-672.

Higashi, H., T. Tokumi, C. J. Hogan, H. Suda, T. Seto & Y. Otani (2015) Simultaneous ion and neutral evaporation in aqueous nanodrops: experiment, theory, and molecular dynamics simulations. *Physical Chemistry Chemical Physics,* 17**,** 15746-15755.

Hogan, C. J. & J. Fernandez de la Mora (2009) Tandem ion mobility-mass spectrometry (IMS-MS) study of ion evaporation from ionic liquid-acetonitrile nanodrops. *Physical Chemistry Chemical Physics,* 11**,** 8079-8090.

--- (2010) Ion-Pair Evaporation from Ionic Liquid Clusters. *Journal of the American Society for Mass Spectrometry,* 21**,** 1382-1386.

Hogan, C. J. & J. F. de la Mora (2011) Ion mobility measurements of nondenatured 12–150 kDa proteins and protein multimers by Tandem Differential Mobility Analysis–Mass Spectrometry (DMA-MS). *Journal of the American Society for Mass Spectrometry,* 22**,** 158-172.

Holton, P. M. & K. Willeke (1987) The Effect of Aerosol Size Distribution and Measurement Method on Respirator Fit. *American Industrial Hygiene Association Journal,* 48**,** 855-860.

Hoppel, W. A. & G. M. Frick (1986) Ion—aerosol attachment coefficients and the steady-state charge distribution on aerosols in a bipolar ion environment. *Aerosol Science and Technology,* 5**,** 1-21.

Hoppel, W. A. & G. M. Frick (1990) The Nonequilibrium Character of the Aerosol Charge-Distributions Produced by Neutralizers. *Aerosol Science and Technology,* 12**,** 471-496.

Iida, K., M. R. Stolzenburg & P. H. McMurry (2009) Effect of Working Fluid on Sub-2 nm Particle Detection with a Laminar Flow Ultrafine Condensation Particle Counter. *Aerosol Science and Technology,* 43**,** 81-96.

Iida, K., M. R. Stolzenburg, P. H. McMurry, J. N. Smith, F. R. Quant, D. R. Oberreit, P. B. Keady, A. Eiguren-Fernandez, G. S. Lewis, N. M. Kreisberg & S. V. Hering

(2008) An ultrafine, water-based condensation particle counter and its evaluation under field conditions. *Aerosol Science and Technology,* 42**,** 862-871.

Jecklin, M. C., G. Gamez & R. Zenobi (2009) Fast polymer fingerprinting using flowing afterglow atmospheric pressure glow discharge mass spectrometry. *Analyst,* 134**,** 1629-1636.

Jen, C. N., D. R. Hanson & P. H. McMurry (2014a) Toward Reconciling Measurements of Atmospherically Relevant Clusters by Chemical Ionization Mass Spectrometry and Mobility Classification/Vapor Condensation. *Aerosol Science and Technology,* 49**,** i-iii.

Jen, C. N., P. H. McMurry & D. R. Hanson (2014b) Stabilization of sulfuric acid dimers by ammonia, methylamine, dimethylamine, and trimethylamine. *Journal of Geophysical Research-Atmospheres,* 119**,** 7502-7514.

Jeon, S., D. R. Oberreit, G. Van Schooneveld, Z. Gao, J. C. Bischof, C. L. Haynes & C. J. Hogan (2016) Ion-Mobility-Based Quantification of Surface-Coating-Dependent Binding of Serum Albumin to Superparamagnetic Iron Oxide Nanoparticles. *ACS Applied Materials & Interfaces,* 8**,** 24482-24490.

Jiang, J., M. Chen, C. Kuang, M. Attoui & P. H. McMurry (2011a) Electrical Mobility Spectrometer Using a Diethylene Glycol Condensation Particle Counter for Measurement of Aerosol Size Distributions Down to 1 nm. *Aerosol Science and Technology,* 45**,** 510-521.

Jiang, J., J. Zhao, M. Chen, F. Eisele, J. H. Scheckman, B. J. Williams, C. Kuang & P. H. McMurry (2011b) First Measurements of Neutral Atmospheric Cluster and 1-2 nm Particle Number Size Distributions During Nucleation Events. *Aerosol Science and Technology,* 45**,** ii-v.

Jiang, J. K., M. Attoui, M. Heim, N. A. Brunelli, P. H. McMurry, G. Kasper, R. C. Flagan, K. Giapis & G. Mouret (2011c) Transfer Functions and Penetrations of Five Differential Mobility Analyzers for Sub-2 nm Particle Classification. *Aerosol Science and Technology,* 45**,** 480-492.

Jiang, J., C. Kim, X. Wang, M. R. Stolzenburg, S. L. Kaufman, C. Qi, G. J. Sem, H. Sakurai, N. Hama & P. H. McMurry (2014) Aerosol Charge Fractions Downstream of Six Bipolar Chargers: Effects of Ion Source, Source Activity, and Flowrate. *Aerosol Science and Technology,* 48**,** 1207-1216.

Johnson, C. J. & M. A. Johnson (2013) Vibrational Spectra and Fragmentation Pathways of Size-Selected, D-2-Tagged Ammonium/Methylammonium Bisulfate Clusters. *Journal of Physical Chemistry A,* 117**,** 13265-13274.

Kanu, A. B., P. Dwivedi, M. Tam, L. Matz & H. H. Hill (2008) Ion mobility-mass spectrometry. *Journal of Mass Spectrometry,* 43**,** 1-22.

Keller, B. O., J. Sui, A. B. Young & R. M. Whittal (2008) Interferences and contaminants encountered in modern mass spectrometry. *Analytica Chimica Acta,* 627**,** 71-81.

Kemme, H. R. & S. I. Kreps (1969) Vapor pressure of primary n-alkyl chlorides and alcohols. *Journal of Chemical and Engineering Data,* 14**,** 98-102.

Kemper, P. R., N. F. Dupuis & M. T. Bowers (2009) A new, higher resolution, ion mobility mass spectrometer. *International Journal of Mass Spectrometry,* 287**,** 46-57.

Khan, W. A. & I. Pop (2010) Boundary-layer flow of a nanofluid past a stretching sheet. *International Journal of Heat and Mass Transfer,* 53**,** 2477-2483.

Kilpatrick, W. D. 1971. An experimental mass-mobility relation for ions in air at atmospheric pressure. In *Proceedings of the 19th Annual Conference on Mass Spectroscopy*.

Knutson, E. O. & K. T. Whitby (1975a) Accurate measurement of aerosol electric mobility moments. *Journal of Aerosol Science,* 6.

--- (1975b) Aerosol classification by electric mobility: apparatus, theory, and applications. *Journal of Aerosol Science,* 6**,** 443-451.

Knutson, E. O. & K. T. Whitby (1975c) Aerosol Classification By Electric Mobility: Apparatus, Theory, and Applications. *Journal of Aerosol Science,* 6**,** 443-451.

Ku, B. K. & J. F. de la Mora (2009) Relation between Electrical Mobility, Mass, and Size for Nanodrops 1-6.5 nm in Diameter in Air. *Aerosol Science and Technology,* 43**,** 241-249.

Ku, B. K. & J. Fernandez de la Mora (2009) Relation between Electrical Mobility, Mass, and Size for Nanodrops 1-6.5 nm in Diameter in Air. *Aerosol Science and Technology,* 43**,** 241-249.

Kuang, C., M. Chen, P. H. McMurry & J. Wang (2012) Modification of Laminar Flow Ultrafine Condensation Particle Counters for the Enhanced Detection of 1 nm Condensation Nuclei. *Aerosol Science and Technology,* 46**,** 309-315.

Kuhlbusch, T. A., C. Asbach, H. Fissan, D. Göhler & M. Stintz (2011) Nanoparticle exposure at nanotechnology workplaces: A review. *Particle and Fibre Toxicology,* 8**,** 22.

Kulkarni, P., P. A. Baron & K. Willeke. 2011. *Aerosol measurement: principles, techniques, and applications*. John Wiley & Sons.

Kulkarni, K. S., U. Madanan, R. Mittal & R. J. Goldstein (2017) Experimental validation of heat/mass transfer analogy for two-dimensional laminar and turbulent boundary layers. *International Journal of Heat and Mass Transfer,* 113**,** 84-95.

Kulmala, M., J. Kontkanen, H. Junninen, K. Lehtipalo, H. E. Manninen, T. Nieminen, T. Petaja, M. Sipila, S. Schobesberger, P. Rantala, A. Franchin, T. Jokinen, E. Jarvinen, M. Aijala, J. Kangasluoma, J. Hakala, P. P. Aalto, P. Paasonen, J. Mikkila, J. Vanhanen, J. Aalto, H. Hakola, U. Makkonen, T. Ruuskanen, R. L. Mauldin, J. Duplissy, H. Vehkamaki, J. Back, A. Kortelainen, I. Riipinen, T. Kurten, M. V. Johnston, J. N. Smith, M. Ehn, T. F. Mentel, K. E. J. Lehtinen, A. Laaksonen, V. M. Kerminen & D. R. Worsnop (2013) Direct Observations of Atmospheric Aerosol Nucleation. *Science,* 339**,** 943-946.

Kumar, A., S. Kang, C. Larriba-Andaluz, H. Ouyang, C. J. Hogan & R. M. Sankaran (2014) Ligand-free Ni nanocluster formation at atmospheric pressure via rapid quenching in a microplasma process. *Nanotechnology,* 25**,** 385601.

Kurten, A., T. Jokinen, M. Simon, M. Sipila, N. Sarnela, H. Junninen, A. Adamov, J. Almeida, A. Amorim, F. Bianchi, M. Breitenlechner, J. Dommen, N. M. Donahue, J. Duplissy, S. Ehrhart, R. C. Flagan, A. Franchin, J. Hakala, A. Hansel, M. Heinritzi, M. Hutterli, J. Kangasluoma, J. Kirkby, A. Laaksonen, K. Lehtipalo, M. Leiminger, V. Makhmutov, S. Mathot, A. Onnela, T. Petaja, A. P. Praplan, F.

Riccobono, M. P. Rissanen, L. Rondo, S. Schobesberger, J. H. Seinfeld, G. Steiner, A. Tome, J. Trostl, P. M. Winkler, C. Williamson, D. Wimmer, P. L. Ye, U. Baltensperger, K. S. Carslaw, M. Kulmala, D. R. Worsnop & J. Curtius (2014) Neutral molecular cluster formation of sulfuric acid-dimethylamine observed in real time under atmospheric conditions. *Proceedings of the National Academy of Sciences of the United States of America,* 111**,** 15019-15024.

Kurten, T., V. Loukonen, H. Vehkamaki & M. Kulmala (2008) Amines are likely to enhance neutral and ion-induced sulfuric acid-water nucleation in the atmosphere more effectively than ammonia. *Atmospheric Chemistry and Physics,* 8**,** 4095-4103.

Larriba, C. & J. Fernandez de la Mora (2012) The Gas Phase Structure of Coulombically Stretched Polyethylene Glycol Ions. *The Journal of Physical Chemistry B,* 116**,** 593-598.

Larriba, C., J. Fernandez de la Mora & D. E. Clemmer (2014) Electrospray Ionization Mechanisms for Large Polyethylene Glycol Chains Studied Through Tandem Ion Mobility Spectrometry. *Journal of the American Society for Mass Spectrometry,* 25**,** 1332-1345.

Larriba, C. & C. J. Hogan (2013a) Free Molecular Collision Cross Section Calculation Methods for Nanoparticles and Complex Ions with Energy Accommodation. *Journal of Computational Physics,* 251**,** 344-363.

--- (2013) Ion Mobilities in Diatomic Gases: Measurement versus Prediction with Non-Specular Scattering Models. *Journal of Physical Chemistry A,* 117**,** 3887-3901.

Larriba, C., C. J. Hogan, M. Attoui, R. Borrajo, J. Fernandez-Garcia & J. Fernandez de la Mora (2011) The Mobility-Volume Relationship below 3.0 nm examined by Tandem Mobility-Mass Measurement. *Aerosol Science and Technology,* 45**,** 453-467.

Larriba-Andaluz, C., J. Fernandez-Garcia, M. A. Ewing, C. J. Hogan & D. E. Clemmer (2015) Gas molecule scattering & ion mobility measurements for organic macro-ions in He versus N-2 environments. *Physical Chemistry Chemical Physics,* 17**,** 15019-15029.

Larriba-Andaluz, C. & C. J. Hogan (2014) Collision Cross Section Calculations for Polyatomic Ions Considering Rotating Diatomic/Linear Gas Molecules. *Journal of Chemical Physics,* 141**,** 194107.

Lavi, A., N. Bluvshtein, E. Segre, L. Segev, M. Flores & Y. Rudich (2013) Thermochemical, Cloud Condensation Nucleation Ability, and Optical Properties of Alkyl Aminium Sulfate Aerosols. *Journal of Physical Chemistry C,* 117**,** 22412-22421.

Lee, H. M., C. S. Kim, M. Shimada & K. Okuyama (2005) Bipolar diffusion charging for aerosol nanoparticle measurement using a soft X-ray charger. *Journal of Aerosol Science,* 36**,** 813-829.

Lewis, G. S. & S. V. Hering (2013) Minimizing Concentration Effects in Water-Based, Laminar-Flow Condensation Particle Counters. *Aerosol Science and Technology,* 47**,** 645-654.

Liu, B. Y. & D. Y. Pui (1974) Electrical neutralization of aerosols. *Journal of Aerosol Science,* 5**,** 465-472.

Liu, W., A. L. Davis, W. F. Siems, D. Yin, B. H. Clowers & H. H. Hill (2017) Ambient Pressure Inverse Ion Mobility Spectrometry Coupled to Mass Spectrometry. *Analytical Chemistry***,** 10.1021/acs.analchem.6b03727.

López-Yglesias, X. & R. C. Flagan (2013) Ion–Aerosol Flux Coefficients and the Steady-State Charge Distribution of Aerosols in a Bipolar Ion Environment. *Aerosol Science and Technology,* 47**,** 688-704.

Loukonen, V., T. Kurten, I. K. Ortega, H. Vehkamaki, A. A. H. Padua, K. Sellegri & M. Kulmala (2010) Enhancing effect of dimethylamine in sulfuric acid nucleation in the presence of water - a computational study. *Atmospheric Chemistry and Physics,* 10**,** 4961-4974.

Maestri, L., S. Negri, M. Ferrari, S. Ghittori, F. Fabris, P. Danesino & M. Imbriani (2006) Determination of perfluorooctanoic acid and perfluorooctanesulfonate in human tissues by liquid chromatography/single quadrupole mass spectrometry. *Rapid communications in mass spectrometry,* 20**,** 2728-2734.

Maisser, A., J. M. Thomas, C. Larriba-Andaluz, S. He & C. J. Hogan (2015) The Mass-Mobility Distributions of Ions Produced by a Po-210 Source in Air. *Journal of Aerosol Science,* 90**,** 36-50.

Mäkelä, J. M., V. Jokinen, T. Mattila, A. Ukkonen & J. Keskinen (1996a) Mobility distribution of acetone cluster ions. *Journal of Aerosol Science,* 27**,** 175-190.

Mäkelä, J. M., M. Riihelä, A. Ukkonen, V. Jokinen & J. Keskinen (1996b) Comparison of mobility equivalent diameter with Kelvin-Thomson diameter using ion mobility data. *The Journal of Chemical Physics,* 105**,** 1562-1571.

Makela, J. M., S. Yli-Koivisto, V. Hiltunen, W. Seidl, E. Swietlicki, K. Teinila, M. Sillanpaa, I. K. Koponen, J. Paatero, K. Rosman & K. Hameri (2001) Chemical composition of aerosol during particle formation events in boreal forest. *Tellus Series B-Chemical and Physical Meteorology,* 53**,** 380-393.

Mäkinen, M., M. Nousiainen & M. Sillanpää (2011) Ion spectrometric detection technologies for ultra-traces of explosives: A review. *Mass Spectrometry Reviews,* 30**,** 940-973.

Markowski, G. R. (1987) Improving Twomey's Algorithm for Inversion of Aerosol Measurement Data. *Aerosol Science and Technology,* 7**,** 127-141.

Marrero, T. R. & E. A. Mason (1972) Gaseous Diffusion Coefficients. *Journal of Physical and Chemical Reference Data,* 1**,** 3-118.

Martinez-Lozano, P. & J. Fernandez de la Mora (2006) Resolution improvements of a nano-DMA operating transonically. *Journal of Aerosol Science,* 37**,** 500-512.

Mason, E. A. & E. W. McDaniel. 1988. *Transport Properties of Ions in Gases*. New York: Wiley.

Mason, E. A. & S. C. Saxena (1958) Approximate Formula for the Thermal Conductivity of Gas Mixtures. *The Physics of Fluids,* 1**,** 361-369.

McMurry, P. H. (2000) The History of Condensation Nucleus Counters. *Aerosol Science and Technology,* 33**,** 297-322.

Merenbloom, S. I., R. S. Glaskin, Z. B. Henson & D. E. Clemmer (2009) High-Resolution Ion Cyclotron Mobility Spectrometry. *Analytical Chemistry,* 81**,** 1482-1487.

Mesleh, M. F., J. M. Hunter, A. A. Shvartsburg, G. C. Schatz & M. F. Jarrold (1996) Structural information from ion mobility measurements: Effects of the long-range potential. *Journal of Physical Chemistry,* 100**,** 16082-16086.

Metayer, Y., M. Perrin & G. Madelaine (1982) Analysis of continuous flow condensation nuclei counters.

Meyer, N. A., K. Root, R. Zenobi & G. Vidal-de-Miguel (2016) Gas-Phase Dopant-Induced Conformational Changes Monitored with Transversal Modulation Ion Mobility Spectrometry. *Analytical Chemistry,* 88**,** 2033-2040.

Millikan, R. A. (1923) The General Law of Fall of a Small Spherical Body through a Gas, and its Bearing upon the Nature of Molecular Reflection from Surfaces. *Physical Review,* 22**,** 1-23.

Mordas, G., M. Sipilä & M. Kulmala (2008) Nanometer Particle Detection by the Condensation Particle Counter UF-02proto. *Aerosol Science and Technology,* 42**,** 521-527.

Nadykto, A. B., J. Herb, F. Q. Yu & Y. S. Xu (2014) Enhancement in the production of nucleating clusters due to dimethylamine and large uncertainties in the thermochemistry of amine-enhanced nucleation. *Chemical Physics Letters,* 609**,** 42-49.

Nadykto, A. B., F. Q. Yu, M. V. Jakovleva, J. Herb & Y. S. Xu (2011) Amines in the Earth's Atmosphere: A Density Functional Theory Study of the Thermochemistry of Pre-Nucleation Clusters. *Entropy,* 13**,** 554-569.

Oberreit, D., V. K. Rawat, C. Larriba-Andaluz, H. Ouyang, P. H. McMurry & C. J. Hogan (2015) Analysis of heterogeneous water vapor uptake by metal iodide cluster ions via differential mobility analysis-mass spectrometry. *The Journal of Chemical Physics,* 143**,** 104204.

Oberreit, D. R., P. H. McMurry & C. J. Hogan (2014) Analysis of heterogeneous uptake by nanoparticles via differential mobility analysis-drift tube ion mobility spectrometry. *Physical Chemistry Chemical Physics,* 16**,** 6968-6979.

Oberreit, D. R., P. H. McMurry & C. J. Hogan (2014) Mobility Analysis of 2 nm to 11 nm Aerosol Particles with an Aspirating Drift Tube Ion Mobility Spectrometer. *Aerosol Science & Technology,* 48**,** 108-118.

Ohshimo, K., S. Azuma, T. Komukai, R. Moriyama & F. Misaizu (2015) Structures and CO-Adsorption Reactivities of Nickel Oxide Cluster Cations Studied by Ion Mobility Mass Spectrometry. *The Journal of Physical Chemistry C,* 119**,** 11014-11021.

Okuyama, K., Y. Kousaka & T. Motouchi (1984) Condensational Growth of Ultrafine Aerosol Particles in a New Particle Size Magnifier. *Aerosol Science and Technology,* 3**,** 353-366.

Ortega, I. K., Olenius, T., Kupiainen-Määttä, O., Loukonen, V., Kurtén, T., and Vehkamäki, H. (2014) Electrical charging changes the composition of sulfuric acid–ammonia/dimethylamine clusters. *Atmos. Chem. Phys.,* 14**,** 13.

Ouyang, H., S. Q. He, C. Larriba-Andaluz & C. J. Hogan (2015) IMS-MS and IMS-IMS Investigation of the Structure and Stability of Dimethylamine-Sulfuric Acid Nanoclusters. *Journal of Physical Chemistry A,* 119**,** 2026-2036.

Ouyang, H., C. Larriba-Andaluz, D. R. Oberreit & C. J. Hogan (2013) The Collision Cross Sections of Iodide Salt Cluster Ions in Air via Differential Mobility Analysis-Mass Spectrometry. *Journal of the American Society for Mass Spectrometry,* 24**,** 1833-1847.

Peineke, C., M. B. Attoui & A. Schmidt-Ott (2006) Using a glowing wire generator for production of charged, uniformly sized nanoparticles at high concentrations. *Journal of Aerosol Science,* 37**,** 1851-1661.

Pinterich, T., A. Vrtala, M. Kaltak, J. Kangasluoma, K. Lehtipalo, T. Petäjä, P. M. Winkler, M. Kulmala & P. E. Wagner (2016) The versatile size analyzing nuclei counter (vSANC). *Aerosol Science and Technology,* 50**,** 947-958.

Pratsinis, S. E. (2010) Aerosol-based technologies in nanoscale manufacturing: from functional materials to devices through core chemical engineering. *AIChE journal,* 56**,** 3028-3035.

Premnath, V., D. Oberreit & C. J. Hogan (2011) Collision-Based Ionization: Bridging the Gap between Chemical Ionization and Aerosol Particle Diffusion Charging. *Aerosol Science and Technology,* 45**,** 712-726.

Pui, D., S. Fruin & P. McMurry (1988) Unipolar diffusion charging of ultrafine aerosols. *Aerosol Science and Technology,* 8**,** 173-187.

Qiu, C. & R. Y. Zhang (2012) Physiochemical Properties of Alkylaminium Sulfates: Hygroscopicity, Thermostability, and Density. *Environmental Science & Technology,* 46**,** 4474-4480.

--- (2013) Multiphase chemistry of atmospheric amines. *Physical Chemistry Chemical Physics,* 15**,** 5738-5752.

Rahman, T., L. Renaud, D. Heo, M. Renn & R. Panat (2015) Aerosol based direct-write micro-additive fabrication method for sub-mm 3D metal-dielectric structures. *Journal of Micromechanics and Microengineering,* 25**,** 107002.

Rawat, V. K., G. Vidal-de-Miguel & C. J. Hogan (2015) Modeling vapor uptake induced mobility shifts in peptide ions observed with transversal modulation ion mobility spectrometry-mass spectrometry. *Analyst,* 140**,** 6945-6954.

Reischl, G. P., J. M. Mäkelä, R. Karch & J. Necid (1996) Bipolar charging of ultrafine particles in the size range below 10 nm. *Journal of Aerosol Science,* 27**,** 931-949.

Reischl, G. P., H. G. Scheibel & J. Porstendörfer (1983) The bipolar charging of aerosols: Experimental results in the size range below 20-nm particle diameter. *Journal of Colloid and Interface Science,* 91**,** 272-275.

Revercomb, H. E. & E. A. Mason (1975) Theory of Plasma Chromatography Gaseous Electrophoresis - Review. *Analytical Chemistry,* 47**,** 970-983.

Rus, J., D. Moro, J. A. Sillero, J. Royuela, A. Casado, F. Estevez-Molinero & J. Fernandez de la Mora (2010a) IMS-MS studies based on coupling a differential mobility analyzer (DMA) to commercial API-MS systems. *International Journal of Mass Spectrometry,* 298**,** 30-40.

Schmoll, L. H., T. M. Peters & P. T. O'Shaughnessy (2010) Use of a Condensation Particle Counter and an Optical Particle Counter to Assess the Number Concentration of Engineered Nanoparticles. *Journal of Occupational and Environmental Hygiene,* 7**,** 535-545.

Schneider, C., M. Sablier & B. Desmazières (2008) Characterization by mass spectrometry of an unknown polysiloxane sample used under uncontrolled medical conditions for cosmetic surgery. *Rapid Communications in Mass Spectrometry,* 22**,** 3353-3361.

Seager, S. L., L. R. Geertson & J. C. Giddings (1963) Temperature Dependence of Gas and Vapor Diffusion Coefficients. *Journal of Chemical and Engineering Data,* 8**,** 168-169.

Searcy, J. Q. & J. B. Fenn (1974) Clustering of water on hydrated protons in a supersonic free jet expansion. *The Journal of Chemical Physics,* 61**,** 5282-5288.

Seto, T., K. Okuyama, L. deJuan & J. Fernandez de la Mora (1997) Condensation of supersaturated vapors on monovalent and divalent ions on varying size. *Journal of Chemical Physics,* 107**,** 1576-1585.

Sgro, L. A. & J. Fernandez de la Mora (2004) A simple turbulent mixing CNC for charged particle detection down to 1.2 nm. *Aerosol Science and Technology,* 38**,** 1-11.

Shvartsburg, A. A. & M. F. Jarrold (1996) An exact hard-spheres scattering model for the mobilities of polyatomic ions. *Chemical Physics Letters,* 261**,** 86-91.

Shvartsburg, A. A., S. V. Mashkevich, E. S. Baker & R. D. Smith (2007) Optimization of algorithms for ion mobility calculations. *Journal of Physical Chemistry A,* 111**,** 2002-2010.

Shvartsburg, A. A., S. V. Mashkevich & K. W. M. Siu (2000) Incorporation of thermal rotation of drifting ions into mobility calculations: Drastic effect for heavier buffer gases. *Journal of Physical Chemistry A,* 104**,** 9448-9453.

Sipilä, M., N. Sarnela, T. Jokinen, H. Henschel, H. Junninen, J. Kontkanen, S. Richters, J. Kangasluoma, A. Franchin, O. Peräkylä, M. P. Rissanen, M. Ehn, H. Vehkamäki, T. Kurten, T. Berndt, T. Petäjä, D. Worsnop, D. Ceburnis, V.-M. Kerminen, M. Kulmala & C. O'Dowd (2016) Molecular-scale evidence of aerosol particle formation via sequential addition of HIO3. *Nature,* 537**,** 532.

Smith, J. N., K. C. Barsanti, H. R. Friedli, M. Ehn, M. Kulmala, D. R. Collins, J. H. Scheckman, B. J. Williams & P. H. McMurry (2010) Observations of aminium salts in atmospheric nanoparticles and possible climatic implications. *Proceedings of the National Academy of Sciences,* 107**,** 6634-6639.

Stein, S. E. 2015. NIST Standard Reference Database Number 69, Mass Spectra. In *NIST Chemistry WebBook*. National Institute of Standards and Technology.

Steiner, G., T. Jokinen, H. Junninen, M. Sipila, T. Petaja, D. Worsnop, G. P. Reischl & M. Kulmala (2014) High-Resolution Mobility and Mass Spectrometry of Negative Ions Produced in a Am-241 Aerosol Charger. *Aerosol Science and Technology,* 48**,** 261-270.

Steiner, G. & G. P. Reischl (2012) The effect of carrier gas contaminants on the charging probability of aerosols under bipolar charging conditions. *Journal of Aerosol Science,* 54**,** 21-31.

Steiner, W. E., C. S. Harden, F. Hong, S. J. Klopsch, H. H. Hill Jr & V. M. McHugh (2006) Detection of Aqueous Phase Chemical Warfare Agent Degradation Products by Negative Mode Ion Mobility Time-of-Flight Mass Spectrometry [IM(tof)MS]. *Journal of the American Society for Mass Spectrometry,* 17**,** 241-245.

Stewart, J. J. P. (2007) Optimization of parameters for semiempirical methods V: modification of NDDO approximations and application to 70 elements. *Journal of Molecular modeling,* 13**,** 1173-1213.

Stewart, J. P. (1989) Optimization of parameters for semiempirical methods I. Method. *Journal of Computational Chemistry,* 10**,** 209-220.

St. Louis, R. H. & H. H. Hill (1990) Ion Mobility Spectrometry in Analytical-Chemistry. *Critical Reviews in Analytical Chemistry,* 21**,** 321-355.

Stolzenburg, M. R. & P. H. McMurry (1991) An Ultrafine Aerosol Condensation Nucleus Counter. *Aerosol Science and Technology,* 14**,** 48-65.

Stolzenburg, M. R. & P. H. McMurry (2008) Equations governing single and tandem DMA configurations and a new lognormal approximation to the transfer function. *Aerosol Science and Technology,* 42**,** 421-432.

Tam, M. & H. H. Hill (2004) Secondary electrospray ionization-ion mobility spectrometry for explosive vapor detection. *Analytical Chemistry,* 76**,** 2741-2747.

Tammet, H. (1995) Size and Mobility of Nanometer Particles, Clusters and Ions. *Journal of Aerosol Science,* 26**,** 459-475.

Thomas, J. M., S. He, C. Larriba-Andaluz, J. W. DePalma, M. V. Johnston & C. J. Hogan Jr (2016) Ion mobility spectrometry-mass spectrometry examination of the structures, stabilities, and extents of hydration of dimethylamine–sulfuric acid clusters. *Physical Chemistry Chemical Physics,* 18**,** 22962-22972.

Thomas, J. M., Chen, X., Maisser, A & C. J. Hogan Jr (2018) Differential heat and mass transfer rate influences on the activation efficiency of laminar flow condensation particle counters. *International Journal of Heat and Mass Transfer,* 127A**,** 740-750.

Thomson, S. W. (1871) On the equilibrium of vapour at a curved surface of liquid. *Philosophical Magazine,* 4**,** 448-452.

Tigges, L., A. Jain & H. J. Schmid (2015) On the bipolar charge distribution used for mobility particle sizing: Theoretical considerations. *Journal of Aerosol Science,* 88**,** 119-134.

Timko, M. T., Z. Yu, J. Kroll, J. T. Jayne, D. R. Worsnop, R. C. Miake-Lye, T. B. Onasch, D. Liscinsky, T. W. Kirchstetter, H. Destaillats, A. L. Holder, J. D. Smith & K. R. Wilson (2009) Sampling Artifacts from Conductive Silicone Tubing. *Aerosol Science and Technology,* 43**,** 855-865.

Tsona, N. T., H. Henschel, N. Bork, V. Loukonen & H. Vehkamaki (2015) Structures, Hydration, and Electrical Mobilities of Bisulfate Ion-Sulfuric Acid-

Ammonia/Dimethylamine Clusters: A Computational Study. *Journal of Physical Chemistry A,* 119**,** 9670-9679.
Ude, S. & J. Fernandez de la Mora (2005) Molecular monodisperse mobility and mass standards from electrosprays of tetra-alkyl ammonium halides. *Journal of Aerosol Science,* 36**,** 1224-1237.
Wang, J., V. F. McNeill, D. R. Collins & R. C. Flagan (2002) Fast mixing condensation nucleus counter: Application to rapid scanning differential mobility analyzer measurements. *Aerosol Science and Technology,* 36**,** 678-689.
Wang, S. C. & R. C. Flagan (1990) Scanning Electrical Mobility Spectrometer. *Aerosol Science and Technology,* 13**,** 230-240.
Wiedensohler, A. (1988) An Approximation of the Bipolar Charge-Distribution for Particles in the Sub-Micron Size Range. *Journal of Aerosol Science,* 19**,** 387-389.
Wiedensohler, A. & H. J. Fissan (1988) Aerosol Charging in High-Purity Gases. *Journal of Aerosol Science,* 19**,** 867-870.
--- (1990) Bipolar Ion and Electron-Diffusion Charging of Aerosol-Particles in High-Purity Argon and Nitrogen. *Particle & Particle Systems Characterization,* 7**,** 250-255.
--- (1991) Bipolar Charge-Distributions of Aerosol-Particles in High-Purity Argon and Nitrogen. *Aerosol Science and Technology,* 14**,** 358-364.
Wiedensohler, A., E. Lutkemeier, M. Feldpausch & C. Helsper (1986) Investigation of the Bipolar Charge-Distribution at Various Gas Conditions. *Journal of Aerosol Science,* 17**,** 413-416.
Wilke, C. R. (1950) A Viscosity Equation for Gas Mixtures. *The Journal of Chemical Physics,* 18**,** 517-519.
Wilson, C. T. R. (1897) Condensation of water vapour in the presence of dust-free air and other gases. *Proceedings of the Royal Society of London,* 61**,** 240-242.
--- (1911) On a method of making visible the paths of ionising particles through a gas. *Proceedings of the Royal Society of London. Series A,* 85**,** 285-288.
--- (1912) On an expansion apparatus for making visible the tracks of ionising particles in gases and some results obtained by its use. *Proceedings of the Royal Society of London. Series A,* 87**,** 277-292.
Yli-Ojanperä, J., H. Sakurai, K. Iida, J. M. Mäkelä, K. Ehara & J. Keskinen (2012) Comparison of Three Particle Number Concentration Calibration Standards Through Calibration of a Single CPC in a Wide Particle Size Range. *Aerosol Science and Technology,* 46**,** 1163-1173.
Yu, H., R. McGraw & S. H. Lee (2012) Effects of amines on formation of sub-3 nm particles and their subsequent growth. *Geophysical Research Letters,* 39.
Yu, Y., M. L. Alexander, V. Perraud, E. A. Bruns, S. N. Johnson, M. J. Ezell & B. J. Finlayson-Pitts (2009) Contamination from electrically conductive silicone tubing during aerosol chemical analysis. *Atmospheric Environment,* 43**,** 2836-2839.
Zhang, S.-H., Y. Akutsu, L. M. Russell, R. C. Flagan & J. H. Seinfeld (1995) Radial differential mobility analyzer. *Aerosol Science and Technology,* 23**,** 357-372.

Zhang, L.-Z. (2012) Coupled heat and mass transfer in an application-scale cross-flow hollow fiber membrane module for air humidification. *International Journal of Heat and Mass Transfer,* 55**,** 5861-5869.

Zhao, J., F. L. Eisele, M. Titcombe, C. G. Kuang & P. H. McMurry (2010) Chemical ionization mass spectrometric measurements of atmospheric neutral clusters using the cluster-CIMS. *Journal of Geophysical Research-Atmospheres,* 115.

Zhao, J., J. N. Smith, F. L. Eisele, M. Chen, C. Kuang & P. H. McMurry (2011) Observation of neutral sulfuric acid-amine containing clusters in laboratory and ambient measurements. *Atmospheric Chemistry and Physics,* 11**,** 10823-10836.